Towards First-principles Electrochemistry

Ismaila Dabo

M.S., Mechanical Engineering
École Polytechnique, 2004

Engineering Diploma, Mechanical Engineering
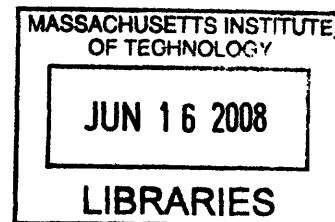École Polytechnique, 2002

Submitted to the Department of Materials Science and Engineering
in partial fulfillment of the requirements for the degree of

DOCTOR OF PHILOSOPHY IN MATERIALS SCIENCE AND ENGINEERING

at the

MASSACHUSETTS INSTITUTE OF TECHNOLOGY

February 2008

Author.........................
Department of Materials Science and Engineering
September 20, 2007

Certified by ....
Nicola Marzari
Associate Professor of Materials Science and Engineering
Thesis Supervisor

Accepted by.....................
Samuel Allen
POSCO Professor of Physical Metallurgy
Chair, Department Committee on Graduate Students

Towards First-principles Electrochemistry

Ismaila Dabo

Submitted to the Department of Materials Science and Engineering
on September 20, 2007, in partial fulfillment of the
requirements for the degree of
Doctor of Philosophy in Materials Science and Engineering

Abstract

This doctoral dissertation presents a comprehensive computational approach to describe quantum mechanical systems embedded in complex ionic media, primarily focusing on the first-principles representation of catalytic electrodes under electrochemical conditions. The accurate electrostatic description of electrified metal-solution interfaces represents a persistent challenge for *ab-initio* simulations and an essential requisite for predicting the electrical response of electrochemical convertors—*i.e.*, the correspondence between the macroscopic voltage and the microscopic interfacial charge distribution.

The approach consists of controlling the electrode voltage via its conjugate extensive variable, namely, the charge of the system. As a preliminary to the study of electrified interfaces in ionic media, we analyze charged slabs in vacuum subject to periodic boundary conditions. We show that the corrective potential (defined as the difference between the exact open-boundary potential and the periodic potential obtained from a Fourier transform) varies smoothly over space, allowing for its determination on a coarse mesh using optimized electrostatic solvers. Because this scheme takes into account exact open boundary conditions, its performance is considerably superior to that of conventional corrective methods. Extending this computational scheme, we present an efficient approach to model electrochemical systems under realistic conditions, based on a first-principles description of the interface region and on a continuum representation of the ionic solvent. We demonstrate that the ionic-solution contribution to the electrostatic potential—the ionic solvent reaction field—can be computed independently at low cost simultaneously using fast Fourier transforms and multigrid techniques, and highlight the importance of adopting adequate electrochemical boundary conditions to correctly predict the electrical response of electrode-electrolyte interfaces.

In order to probe and validate the electrochemical model, we study the vibrational Stark effect—*i.e.*, the influence of the applied voltage on the vibrational properties—for carbon monoxide adsorbed on transition metal surfaces, a phenomenon whose description requires an accurate representation of the interfacial electric field. We start out the analysis by examining the vibrational properties of CO adsorbed on clean and ruthenium-covered platinum substrates. The calculated C–O stretching frequencies are found to be in excellent agreement with experimental measurements despite the frequent qualitative failures of local and semilocal

exchange-correlation functionals in predicting adsorption energies for CO on transition metals. We then introduce an orbital-resolved force analysis to clarify the electronic origins of the C–O red shifts, and present a sensitivity analysis to assess the influence the HOMO and LUMO hybridizations on the calculated frequencies, thereby establishing the remarkable accuracy of conventional density-functional theory methods in determining the vibrational properties of adsorbed CO. Based on these results, we apply the electrochemical model to provide the first comprehensive *ab-initio* description of the vibrational Stark effect for CO on transition metal surfaces, finding excellent agreement with spectroscopic measurements.

As related projects, we have implemented a molecular-dynamics algorithm for metallic systems and developed a self-interaction correction method to rectify the tendency of density-functional theory calculations to overestimate binding energies.

The present computational electrochemistry toolkit open promising perspectives for the application of first-principles methods to assist the microstructural engineering of electro-chemical convertors.

Thesis Supervisor: Nicola Marzari
Title: Associate Professor of Materials Science and Engineering

À ma mère Fatoumata, à mon père Oumar.

Acknowledgments

My first and deepest thanks go to my family, whose constant support carried me through the most difficult times. Without the inspiring encouragement from my beloved ones, I could never have hoped to successfully complete this doctoral project.

I am also extremely grateful to my advisor, Prof. Nicola Marzari. To him I owe, everything I know. I wish to thank Prof. Gerbrand Ceder, Prof. Sanjeev Mukerjee, and Prof. Yang Shao-Horn, who served in my thesis committee and without whom this project would not have materialize.

I am indebted to Prof. Andrzej Wieckowski with whom I had the privilege to work on the interpretation of spectroscopic experiments. I would also like to thank Matteo Cococcioni, who helped me in the early stage of my doctoral research, and to acknowledge Damian Scherlis, Paolo Umari, and Cody Friesen for their valuable guidance. Moreover, I had the great pleasure to collaborate with Boris Kozinsky and Nicholas Singh-Miller on some of the most important aspects of this thesis. I also wish to express my deep gratitude to Brandon Wood for his exceptional patience whenever I needed scientific or stylistic advice; to Young-Su Lee for her continual attention to the well-being of the group; and to Nicolas Poilvert for his positive and enthusiastic energy. I am also grateful to all the group members, present and past—Francesca Baletto, Nicola Bonini, Nicéphore Bonnet, Oswaldo Dieguez, Prof. Marco Fornari, Jivtesh Garg, Sejoong Kim, Heather Kulik, Elise Li, Arash Mostofi, Nicolas Mounet, Manu Sharma, Patrick Sit, Michael Tambe, Timo Thonhauser—for managing to put up with me during all these years. My deep thanks also go to Kathryn Simons for her help and joyful friendship. I thank the École Nationale des Ponts et Chaussées (France) and the Martin Family Society of Fellows for Sustainability for their assistance and support.

Finally, I owe the deepest gratitude to Fabien Sorin and to my dear friends, whose presence has been a constant source of happiness and joy throughout my years at MIT.

Contents

List of Figures

14

List of Tables

Introduction

1.1 Origin and Development of Electrochemistry

IN 1771, THE ANATOMIST AND PHYSICIAN Luigi Galvani conducted a series of experiments on animal tissue, thereby establishing the electrical origin of muscular contraction. Subsequently, in a seminal treatise entitled *De Viribus Electricitatis in Motu Musculari Commentarius* (Memorandum on the Role of Electric Forces in Muscular Motion) [1], Galvani postulated the existence of an innate vital force termed animal electricity or galvanism. Firmly opposed to Galvani's theory, physics professor Alessandro Volta claimed that the newly evidenced form of electricity does not come from muscular tissue but results from the immersion of two metals of *different temper* in a moist environment. Volta's reinterpretation was promptly contested by Galvani.

Luigi Galvani (1737-1798)

Alessandro Volta (1745-1827)

The vivid scientific debate that confronted Galvani to Volta at the end of the eighteenth century is often considered to mark the birth of electrochemistry, an interdisciplinary science that has stood, from its very inception, at the frontier between biology, physics, and chemistry.

In the early nineteenth century, electrochemistry rapidly evolved into a well-established discipline owing, above all, to the experimental achievements of Michael Faraday.

From studying electrically driven chemical decomposition, Faraday developed a phenomenological theory of electrolysis and enunciated a set of laws relating the amount of electricity passing through an electrical cell to the quantity of substance depositing on the *anode* and on the *cathode*—two designations whose introduction is commonly attributed to Faraday.

Michael Faraday (1791-1867)

Svante Arrhenius (1859-1927)

Walther Nernst (1864-1941)

In 1884, Svante Arrhenius published his doctoral dissertation entitled *Recherches sur la Conductibilité Galvanique des Électrolytes* (Research on the Galvanic Conductivity of Electrolytes) [2] and proposed a microscopic theory for ionic dissociation in aqueous solutions.[1] In 1889, based on Arrhenius' results, Walther Nernst derived and evidenced the existence of a hitherto unknown electrostatic driving force for ionic transport in electrolytes, which he termed *electrolytic pressure of dissolution*. The fundamental contributions from Arrhenius and Nernst laid down the platform for the modern theory of electrolytic solutions introduced by Peter Debye and his research assistant Erich Hueckel in 1923. The Debye-Hueckel theory provides a reliable representation of ionic interactions in solution and is widely used to this day.

Despite the success of the Debye-Hueckel theory for describing ionic interactions in electrolytes, the current understanding of solvated electrode surfaces—the Gouy-Chapman-Stern theory—remains questioned. Difficulties in describing solvated electrodes arise out primarily from the complex structure of the interphase region separating the electrode and the electrolyte, commonly referred to as

Peter Debye (1884-1966)

the electrical double layer—a terminology popularized by Helmholtz. The experimental validation and theoretical extension of the Gouy-Chapman-Stern double-layer model constitute two essential challenges in modern electrochemistry.

---

[1]Interestingly enough, Arrhenius barely passed his doctoral examination, receiving the lowest admissible grade.
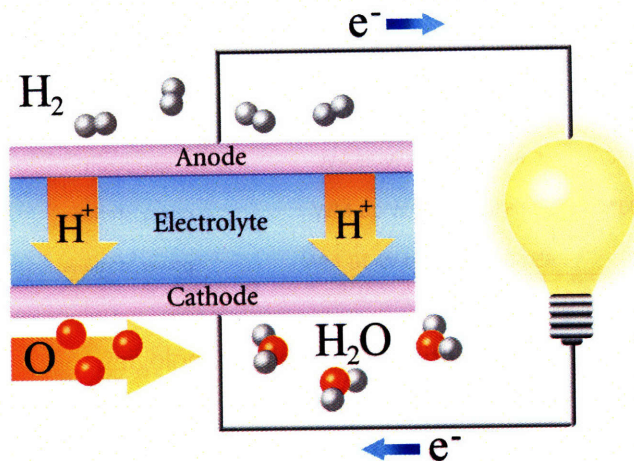
Figure 1-1: Principle of operation of a proton electrolyte membrane fuel cell (PEMFC). At the anode, hydrogen is oxidized into H^+, liberating electrons. At the cathode, oxygen is reduced to form water. This electrochemical process generates electricity and heat. (Courtesy B. C. Wood [5].)

In recent decades, a number of experimental methods for the characterization of electro-chemical surfaces have been developed. These techniques can be categorized into two classes. The first class, which includes cyclic voltammetry and impedance spectroscopy, proceeds by relating the total current flowing through the cell to the rate of an electrochemical process taking place at the electrode-electrolyte interface. The second class consists of probing solvated interfaces by surface-sensitive spectroscopy. Among the existing *in-situ* spectroscopic techniques—*e.g.*, radiotracing, ellipsometry, surface plasmons, surface-enhanced Raman spectroscopy, Fourier transform infrared spectroscopy [3]—optical sum-frequency generation (SFG) has recently gained considerable interest [4].

Simultaneously to the evolution of experimental techniques, conventional continuum theories for the description of electrified solid-liquid interfaces are now supplemented by a range of first-principles methods of increasing predictive ability. Particularly, density-functional theory (DFT) has emerged as one of the most successful approaches for studying molecular adsorption on metal surfaces.

1.2 Challenges in Fuel-cell Microstructural Engineering

Fuel cells are electrochemical convertors of potential high environmental benefit that provide electricity and heat by catalytic conversion of a fuel, such as hydrogen or methanol. The general principle of a hydrogen proton electrolyte membrane fuel cell (PEMFC) is illustrated in Figure 1-1.

Besides PEMFCs, there exist several types of fuel cells, which primarily differ by their

Type	Ion	Electrolyte	Operating temperature	Nominal efficiency	Nominal power	Applications
PEMFC	H^+	polymer	30-100°C	40-60%	1 W-250 kW	transportation, portable devices
DMFC	H^+	polymer	20-130°C	40%	1 W-10 kW	portable devices
PAFC	H^+	phosphoric acid	200°C	35-40%	10 kW-1 MW	power stations
AFC	OH^-	potassium hydroxide	50-200°C	45-60%	1 kW-25 kW	spacecraft
SOFC	O^{2-}	ceramic	500-1000°C	50-65%	1 kW-10 MW	power stations
MCFC	CO_3^{2-}	molten carbonate	650°C	45-60%	100 kW-10 MW	power stations

Table 1.1: Technical characteristics of conventional fuel-cell technologies.

nominal power, their operating temperature, and the electrochemical reaction involved. A comparison of fuel-cell technologies is presented in Table 1.1. It should be noted that low-temperature PEMFCs and direct methanol fuel cells (DMFCs) are principally suited for transportation and portable applications, while intermediate- and high-temperature alkaline fuel cells (AFCs), solid oxide fuel cells (SOFCs), molten carbonate fuel cells (MCFCs), and phosphoric acid fuel cells (PAFCs) are typically employed as stationary co-generators.

Paradoxically, the introduction of fuel-cell technology is by no means recent: the principle of fuel cells was identified as early as 1839 by William Grove who accidentally observed catalytic electricity generation while conducting electrolysis experiments with platinum electrodes. In 1843, Grove designed the first fuel cell (the *gas voltaic battery*). Despite early development, fuel cells were prematurely abandoned in favor of internal combustion engines due to their relative lack of performance, at a time when environmental sustainability, among other crucial concerns, was not a priority. It was only in the 1960s—after a dormant phase of more than one century—that NASA and General Electrics revived fuel-cell technology for the supply of electricity (and drinking water) in manned space vehicles.

William Grove (1811-1896)

In spite of significant progress in the engineering of fuel-cell components—such as the introduction of the Nafion electrolyte membrane (DuPont, 1967) or the development of finely dispersed carbon-supported catalysts—fuel-cell technology is only slowly reaching the stage of commercial viability. Notably, the deployment of fuel cells has been hindered by the surging cost of precious metal catalysts.

In addition to material cost constraints, the nominal power of fuel-cell systems is subject to intrinsic limitations. The energy and power densities per unit mass of conventional energy

Figure 1-2: Ragone diagram—power density versus energy density per unit mass—of energy storage and delivery technologies (Tester *et al.* [6]).
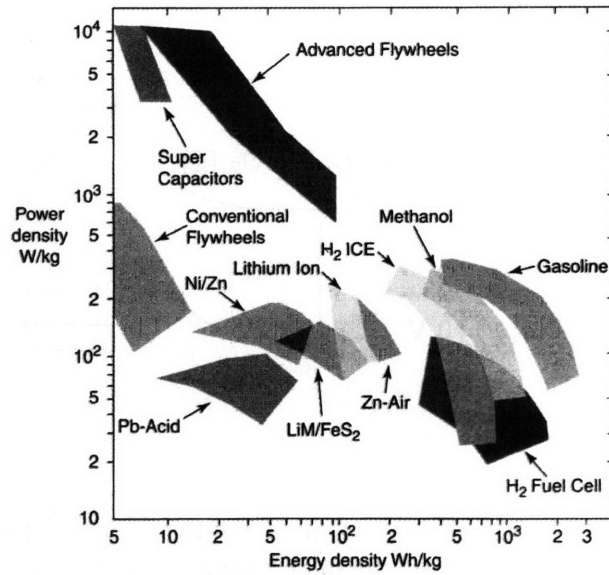
technologies are reported in logarithmic scale in Figure 1-2. One prominent feature of the diagram is the high energy storage and delivery performance of gasoline internal combustion engines—this fact explains their traditional predominance in the energy sector. In comparison, fuel cells exhibit intermediate power densities despite high energy densities. Two major power-density limitations can be identified [7]: *ohmic losses* (irreversible losses due to the resistance to proton transport in the electrolyte and to the electrical resistance of the cell), and *activation losses* (irreversible losses due to the necessity of bringing the fuel cell under slight off-equilibrium conditions in order to drive the electrochemical reaction). Activation losses were first evidenced by Tafel in 1905 and can be characterized by the Butler-Volmer equation:

$$i = i_+ - i_- = i_0 \exp\left(\alpha \frac{nF\eta_{act}}{RT}\right) - i_0 \exp\left(-(1-\alpha)\frac{nF\eta_{act}}{RT}\right) \qquad (1.1)$$

where η_{act} is the activation voltage drop (activation overvoltage), n is the number of electrons involved in the electrochemical reaction, α is the charge-transfer coefficient that quantifies the relative proportion of overvoltage effectively engaged in driving the electrochemical process at each electrode, i is the total current density, i_+ is the forward anodic current, i_- is the backward cathodic current, and i_0 is the exchange-current density prefactor that characterizes the intrinsic activity of the catalyst. Figure 1-3 illustrates the influence of the activation overvoltage on the operation of a hydrogen fuel cell. Among the possible options for reducing activation losses (*e.g.*, changing the operating temperature, varying the concentration and the purity of the reactants, or increasing the specific surface area by microstructural optimization),
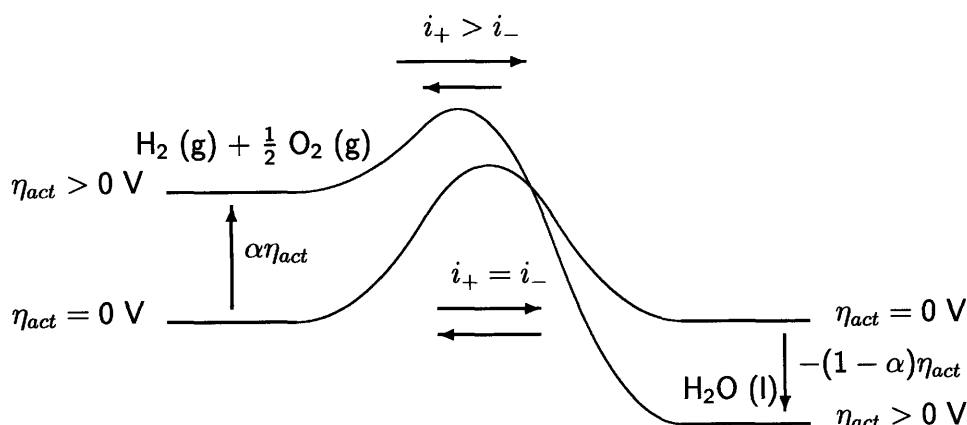
Figure 1-3: Influence of the activation overvoltage η_{act} on the kinetics of the hydrogen oxidation reaction. At the open-circuit voltage ($\eta_{act} = 0$), the forward current i_+ and backward current i_- cancel out: the cell does not supply any electrical current. Applying a positive overvoltage breaks the electrochemical equilibrium and drives the catalytic conversion.

a privileged route consists of raising the exchange-current density by improving the catalytic properties of the electrode materials.

Besides catalytic performance, the chemical stability of fuel-cell components under severe pressure, temperature, and acidity conditions constitutes a primary concern. Several degradation processes may limit the durability of a fuel cell: infinitesimal amounts of strongly adsorbed impurities may dramatically poison the electrodes; acidity conditions can cause the electrode to dissolve in the electrolyte; radical attack can lead to the decomposition of the electrolyte-membrane; among other detrimental factors. The characterization of complex degradation phenomena and the design of chemically resistant materials represent fundamental challenges in fuel-cell research.

1.3   Towards First-principles Electrochemistry

Confronted with daunting—and oftentimes contradictory—material design constraints, fuel-cell engineering is increasingly relying on bottom-up approaches based on a strong interplay between theory and experiment. In that respect, first-principles simulations have become instrumental. Density-functional theory calculations are now routinely employed for the prediction of electrode surface structures, the elucidation of catalytic trends, and the interpretation

of spectroscopic experiments.

Notwithstanding the increasing relevance of density-functional theory simulations, several methodological limitations restrict their more widespread use in fuel-cell research and electrochemistry. First and foremost, modeling solvated interfaces subject to a constant electrical potential represents a persistent challenge. Growing out of the compelling necessity of achieving a realistic first-principles description of electrochemical surfaces, this thesis presents and applies novel computational approaches extending the applicability of density-functional theory calculations in electrochemistry.

This dissertation focuses chiefly on *CO poisoning*, a phenomenon that imposes important limitations to the performance of low-temperature PEMFC and DMFC electrodes. The central purpose of this work is to investigate the vibrational properties of carbon monoxide adsorbed on platinum and platinum-ruthenium surfaces under varying electrical-potential conditions in order to help the spectroscopic recognition of CO adsorption sites on transition-metal electrodes and the elucidation of important chemical mechanisms related to CO poisoning.

The outline of this doctoral dissertation follows:

- The second chapter starts out with presenting density-functional theory and density-functional perturbation theory. The remainder of the chapter describes the ensemble density-functional theory minimization scheme and introduces a parameter-free method for eliminating electronic self-interactions in density-functional theory calculations.

- The third chapter addresses periodic-image errors arising out from the use of periodic boundary conditions to describe systems that do not exhibit full three-dimensional periodicity, and presents an efficient method to calculate the properties of charged surfaces in vacuum.

- The fourth chapter introduces a first-principles model for predicting the electrical response of electrified metal-liquid interfaces subject to an applied voltage. The approach is based on a density-functional theory description of the interface region and a continuum representation of the semi-infinite ionic solvent.

- In the fifth chapter, we study the vibrational properties of CO adsorbed on clean and ruthenium-covered platinum surfaces, finding excellent agreement with SFG measurements notwithstanding well-known qualitative discrepancies in the predicted adsorption energies. In order to establish the accuracy of density-functional calculations in determining adsorbate vibrational properties, we introduce an orbital-resolved force analysis,

and present a sensitivity analysis for the calculated intramolecular frequencies based on hybridization penalization methods.

- The sixth chapter is devoted to the prediction of the electrode-potential dependence of the vibrational properties of CO on platinum and platinum-ruthenium substrates—a phenomenon known as the *vibrational Stark effect*—with the ultimate aim of completing the electrochemical interpretation of spectroscopic measurements.

Computational Methods

2.1 Density-functional Theory

SOLVING THE MANY-BODY SCHROEDINGER EQUATION generally proves to be a daunting task. Density-functional theory offers a practical formulation for studying the ground state of electronic systems. This section provides a succinct presentation of the DFT approach.

In 1964, based on the fact that the properties of electronic systems are uniquely determined by their ground-state charge density (*first Hohenberg-Kohn theorem*),[1] Hohenberg and Kohn introduced a variational alternative to the many-electron Schroedinger equation. The fundamental variable of this variational scheme is the electronic density (*second Hohenberg-Kohn theorem*) [8]. The finite-temperature extension of the Hohenberg-Kohn theorems

Walter Kohn (b. 1923)

was proposed by Mermin the following year [9]. A practical self-consistent scheme was subsequently devised by Kohn and Sham [10]. The Kohn-Sham approach, which introduces an independent-electron mapping of the many-body problem, consists of considering the follow-

---

[1]The electronic ground state is assumed to not be degenerate.

ing energy functional:

$$
\begin{aligned}
F[\{\psi_i\}, \{f_i\}] &= E[\{\psi_i\}, \{f_i\}] - \sigma S(\{f_i\}) \\
&= -\frac{1}{2}\sum_i f_i \langle \psi_i | \nabla^2 | \psi_i \rangle + \int \frac{n(\mathbf{r})n(\mathbf{r}')}{|\mathbf{r}-\mathbf{r}'|} d\mathbf{r}d\mathbf{r}' + \int v(\mathbf{r})n(\mathbf{r}) + E_{XC}[n] \\
&\quad + \sigma \sum_i f_i \ln f_i + (1-f_i)\ln(1-f_i)
\end{aligned}
\tag{2.1}
$$

where v is the ionic potential, $n = \sum_i f_i |\psi_i|^2$ denotes the electronic charge density, E_{XC} stands for the exchange-correlation energy, and σ is the electronic temperature of the Fermi-Dirac broadening. (It should be mentioned that alternative formulations of the electronic thermal distribution have been proposed for the essential purpose of numerical convergence [11, 12].)

Minimizing the energy functional F for normalized wavefunctions, we obtain the self-consistent Kohn-Sham equations:

$$
\left\{
\begin{aligned}
&\hat{h}^{eff}\psi_i(\mathbf{r}) = \epsilon_i\psi_i(\mathbf{r}) \\
&\hat{h}^{eff} = -\frac{1}{2}\nabla^2 + \int \frac{n(\mathbf{r}')}{|\mathbf{r}-\mathbf{r}'|}d\mathbf{r}' + v(\mathbf{r}) + v_{XC}(\mathbf{r}) \\
&f_i = 1 \left/ \left\{ 1 + \exp\left(\frac{\epsilon_i - \epsilon_F}{\sigma}\right)\right\}\right. \\
&n(\mathbf{r}) = \sum_i f_i |\psi_i(\mathbf{r})|^2
\end{aligned}
\right.
\tag{2.2}
$$

where $\hat{h}^{eff}$ is the effective single-electron Hamiltonian, ϵ_i is the single-electron energy (due to the wavefunction normalization constraint), ϵ_F is the Fermi energy (arising from fixing the number of electrons N), and $v_{XC}[n] = \delta E_{XC}/\delta n$ denotes the functional derivative of the exchange-correlation energy (explicitly, $\delta E_{XC} = \int v_{XC}[n](\mathbf{r})\delta n(\mathbf{r})d\mathbf{r}$). In Eq. 2.2, the Fermi energy is chosen so that the sum of the electronic occupations equals the total number of electrons.

It is important to realize that the precision of density-functional theory calculations is determined by the quality of the exchange-correlation approximation. The minimal local density approximation (LDA) [10] consists of employing the exchange functional derived by Dirac in the context of the Thomas-Fermi-Dirac theory [13]:

$$
E_X^{LDA}[n] = -\frac{3}{4}\left(\frac{3}{\pi}\right)^{\frac{1}{3}} \int n^{\frac{4}{3}}(\mathbf{r})d\mathbf{r}
\tag{2.3}
$$

Several refinements to the local density approximation have been proposed (local-spin density approximation [13], Ceperley-Alder correlation [14], generalized-gradient approximations [15, 16], and hybrid exchange-correlation functionals [17,18]).

To close this introduction, it is worth noting that density-functional theory borrows from both the Thomas-Fermi-Dirac and Hartree-Fock methods. Indeed, as in the Thomas-Fermi-Dirac model, the charge density is the fundamental variational variable, and similarly to the Hartree-Fock method, density-functional theory provides a self-consistent scheme based on single-electron orbitals.

2.2 Density-functional Perturbation Theory

2.2.1 Vibrational Properties from First Principles

Several methods can be employed to determine the vibrational properties of a system from density-functional theory:

- Frozen-phonon method

  The second derivatives of the density-functional free energy are evaluated by displacing the atoms from their equilibrium positions. The eigenvalue problem $\det \left\{ (m_I m_J)^{-1/2} \partial^2 F / \partial \mathbf{R}_I \partial \mathbf{R}_J - \omega^2 \delta_{IJ} \right\} = 0$ (where m_I is the atomic mass of Ith ionic species) is then solved to obtain the vibrational frequencies.

- Molecular-dynamics spectral analysis

  The vibrational spectrum is determined by performing a Fourier transform on the velocity autocorrelation function $\langle \mathbf{v}(t)\mathbf{v}(t+\tau)\rangle_t$.

- Density-functional perturbation theory (DFPT)

  The second derivatives of the energy are calculated directly using a linear-response approach. This method is particularly advantageous for calculating the phonon frequencies corresponding to a lattice perturbation corresponding to an arbitrary wavevector [19].

A brief description of density-functional perturbation theory is presented below.

2.2.2 Density-functional Perturbation Theory Formalism

Density-functional perturbation theory consists of calculating the free-energy Hessian as:

$$\frac{\partial^2 F}{\partial \mathbf{R}_I \partial \mathbf{R}_J} = \int \frac{\partial^2 v(\mathbf{r})}{\partial \mathbf{R}_I \partial \mathbf{R}_J} n(\mathbf{r}) + \frac{\partial v(\mathbf{r})}{\partial \mathbf{R}_I} \frac{\partial n(\mathbf{r})}{\partial \mathbf{R}_J} dr, \qquad (2.4)$$

where use has been made of the free-energy minimality condition (Hellmann-Feynman theorem). Following Ref. [20], the density variation can be written as:

$$\frac{\partial n(\mathbf{r})}{\partial \mathbf{R}_I} = \sum_{i\sigma} \psi^*_{i\sigma}(\mathbf{r}) \Delta_I \psi_{i\sigma}(\mathbf{r}), \qquad (2.5)$$

where

$$\Delta_I \psi_{i\sigma}(\mathbf{r}) = \sum_{j} \theta_{j\sigma,i\sigma} \frac{f_{i\sigma} - f_{j\sigma}}{\epsilon_{i\sigma} - \epsilon_{j\sigma}} \langle \psi_{j\sigma} | \frac{\partial v(\mathbf{r})}{\partial \mathbf{R}_I} | \psi_{i\sigma} \rangle \psi_{j\sigma}(\mathbf{r}). \qquad (2.6)$$

$\theta_{i\sigma,j\sigma}$ equals 1 if $\epsilon_{i\sigma} < \epsilon_{j\sigma}$ and is null otherwise.

Calculating $\Delta_I \psi_{i\sigma}$ by summation over all the occupied and unoccupied levels is cumbersome, however. An efficient alternative consists of evaluating $\Delta_I \psi_{i\sigma}$ using a linear-response approach. The scheme proceeds by determining $\Delta_I \psi_{i\sigma}$ as the solution of a problem of the form:

$$\{\hat{h}^{eff} + \hat{Q} - \epsilon_{i\sigma}\} | \Delta_I \psi_{i\sigma} \rangle = | \kappa_{i\sigma} \rangle, \qquad (2.7)$$

where $\hat{Q} = \sum_{j\sigma} \alpha_{j\sigma} | \psi_{j\sigma} \rangle \langle \psi_{j\sigma} |$ is introduced to insure that the Green's operator $\mathcal{G}_{i\sigma} = (\hat{h}^{eff} + \hat{Q} - \epsilon_{i\sigma})^{-1}$ is not singular.

A plane-wave implementation for lattice perturbations of an arbitrary wavevector was presented by Baroni et al. [19]. An extension of this method to the Vanderbilt ultrasoft formalism [21] was proposed by Dal Corso [22].

2.3 Ensemble Density-functional Theory

2.3.1 Level-crossing Instabilities in Metals

Due to their nonvanishing density of states at the Fermi level, metallic and semiconducting systems must be treated carefully. Indeed, when applying iterative algorithms to determine the Kohn-Sham ground state of such systems, crossings between single-electron energies in the vicinity of ϵ_F systematically occur. These level crossings cause sharp occupation variations,

which results in significant electron-density fluctuations that strongly destabilize the self-consistent procedure. Ensemble density-functional theory (eDFT) provides an effective way to handle these instabilities.

2.3.2 Ensemble Density-functional Theory Formalism

Ensemble density-functional theory was introduced by Marzari, Vanderbilt, and Payne [23]. It essentially consists of adopting a matrix representation for the Kohn-Sham occupations:

$$f_i \rightarrow f_{ij} \tag{2.8}$$

Correspondingly, the Kohn-Sham free energy is rewritten as:

$$
\begin{aligned}
F[\{\psi_i\}, \{f_{ij}\}] &= -\frac{1}{2}\sum_{ij} f_{ij}\langle\psi_j|\nabla^2|\psi_i\rangle + \int \frac{n(\mathbf{r})n(\mathbf{r}')}{|\mathbf{r}-\mathbf{r}'|}d\mathbf{r}d\mathbf{r}' \\
&\quad + \int v(\mathbf{r})n(\mathbf{r})d\mathbf{r} + E_{XC}[n] - \sigma\text{Tr}\{S(\mathbf{f})\},
\end{aligned}
\tag{2.9}
$$

where $\mathbf{f} = [f_{ij}]$ denotes the occupation matrix and $S(f) = -f\ln f - (1-f)\ln(1-f)$ stands for the occupation-dependent Fermi-Dirac entropy function. A minimization over the occupation variables is then performed to obtain a *projected functional* $G[\{\psi_i\}]$:

$$G[\{\psi_i\}] = \min_{\{f_{ij}\}} F[\{\psi_i\}, \{f_{ij}\}] \tag{2.10}$$

As discussed in Ref. [23], employing the projected functional G instead of the free energy F leads to a more rapid evolution of the Kohn-Sham orbitals towards the electronic ground state in static calculations and stabilizes molecular dynamics evolutions.

2.3.3 Ensemble Density-functional Theory Algorithm

The ensemble density-functional algorithm aims at minimizing the Kohn-Sham free energy F with respect to the occupation matrix $\mathbf{f}$ under the constraint $\text{Tr}(\mathbf{f}) = N$. This algorithm proceeds as follows:

Ensemble Density-functional Theory (eDFT) Algorithm

1. Start with the initial occupation matrix $\mathbf{f}^{(n=0)} = [f_{ij}^{(n=0)}]$.

2. Find the non-self-consistent solution $\tilde{\mathbf{f}}^{(n)}$ of $\partial\{F - \epsilon_F \mathrm{Tr}(\mathbf{f})\}/\partial \mathbf{f}|_{\hat{h}_{eff}} = 0$.

   (The Fermi energy ϵ_F is chosen in such a way that $\mathrm{Tr}(\mathbf{f}) = N$.)

3. Define the search direction: $\Delta\mathbf{f}^{(n)} = \tilde{\mathbf{f}}^{(n)} - \mathbf{f}^{(n)}$.

4. Interpolate and minimize $F(\lambda) = F(\mathbf{f}^{(n)} + \lambda\Delta\mathbf{f}^{(n)})$ to obtain $\lambda_{min}^{(n)}$.

   (A proper choice for interpolating the energy $E - \sigma S$ is to use a function of the form $P - \sigma\sum_i S(Q_i)$, where P and Q_i are third order polynomials.)

5. Update $\mathbf{f}$: $\mathbf{f}^{(n+1)} = \mathbf{f}^{(n)} + \lambda_{min}^{(n)}\Delta\mathbf{f}^{(n)}$.

6. Iterate from Step 2 until convergence.

It is worth noting that the free energy systematically decreases along the search direction in the vicinity of $\mathbf{f}^{(n)}$. This fact can be established by expressing the free energy derivative as:

$$\frac{dF}{d\lambda}(0) = \mathrm{Tr}[\mathbf{h}^{(n)} - \sigma S'(\mathbf{f}^{(n)})]\Delta\mathbf{f}^{(n)} \tag{2.11}$$

where the coefficients of the matrix $\mathbf{h}^{(n)}$ are defined as $h_{ij}^{(n)} = \langle\psi_i|\hat{h}^{eff}(\mathbf{f}^{(n)})|\psi_j\rangle$. By definition, $\tilde{\mathbf{f}}^{(n)}$ satisfies the non-self-consistent minimality condition:

$$\mathbf{h}^{(n)} - \sigma S'(\tilde{\mathbf{f}}^{(n)}) - \epsilon_F \mathbf{I} = 0 \tag{2.12}$$

Consequently, substituting the preceding equation in the expression of the derivative $\dfrac{dF}{d\lambda}(0)$, we obtain:

$$\frac{dF}{d\lambda}(0) = \sigma\mathrm{Tr}\left[(S'(\tilde{\mathbf{f}}^{(n)}) - S'(\mathbf{f}^{(n)}))(\tilde{\mathbf{f}}^{(n)} - \mathbf{f}^{(n)})\right] \tag{2.13}$$

where use has been of the fact that $\mathrm{Tr}(\mathbf{f}^{(n)}) = \mathrm{Tr}(\tilde{\mathbf{f}}^{(n)})$. Hence, S being a decreasing function, the derivative of the free energy at the origin of the search direction is always negative.

2.4 Self-interaction Corrections

2.4.1 Self-interaction Errors in Mean-field Theories

The fundamental idea underlying the Kohn-Sham procedure is to recast many-body electronic interactions into an effective mean-field potential. Since the effective potential is constructed as a functional of the total charge density, each electron is implicitly immersed in a field that includes a contribution from its own charge density, which gives rise to unphysical electronic self-interactions.

Although self-interaction errors are present in most mean-field descriptions, they are of particular significance for DFT calculations. Indeed, self-interaction is responsible for the well-known tendency of conventional density-functional methods to delocalize electronic states. This tendency results in frequent underestimations of the energy gap for insulators and semi-conductors [24]. For the same fundamental reason, Koopmans' theorem, which identifies the ionization potential of a molecule as the energy of its highest occupied orbital, cannot be applied to density-functional theory. In addition, self-interaction is at the origin of orbital overhybridization that ultimately translates into overestimated binding energies.

A number of schemes have been proposed to eliminate electronic self-interaction errors in electronic-structure calculations. In the context of the Thomas-Fermi-Dirac theory, Fermi and Amaldi introduced a corrective approach that relies on suppressing the electrostatic self-interaction energy corresponding to the total electronic density rescaled by the number of electrons. Extending the Fermi-Amaldi prescription to density-functional theory, the Perdew-Zunger self-interaction correction (PZ-SIC) proceeds by subtracting individual electronic contributions to the total energy functional. Several refinements of the Perdew-Zunger method have been proposed. It is also important to note that a number of recently popularized first-principles approaches—such as hybrid density functional theories (HDFTs) [18]—inherently reduce self-interaction errors. In addition to these approaches, the LDA + U method introduced by Anisimov et al. [25–28] consists of eliminating electronic overhybridization by adding orbital Hubbard U contributions to the total energy, thus imposing a penalty on partially occupied electronic states. Subsequently, Cococcioni and de Gironcoli [29] demonstrated that the U parameters could be rigorously determined from linear-response calculations.

In spite of its central importance in understanding the accuracy of electronic-structure calculations, the concept of self-interaction is generally poorly defined. Although electronic self-interactions are known to be present in local and semilocal density-functional approxi-

mation while absent from the Hartree-Fock formulation [13], there exists no well-established criterion to determine whether a given method is exempt from self-interaction errors. The lack of explicit definition greatly complicates any attempt to evaluate, compare, and extend existing corrective schemes.

This work presents a general formalism for analyzing electronic self-interaction in the context of electronic-structure calculations and introduces a new scheme to eliminate self-interaction errors. In the next section, we propose a formal, yet intuitive, criterion for electronic self-interaction and present a parameter-free LDA + U$\alpha\beta$ method to extend the PZ-SIC scheme in the LDA + U formalism.

2.4.2 Defining Self-interaction

In mean-field descriptions of physical systems, self-interaction occurs when an element of the system interacts directly with itself through the total effective field. In the context of density-functional theory, self-interaction manifests itself in the dependence of the single-electron Hamiltonian with respect to the occupation of a given electronic state. Therefore, the following criterion for identifying electronic self-interaction can be proposed:

> *An independent-electron scheme is self-interaction free if the energy of any given orbital does not vary when changing the occupation of that orbital, all electronic orbitals and all other occupations remaining constant.*
>
> (non-self-interaction criterion)

Explicitly, this condition can be written as:

$$\frac{\partial \epsilon_{i\sigma}}{\partial f_{i\sigma}} = 0, \tag{2.14}$$

where $\psi_{i\sigma}$, $f_{i\sigma}$, and $\epsilon_{i\sigma}$ denote the electronic orbitals, the orbital occupations, and the orbital energies, respectively.

According to Janak's theorem, the single-electron energy ϵ_i equals the derivative of the total energy with respect to the orbital occupation at the electronic configuration minimizing the total energy:

$$\epsilon_{i\sigma} = \frac{\partial E}{\partial f_{i\sigma}} = \frac{dE}{df_{i\sigma}}. \tag{2.15}$$

Therefore, the condition of non-self-interaction can be recast as:

$$\frac{\partial^2 E}{\partial f_{i\sigma}^2} = 0. \tag{2.16}$$

Thus, self-interaction contributes an unphysical curvature to the dependence of the energy with respect to orbital occupations. This central observation constitutes the basis of the linear-response LDA + U method [29], which relies on adding occupation-dependent parabolic terms to the energy functional in order to cancel the second derivatives of the energy with respect to the electronic occupations.

In order to illustrate the implications of Eq. 2.16, we consider the finite-temperature Hartree Fock theory, within which the total electronic energy E_{HF} can be expressed as:

$$
\begin{aligned}
E_{HF} &= \sum_{i\sigma} f_{i\sigma} \langle i\sigma | -\frac{1}{2}\nabla^2 + v(\mathbf{r})|i\sigma\rangle + \frac{1}{2}\sum_{ij\sigma\sigma'} f_{i\sigma} f_{j\sigma'} \langle i\sigma, j\sigma' | \frac{1}{|\mathbf{r}-\mathbf{r}'|}|i\sigma, j\sigma'\rangle \\
&- \frac{1}{2}\sum_{ij\sigma} f_{i\sigma} f_{j\sigma} \langle i\sigma, j\sigma | \frac{1}{|\mathbf{r}-\mathbf{r}'|}|j\sigma, i\sigma\rangle
\end{aligned} \tag{2.17}
$$

Varying the occupation $f_{i\sigma}$ while fixing all other variational degrees of freedom, we obtain:

$$\frac{\partial^2 E_{HF}}{\partial f_{i\sigma}^2} = \langle i\sigma, i\sigma | \frac{1}{|\mathbf{r}-\mathbf{r}'|}|i\sigma, i\sigma\rangle - \langle i\sigma, i\sigma | \frac{1}{|\mathbf{r}-\mathbf{r}'|}|i\sigma, i\sigma\rangle = 0 \tag{2.18}$$

Thus, we verify that the non-self-interaction criterion given in Eq. 2.16 is equivalent to a well-known cancellation rule between the electrostatic and exchange self-interaction energies.

Additionally, for any independent-electron scheme, the ionization energy $\mathcal{E}_{i\sigma}$ of a given orbital can be expressed in terms of the single-electron energy $\epsilon_{i\sigma}$ (Slater's theorem):

$$\mathcal{E}_{i\sigma} = \int_0^1 \frac{dE}{df_{i\sigma}} df_{i\sigma} = \int_0^1 \epsilon_{i\sigma} df_{i\sigma}, \tag{2.19}$$

where the integral is evaluated along the minimal energy path connecting $f_{i\sigma} = 0$ to $f_{i\sigma} = 1$. Therefore, in the absence of self-interaction (Eq. 2.14)—and neglecting second-order relaxation effects—the ionization energy can be directly obtained from Koopmans' theorem:

$$\mathcal{E}_{i\sigma} \approx \epsilon_{i\sigma}. \tag{2.20}$$

The equivalence between Slater's theorem and Koopmans' theorem under satisfaction of Eq. 2.14 confirms the significance of self-interaction for the physical interpretation of orbital energies.

2.4.3   LDA + U$\alpha\beta$ Method

Within the Perdew-Zunger approach, the corrected energy functional E_{PZ} is expressed as:

$$E_{PZ} = E - \sum_{i\sigma} E_H[f_{i\sigma}|\psi_{i\sigma}|^2] - \sum_{i\sigma} E_{XC}[f_{i\sigma}|\psi_{i\sigma}|^2, 0], \tag{2.21}$$

where E, E_H, and E_{XC} stand for the total energy, the Hartree energy, and the local (or semilocal) spin density approximation for the exchange-correlation energy. Hence, the second derivative of the orbital-dependent energy with respect to $f_{i\sigma}$ can be expressed as:

$$\frac{\partial^2 E_{PZ}}{\partial f_{i\sigma}^2} = \langle i\sigma, i\sigma | \hat{f}_{XC}[n_\uparrow, n_\downarrow](\mathbf{r}, \mathbf{r}') | i\sigma, i\sigma \rangle$$
$$- \langle i\sigma, i\sigma | \hat{f}_{XC}[f_{i\sigma}|\psi_{i\sigma}|^2, 0](\mathbf{r}, \mathbf{r}') | i\sigma, i\sigma \rangle, \tag{2.22}$$

where $\hat{f}_{XC}[n_\uparrow, n_\downarrow](\mathbf{r}, \mathbf{r}') = [\delta^2 E_{XC}/\delta n_\sigma(\mathbf{r})\delta n_{\sigma'}(\mathbf{r}')]_{\sigma\sigma'}$ denotes the exchange-correlation kernel. As a consequence, the Perdew-Zunger self-interaction correction results in an exact cancellation of Hartree self-interaction due to the linear dependence of the electrostatic potential with respect to the electronic charge. However, it eliminates the exchange-correlation self-interaction contribution only in the limit where $\hat{f}_{XC}[n_\uparrow, n_\downarrow]$ can be approximated by $\hat{f}_{XC}[f_{i\sigma}|\psi_{i\sigma}|^2, 0]$. (This condition is satisfied, for instance, when the charge density in the background of $\psi_{i\sigma}$ is small.)

In order to extend the range of validity of the Perdew-Zunger scheme, we propose the LDA + U$\alpha\beta$ correction inspired by the LDA + U method. The LDA + U$\alpha\beta$ consists of expressing the total electronic energy as:

$$E_{LDA+U\alpha\beta} = E - \sum_{i\sigma} \frac{1}{2} U_{i\sigma} f_{i\sigma}^2 + \alpha_{i\sigma} f_{i\sigma} + \beta_{i\sigma}, \tag{2.23}$$

where the coefficients of the parabolic corrections $U_{i\sigma}$, $\alpha_{i\sigma}$, and $\beta_{i\sigma}$ are selected in order to cancel self-interaction contributions to the total energy E at the current electronic configuration. To express the self-interaction energy contribution from the orbital $\psi_{i\sigma}$, we write the

total energy in function of $f_{i\sigma}$ (all other variational parameters being kept constant):

$$E(f_{i\sigma}) = E(0) + \int_0^{f_{i\sigma}} \frac{\partial E}{\partial f_{i\sigma}}(f)df, \qquad (2.24)$$

where the derivative $\partial E/\partial f_{i\sigma}(f)$ is equal to the expectation value of the Hartree and exchange-correlation potential at $f_{i\sigma} = f$. Thus, Eq. 2.25 can be rewritten as:

$$E(f_{i\sigma}) = E(0) + \int_0^{f_{i\sigma}} \langle i\sigma| - \frac{1}{2}\nabla^2 + v + v_{HXC,i\sigma}(f)|i\sigma\rangle df, \qquad (2.25)$$

where $v_{HXC,i\sigma}(f)$ is the sum of the Hartree and exchange-correlation potentials evaluated at $f_{i\sigma} = f$, all electronic orbitals and all other occupations remaining constant. In the absence of self-interaction, the orbital-occupation dependence of the total energy becomes:

$$E(f_{i\sigma}) = E(0) + \langle i\sigma| - \frac{1}{2}\nabla^2 + v + v_{HXC,i\sigma}(0)|i\sigma\rangle f_{i\sigma}. \qquad (2.26)$$

Comparing Eq. 2.25 with Eq. 2.26, we obtain the expression of the self-interaction energy $\Delta E_{i\sigma}$ associated with the orbital $\psi_{i\sigma}$:

$$\Delta E_{i\sigma}(f_{i\sigma}) = \int_0^{f_{i\sigma}} \langle i\sigma|v_{HXC,i\sigma}(f) - v_{HXC,i\sigma}(0)|i\sigma\rangle df. \qquad (2.27)$$

In agreement with physical intuition, Eq. 2.27 indicates that the self-interaction energy corresponds to the integrated change in the total energy derivative when varying the orbital occupation from 0 to $f_{i\sigma}$. As a result, the self-interaction correction coefficients $U_{i\sigma}$, $\alpha_{i\sigma}$, and $\beta_{i\sigma}$ can be computed by matching the values of the self-interaction energy and derivatives calculated at the occupation $f_{i\sigma}$:

$$\begin{cases} \Delta E_{i\sigma} &= \int_0^{f_{i\sigma}} \langle i\sigma|v_{HXC,i\sigma}(f) - v_{HXC,i\sigma}(0)|i\sigma\rangle df \\ \partial\Delta E_{i\sigma}/\partial f_{i\sigma} &= \langle i\sigma|v_{HXC} - v_{HXC,i\sigma}(0)|i\sigma\rangle \\ \partial^2\Delta E_{i\sigma}/\partial f_{i\sigma}^2 &= \langle i\sigma, i\sigma|\hat{f}_{HXC}|i\sigma, i\sigma\rangle, \end{cases} \qquad (2.28)$$

where $v_{HXC} = v_{HXC,i\sigma}(f_{i\sigma})$ and $\hat{f}_{HXC} = \hat{f}_{HXC}[n_\uparrow, n_\downarrow]$ are evaluated at the current spin densities $n_\uparrow$ and $n_\uparrow$. It should be emphasized that the $U\alpha\beta$ self-interaction correction is exact for all electronic configurations in the vicinity of the configuration at which $\Delta E_{i\sigma}$ and its derivatives are calculated.

	LDA + U$\alpha\beta$	LDA + U
Energy functional	$E - \frac{1}{2}\sum_{i\sigma} U_{i\sigma} f_{i\sigma}^2 + \alpha_{i\sigma} f_{i\sigma} + \beta_{i\sigma}$	$E + \frac{1}{2}\sum_{m\sigma} U_{m\sigma} q_{m\sigma}(1 - q_{m\sigma})$
Orbitals	$\psi_{i\sigma}$ (Kohn-Sham)	$\phi_{m\sigma}$ (atomic)
Occupations	$f_{i\sigma}$	$q_{m\sigma} = \sum_{i\sigma} f_{i\sigma} |\langle\psi_{i\sigma}|\phi_{m\sigma}\rangle|^2$
U	$U_{i\sigma} = \langle i\sigma, i\sigma|\hat{f}_{HXC}|i\sigma, i\sigma\rangle$	$U_{m\sigma} = \langle m\sigma, m\sigma|\hat{f}_{HXC}|m\sigma, m\sigma\rangle$
α	$\alpha_{i\sigma} = \langle i\sigma|v_{HXC} - v_{HXC,i\sigma}(0)|i\sigma\rangle - U_{i\sigma} f_{i\sigma}$	$\alpha_{m\sigma} = -\frac{1}{2}U_{m\sigma}$
β	$\beta_{i\sigma} = \int_0^{f_{i\sigma}} \langle i\sigma|v_{HXC,i\sigma}(f) - v_{HXC,i\sigma}(0)|i\sigma\rangle df$ $- \frac{1}{2}U_{i\sigma} f_{i\sigma}^2 - \alpha_{i\sigma} f_{i\sigma}$	$\beta_{m\sigma} = 0$

Table 2.1: Comparison between the LDA + U$\alpha\beta$ and LDA + U methods.

The LDA + U$\alpha\beta$ functional share common features with the linear-response method proposed by Cococcioni and de Gironcoli. A comparison of the two approaches is given in Table 2.1. Within the linear-response approach, the Hubbard U coefficient corresponding to a given atomic-like orbital $\phi_{m\sigma}$ of effective occupation $q_{m\sigma} = \sum_{i\sigma} f_{i\sigma}|\langle\psi_{i\sigma}|\phi_{m\sigma}\rangle|^2$ is expressed as:

$$U_{m\sigma} = \langle m\sigma, m\sigma|\hat{\chi}^{-1} - \hat{\chi}_0^{-1}|m\sigma, m\sigma\rangle \tag{2.29}$$

where $\hat{\chi}(\mathbf{r}, \mathbf{r}') = [\delta n_\sigma(\mathbf{r})/\delta v_{\sigma'}(\mathbf{r}')]_{\sigma\sigma'}$ denotes the response function to the external potential, and $\chi_0(\mathbf{r}, \mathbf{r}') = [\delta n_\sigma(\mathbf{r})/\delta v_{\sigma'}^{eff}(\mathbf{r}')]_{\sigma\sigma'}$ stands for the response function to the mean-field effective potential. The two response operators entering into Eq. 2.29 differing only by the linear response of the Hartree and exchange-correlation potentials, the self-interaction curvature $U_{m\sigma}$ can be recast as:

$$U_{m\sigma} = \langle m\sigma, m\sigma|\hat{f}_{HXC}|m\sigma, m\sigma\rangle, \tag{2.30}$$

an expression similar to that in Eq. 2.28. However, it should be noted that at variance with the LDA + U$\alpha\beta$ scheme, the LDA + U method relies on predefined atomic orbtials and sets the self-interaction correction coefficients $\alpha_{m\sigma}$ and $\beta_{m\sigma}$ to be equal to $-\frac{1}{2}U_{m\sigma}$ and 0, respectively, thereby replacing double-counting terms in the energy functional with effective Hubbard interactions [29].

The main difficulty in directly minimizing the LDA + U$\alpha\beta$ energy (Eq. 2.23) lies in taking into account the variational dependence of the self-interaction coefficients $U_{i\sigma}$, $\alpha_{i\sigma}$, and $\beta_{i\sigma}$— which requires calculating the third-order functional derivative of the exchange-correlation

energy $\delta^3 E_{XC}/\delta n(\mathbf{r})\delta n(\mathbf{r}')\delta n(\mathbf{r}'')$, in particular. To bypass this difficulty, we propose an indirect self-consistent scheme that consists of selecting a reference electronic configuration $\{f_{i\sigma}^0, \psi_{i\sigma}^0\}$ for calculating the self-interaction coefficients. Explicitly, the LDA $+$ U$\alpha\beta$ energy and Hamiltonian are expressed as:

$$E_{LDA+U\alpha\beta} \;=\; E - \sum_{i\sigma} \frac{1}{2}U_{i\sigma}^0 (q_{i\sigma}^0)^2 + \alpha_{i\sigma}^0 q_{i\sigma}^0 + \beta_{i\sigma}^0 \tag{2.31}$$

$$\hat{h}_{LDA+U\alpha\beta}^{eff} \;=\; -\frac{1}{2}\nabla^2 + v + v_{HXC} - \sum_{i\sigma} |i\sigma^0\rangle U_{i\sigma}^0 q_{i\sigma}^0 + \alpha_{i\sigma}^0 \langle i\sigma^0|, \tag{2.32}$$

where $q_{i\sigma}^0 = \sum_{j\sigma} f_{j\sigma}|\langle \psi_{j\sigma}|\psi_{i\sigma}^0\rangle|^2$ is the effective occupation of the reference orbital $\psi_{i\sigma}^0$.

It is important to note that in the vicinity of the reference configuration, $q_{i\sigma}^0$ and $f_{i\sigma}^0$ are nearly equal, which results in the following approximation for the effective Hamiltonian:

$$\hat{h}_{LDA+U\alpha\beta}^{eff} \approx -\frac{1}{2}\nabla^2 + v + v_{HXC} + \sum_{i\sigma} |i\sigma^0\rangle\langle i\sigma^0|v_{HXC,i\sigma}^0(0) - v_{HXC}^0|i\sigma^0\rangle\langle i\sigma^0|,$$

where $v_{HXC,i\sigma}^0(0)$ and $v_{HXC}^0 = v_{HXC,i\sigma}^0(f_{i\sigma}^0)$ are calculated at the reference electronic configuration. Eq. 2.33 offers an intuitive interpretation of the LDA $+$ U$\alpha\beta$ self-consistent procedure: provided that the current electronic configuration $\{f_{i\sigma}, \psi_{i\sigma}\}$ does not deviate significantly from the reference configuration $\{f_{i\sigma}^0, \psi_{i\sigma}^0\}$, each orbital $\psi_{i\sigma} \approx \psi_{i\sigma}^0$ is effectively subject to a potential $v_{i\sigma}^{eff} \approx v + v_{HXC,i\sigma}(0)$ that does not include its own contribution. In other words, the self-interaction correction substitutes $v_{HXC,i\sigma}(0)$ for $v_{HXC} = v_{HXC,i\sigma}(f_{i\sigma})$ in the proximity of the self-consistent reference configuration.

We now present the LDA $+$ U$\alpha\beta$ self-consistent algorithm. Let N^{SCF} denote the number of self-consistent field (SCF) steps between each update of the reference configuration.

<hr>

LDA + U$\alpha\beta$ Algorithm

1. Select an initial reference electronic configuration $\{f_{i\sigma}^0, \psi_{i\sigma}^0\}$.

2. Calculate the self-interaction coefficients $U_{i\sigma}^0$, $\alpha_{i\sigma}^0$, and $\beta_{i\sigma}^0$ corresponding to the reference electronic configuration $\{f_{i\sigma}^0, \psi_{i\sigma}^0\}$.

3. Perform N^{SCF} Kohn-Sham self-consistent steps with the LDA + U$\alpha\beta$, updating the effective occupations $q_{i\sigma}^0 = \sum_{j\sigma} f_{j\sigma} |\langle \psi_{j\sigma} | \psi_{i\sigma}^0 \rangle|^2$ during each minimization.

4. Set the new reference electronic configuration to be equal to the current configuration: $\{f_{i\sigma}, \psi_{i\sigma}\} \rightarrow \{f_{i\sigma}^0, \psi_{i\sigma}^0\}$.

5. Iterate from Step 2 until SCF convergence is achieved.

<hr>

Note that the current and reference electronic configurations become identical at convergence. Therefore, the LDA + U$\alpha\beta$ self-consistent algorithm ensures satisfaction of the non-self-interaction condition (Eq. 2.16).

Step 2 of the algorithm requires calculating the kernel of the local or semilocal exchange-correlation energy $\hat{f}_{XC}$. This calculation is performed using the method proposed by Dal Corso and de Gironcoli in the context of phonon-dispersion computations [30]. Moreover, the determination of the self-interaction coefficients necessitates calculating the Hartree self-interaction energies $\int |\psi_{i\sigma}|^2(\mathbf{r})|\psi_{i\sigma}|^2(\mathbf{r}')/|\mathbf{r} - \mathbf{r}'| d\mathbf{r} d\mathbf{r}'$, which entails treating a system with a net electrical charge. To eliminate periodic-image errors [31] in our plane-wave calculations, we employed the density-countercharge method (DCC) introduced in the next chapter. Since computing the $\hat{f}_{HXC}$ and of $v_{HXC,i\sigma}$ is relatively inexpensive and is only done every N^{SCF} Kohn-Sham iterations, the overall cost of the LDA + U$\alpha\beta$ calculation is comparable to that of standard LDA calculations.

As a final note, it is worth pointing out that the LDA + U$\alpha\beta$ algorithm can be modified to exactly reproduce the PZ-SIC correction. The adaptation of the LDA + U$\alpha\beta$ to the PZ-SIC scheme consists of changing the reference configuration $\{f_{i\sigma}^0, \psi_{i\sigma}^0\}$ in the calculation of the self-interaction coefficients (Step 2). Specifically, when determining the PZ-SIC coefficients $U_{i\sigma}^{0,PZ}$, $\alpha_{i\sigma}^{0,PZ}$, and $\beta_{i\sigma}^{0,PZ}$, the following substitutions must be made:

$$\begin{cases} f_{j\sigma'}^0 \rightarrow 0 & \text{if } (j,\sigma') \neq (i,\sigma) \\ f_{i\sigma}^0 \rightarrow f_{i\sigma}^0. \end{cases} \tag{2.33}$$

<hr>

Figure 2-1: LDA + U$\alpha\beta$, LDA, and exact Born-Oppenheimer hydrogen energies as the function of the fractional occupation of the electronic orbital.
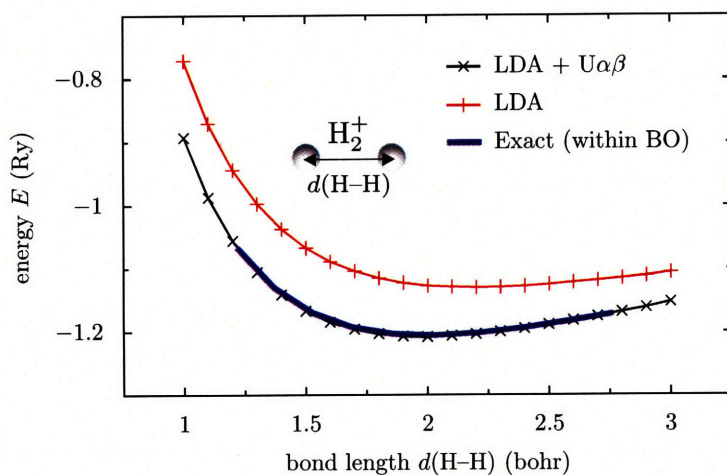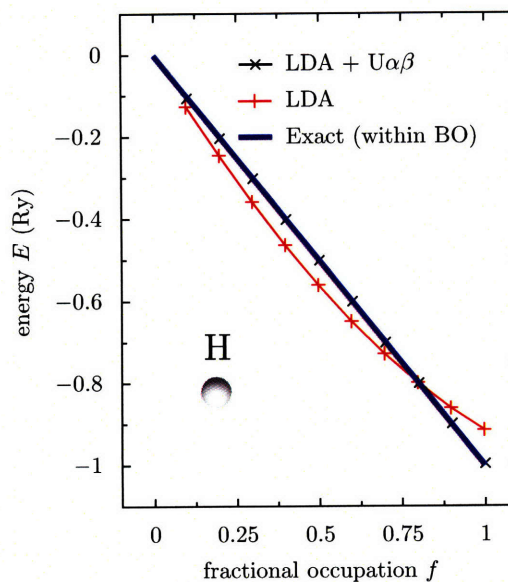
Figure 2-2: LDA + U$\alpha\beta$, LDA, and exact Born-Oppenheimer potential-energy curves of H_2^+.

In addition to computational efficiency, one of the main advantages of the above scheme lies in the fact that it does not require additional orthogonality constraints in the electronic minimization at variance with the PZ-SIC scheme.

2.4.4   Application to Archetypal Self-interaction Problems

In order to probe the performance of the LDA + U$\alpha\beta$ scheme, we first consider an ionized hydrogen atom. The total energy of the atom as a function of the fractional occupation of its electronic orbital is reported in Figure 2-1. In this calculation, we use a self-interaction-

Figure 2-3: LDA + U$\alpha\beta$, LDA, and unrestricted Hartree-Fock potential-energy curves of H_2.
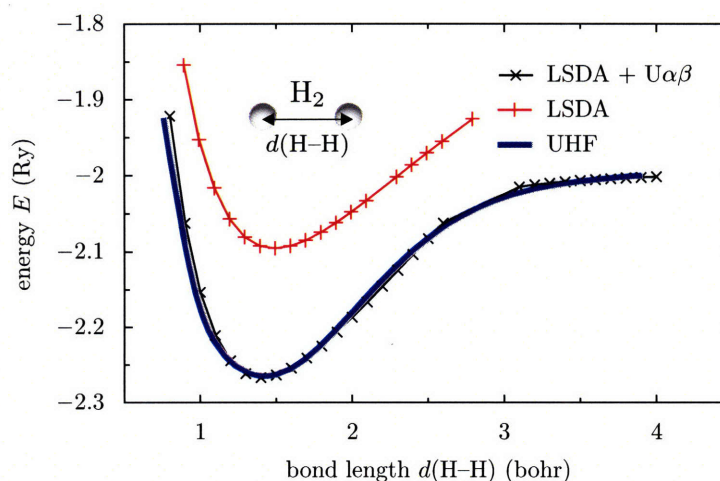
free hydrogen pseudopotential (generated by canceling the exchange-correlation term in the effective Hamiltonian) and employ the local density approximation (Eq. 2.3). We observe that the LDA ionization curve deviates significantly from the expected linear behavior [32]. Indeed, at low fractional occupations, the LDA functional overestimates the stability of the hydrogen ion, reflecting the predominance of the exchange energy (scaling as $f^{4/3}$) over the electrostatic contribution (scaling as f^2). At higher occupancy, the LDA functional underestimates the absolute value of the total energy. In contrast, the ionization curve calculated using the LDA + U$\alpha\beta$ method is seen to follow the expected linear trend, reflecting the invariance of the single-electron Hamiltonian with respect to the occupation f. It should also be mentioned that at full orbital occupancy, the LDA + U$\alpha\beta$ electronic eigenenergy equals -1.0 Ry (in accordance with Koopmans' theorem) while its LDA counterpart is calculated to be -0.47 Ry, confirming the limited physical relevance of uncorrected LDA single-electron energies.

We now compare the exact Born-Oppenheimer potential-energy curve of H_2^+ [33] to LDA and LDA + U$\alpha\beta$ predictions (Figure 2-2). We observe that while the LDA energies are overestimated by about 0.1 Ry in the vicinity of the equilibrium bond length, the LDA + U$\alpha\beta$ values closely agree with those obtained from exact calculations. This agreement confirms the accuracy of the U$\alpha\beta$ corrective approach for describing one-electron systems—in which total-energy errors are entirely due to self-interaction effects.

As an additional illustration of the performance of the corrective approach, we consider the potential energy of a H_2 molecule as a function of bond length using the unrestricted Hartree-Fock (UHF), the local spin-density approximation (LSDA), and the LSDA + U$\alpha\beta$ methods.

The results are reported in Figure 2-3 (note that the self-consistent energy-minimization procedure becomes unstable around $d(H\text{–}H) = 3$ bohr, close to the Coulson-Fischer dissociation limit [34]). Similarly to the H_2^+ calculations, we note that the LSDA calculations underestimates the stability of the molecules. As expected, we also observe that *in the absence correlation contribution*, the U$\alpha\beta$ correction brings the potential energy in close agreement with UHF results.

The above comparative analysis confirms the ability of the LDA $+$ U$\alpha\beta$ method to correct self-interaction errors in important benchmark cases. Furthermore, they demonstrate that the three-parameter occupation-dependent U$\alpha\beta$ term is sufficiently flexible to achieve the accuracy of orbital-dependent schemes—such as the Perdew-Zunger correction [32]—with a significantly lower computational cost. These results establish the LDA $+$ U$\alpha\beta$ approach as a promising computational scheme to eliminate self-interaction errors in density-functional theory calculations.

Electrostatics of Polarized and Charged Systems in Periodic Boundary Conditions

3.1 Introduction

FIRST-PRINCIPLES CALCULATIONS frequently employ periodic boundary conditions to predict materials properties. Besides constituting a natural choice when studying crystalline systems, periodic boundary conditions allow the use of highly optimized fast Fourier transform (FFT) algorithms [35–37], which considerably reduce the computational cost associated with the resolution of electrostatic equations, and allow an efficient evaluation of electronic kinetic energies and interatomic forces when used in conjunction with a plane-wave basis set. Despite these algorithmic advantages, periodic boundary conditions require large supercells when studying aperiodic or partially periodic systems (e.g., isolated molecules, polymer chains, and slabs) in an effort to minimize spurious electrostatic interactions between periodic images [38]. Charged systems are particularly problematic, since conventional algorithms automatically enforce charge neutrality by introducing an artificial jellium background [38]. (Note that the electrostatic energy of a charged system exhibiting three-dimensional periodicity is infinite.) As shown by Makov and Payne, these artifacts induce significant errors scaling as $1/L^3$ for the energy of neutral polarized systems and $1/L$ for that of charged systems, where L denotes the size of the unit cell [31].

In addition to the Makov-Payne asymptotic correction [31], several schemes have been devised to reduce periodic-image errors. Barnett and Landman proposed to eliminate periodic-image interactions for cluster systems by restricting the plane-wave expansions of the wave-

functions and of the charge density to a spherical domain in reciprocal space [39–41]. A generalization of this reciprocal-space approach was introduced by Martyna and Tuckerman [42]. The electrostatic-cutoff approach proposed by Jarvis, White, Godby, and Payne suppresses periodic-image effects by damping the electrostatic potential beyond a certain interaction range [43]. The corrective method introduced by Blöchl consists of using atom-centered Gaussian charges and Ewald summation techniques to cancel periodic-image interactions [44]. In the local-moment-countercharge (LMCC) method developed by Schultz, a superposition of Gaussians is employed as a local-moment model for calculating the Coulomb potential analytically up to a certain multipole order, the remaining electrostatic contribution being computed using conventional plane-wave techniques [45]. Considering atomic adsorption on neutral slabs, Neugebauer and Scheffler proposed eliminating the adsorbate-induced polarization through the introduction of a counteracting planar dipole between slab images [46]. Refinements of this method, based on the linear- and planar-average approximations proposed by Baldereschi, Baroni, and Resta [47], were subsequently developed [48–50]. Extending this approach to charged surfaces, the prescription of Lozovoi and Alavi relies on inserting a Gaussian layer in vacuum to compensate for the excess charge and to allow electric-field discontinuities across the layer [51].

In this work, we propose an alternative approach for correcting periodic-image errors and show that exponential energy convergence with respect to cell size can be obtained at tractable computational cost. The approach proceeds by calculating the electrostatic potential in real space, exploiting the periodic solution of the Poisson equation computed using inexpensive FFT techniques. In the following sections, we first discuss and characterize the difference between the open-boundary electrostatic potential and its periodic counterpart, providing a comparative basis for analyzing the relative accuracy of various corrective schemes. Second, we present our correction method and assess its performance. Last, we extend the method to the study of systems exhibiting one- or two-dimensional periodicity, beyond the conventional linear- and planar-average approximations.
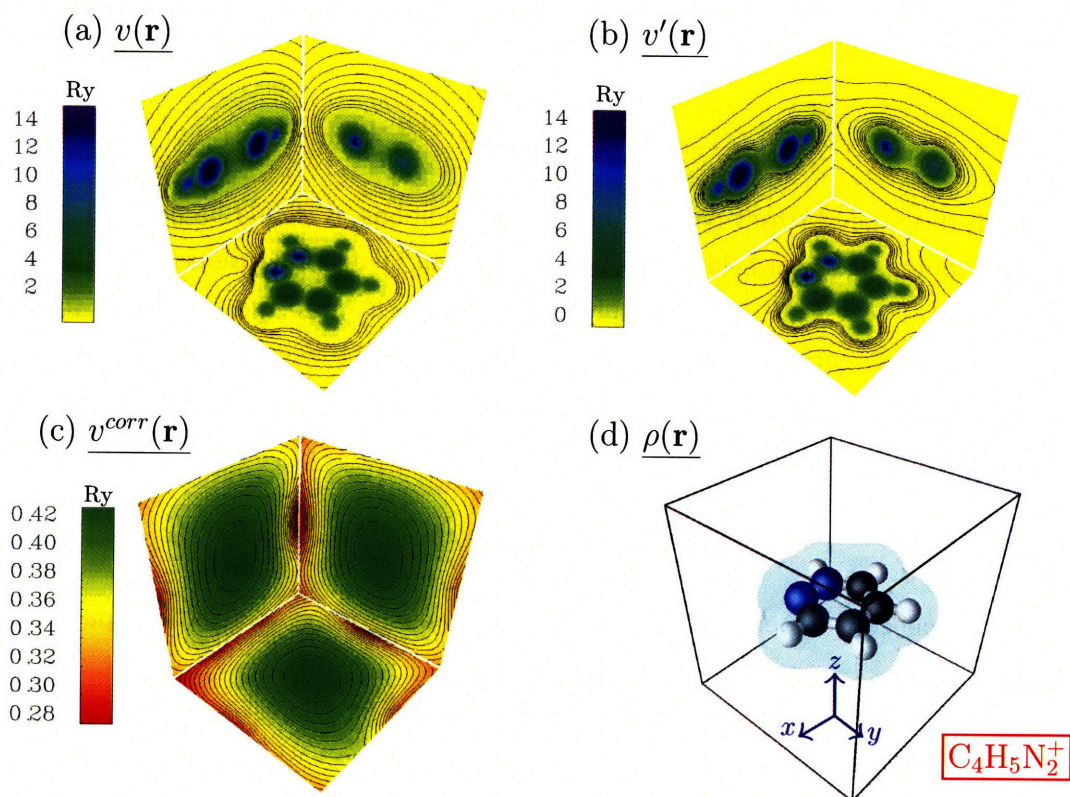
Figure 3-1: (a) Open-boundary electrostatic potential v, (b) periodic electrostatic potential v', and (c) electrostatic-potential correction $v^{corr} = v - v'$ for a pyridazine cation in a cubic cell of length $L = 15$ bohr. The potentials are plotted in three orthogonal planes (Oxy), (Oxz), and (Oyz) passing through the center of the cell.

3.2 Comparison of the Open-boundary and Periodic Potentials

3.2.1 Definition of the Corrective Potential

The electrostatic potential v generated by a charge distribution ρ satisfies the Poisson equation:

$$\nabla^2 v(\mathbf{r}) = -4\pi \rho(\mathbf{r}) \tag{3.1}$$

(atomic units are used throughout). In the absence of an external electric field, we can solve Eq. 3.1 subject to open-boundary conditions ($v(\mathbf{r}) \to 0$ as $|\mathbf{r}| \to +\infty$). As a result, the

electrostatic potential v can be computed via Coulomb integration:

$$v = \int \frac{\rho(\mathbf{r}')}{|\mathbf{r} - \mathbf{r}'|} d\mathbf{r}'. \tag{3.2}$$

(Although this study focuses on open boundary conditions, it should be noted that the contribution from an external field $\mathbf{E}$ can be incorporated by adopting the asymptotic boundary conditions $v(\mathbf{r}) \rightarrow -\mathbf{E} \cdot \mathbf{r}$, which simply adds a term $-\mathbf{E} \cdot \mathbf{r}$ to the solution of the Poisson equation.) A differential equation similar to Eq. 3.1 can be written for the periodic potential v', keeping in mind that periodic boundary conditions can only accommodate a net zero charge (as seen from Gauss' law):

$$\nabla^2 v'(\mathbf{r}) = -4\pi(\rho(\mathbf{r}) - \langle\rho\rangle). \tag{3.3}$$

As a consequence, the periodic potential can be evaluated in the reciprocal-space representation as:

$$v'(\mathbf{r}) = \sum_{\mathbf{g}\neq 0} \frac{4\pi}{\mathbf{g}^2}\rho(\mathbf{g})e^{i\mathbf{g}\cdot\mathbf{r}}, \tag{3.4}$$

where we set the arbitrary component $v'(\mathbf{g} = 0) = \langle v'\rangle$ to zero.

It should be noted that the open-boundary potential v and its periodic counterpart v' are distinct. We define the corrective potential v^{corr} as the difference $v - v'$. The potential v^{corr} must satisfy:

$$\nabla^2 v^{corr}(\mathbf{r}) = -4\pi\langle\rho\rangle, \tag{3.5}$$

for which we specify Dirichlet boundary conditions: $v^{corr} = v - v'$ at the cell boundaries. (Note that the solution of this elliptic boundary value problem [52, 53] is uniquely defined.) Eq. 3.5 indicates that the curvature of the corrective potential is a constant. It should also be noted that, apart from the value of the average $\langle\rho\rangle$, Eq. 3.5 is independent of the structural details of the charge density ρ. Instead, these details are entirely embedded in the Dirichlet boundary conditions, which reflect the electrostatic contributions from compensating jellium and from the surrounding images.

In order to illustrate the implications of Eq. 3.5, we consider a pyridazine cation in a periodically repeated cubic cell. The open-boundary potential v, the periodic potential v', and the corrective potential v^{corr} are shown in Figure 3-1. First, we observe that the potential v' is shifted down in energy with respect to v, due to the fact that the average $\langle v'\rangle$ is null by construction. In addition to this energy shift, the potential v' is significantly distorted. This

Figure 3-2: Open-boundary electrostatic potential v, periodic potential v', and electrostatic-potential correction v^{corr} averaged in the xy-plane parallel to the surface for (a) carbon monoxide adsorbed on a neutral platinum slab, and (b) carbon monoxide adsorbed on a charged platinum slab.
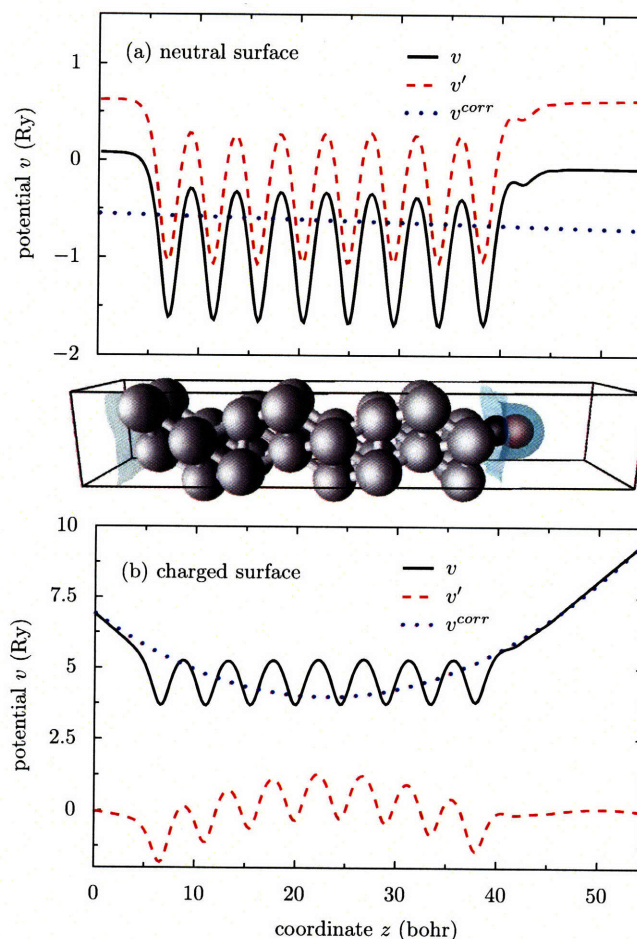
distortion results from satisfying the periodicity conditions. Most importantly, we observe that the corrective potential v^{corr} varies smoothly over space. The smooth spatial dependence of v^{corr} contrasts markedly with the strong variations in v and in v'. Performing a polynomial regression, we can verify that the potential v^{corr} is quadratic to good approximation in the proximity of the cell center with departures from parabolicity restricted to the vicinity of the periodic boundaries.

To further examine the characteristics of v^{corr}, we consider the adsorption of carbon monoxide molecules on neutral and charged platinum slabs. Following Neugebauer and Scheffler, the electrostatic correction is calculated along the z-direction within the planar-average approximation (that is, from the xy-average of the charge distribution) [47]. The validity of this approximation is discussed in the last section. For CO molecules adsorbed on a neutral slab (Figure 3-2a), the periodic potential is shifted up in energy and tilted with respect to
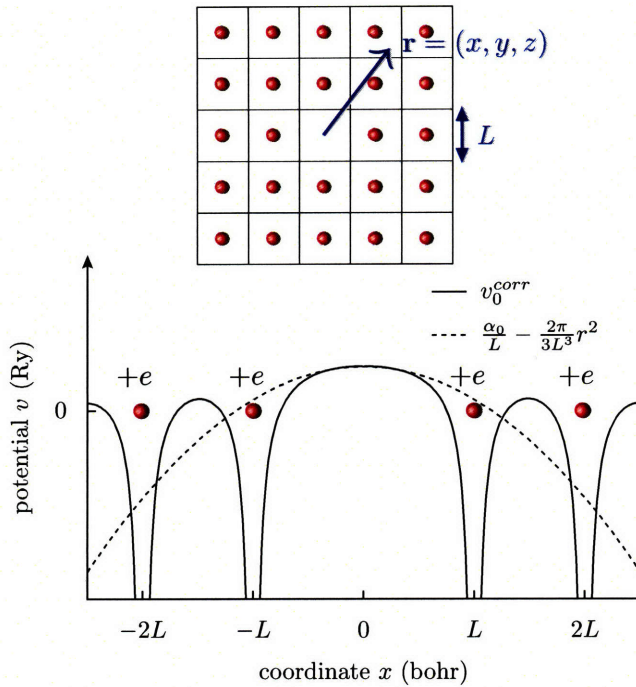
Figure 3-3: Corrective potential v_0^{corr} for a cubic lattice of point charges and its parabolic approximation in the vicinity of the origin.

the open-boundary potential. The potential correction is seen to be linear, in agreement with the analysis of Neugebauer and Scheffler [46]. For CO molecules adsorbed on a slab of surface charge $\tilde{\sigma}$ (Figure 3-2b), the real-space potential diverges as $4\pi\tilde{\sigma}|z|$. In this case, the periodic potential v' undergoes a significant energy downshift, which decreases the energy of the positively charged slab. Moreover, we observe that v' is significantly curved in the slab region. Consistent with these observations and with Eq. 3.5, the corrective potential v^{corr} is found to be parabolic everywhere in the unit cell.

3.2.2 Quasiparabolic Behavior of the Corrective Potential

In order to complete the analysis of the corrective potential, we consider a point charge $q = +e$ in a periodically repeated cubic cell of length L, as illustrated in Figure 3-3. The corrective potential generated by the uniform jellium and the surrounding point charges is denoted v_0^{corr}. Note that v_0^{corr} cannot be calculated directly as the difference between the potential of a lattice of point charges v_0' and the point-charge potential $1/r$ since the representation of a point charge in reciprocal space requires an infinite number of plane-wave components. Instead, to obtain v_0^{corr}, we can exploit the cubic symmetry of the system, writing the corrective potential

as:

$$v_0^{corr}(\mathbf{r}) = v_0^{corr}(r = 0)$$
$$+ \nabla^2 v_0^{corr}(r = 0)\frac{r^2}{6} + O(|\mathbf{r}|^4). \tag{3.6}$$

This parabolic expansion, valid up to third order, confirms that the point-charge correction v_0^{corr} is almost quadratic in the vicinity of $r = 0$. For noncubic lattices, due to inversion symmetry, the point-charge corrective potential takes a more general form:

$$v_0^{corr}(\mathbf{r}) = v_0^{corr}(r = 0)$$
$$+ \frac{1}{2}\sum_\alpha \frac{\partial^2 v_0^{corr}}{\partial r_\alpha^2}(r = 0)r_\alpha^2 + O(|\mathbf{r}|^4), \tag{3.7}$$

where (r_α) are the coordinates of $\mathbf{r}$ along the principal axes. Thus, the corrective potential in a noncubic lattice is also quasiparabolic.

Turning now to an arbitrary distribution ρ, we can express the electrostatic correction v^{corr} by superposition:

$$v^{corr}(\mathbf{r}) = \int v_0^{corr}(\mathbf{r} - \mathbf{r}')\rho(\mathbf{r}')d\mathbf{r}'. \tag{3.8}$$

As a consequence, defining r_{max} as the distance beyond which the parabolic expansion (Eq. 3.6) ceases to be valid, the corrective potential v^{corr} can be considered as nearly parabolic, provided that the spread of the distribution is tolerably lower than r_{max}.

3.2.3 Connection with Existing Schemes

Having justified the general characteristics of the electrostatic-potential correction, we now determine the terms in the expansion of v_0^{corr} (Eq. 3.6). The potential at the origin $v_0^{corr}(r = 0)$ can be written in terms of the Madelung constant α_0 [54] of a cubic lattice of point charges in a compensating jellium background:

$$v_0^{corr}(r = 0) = \frac{\alpha_0}{L}. \tag{3.9}$$

(The calculation of the Madelung constant of a jellium-neutralized assembly of point charges is discussed in Appendix A.) Note that $v_0^{corr}(r = 0)$ is positive, reflecting the stabilizing contribution from the jellium compensation. The value of $\nabla^2 v_0^{corr}(r = 0)$ is then determined
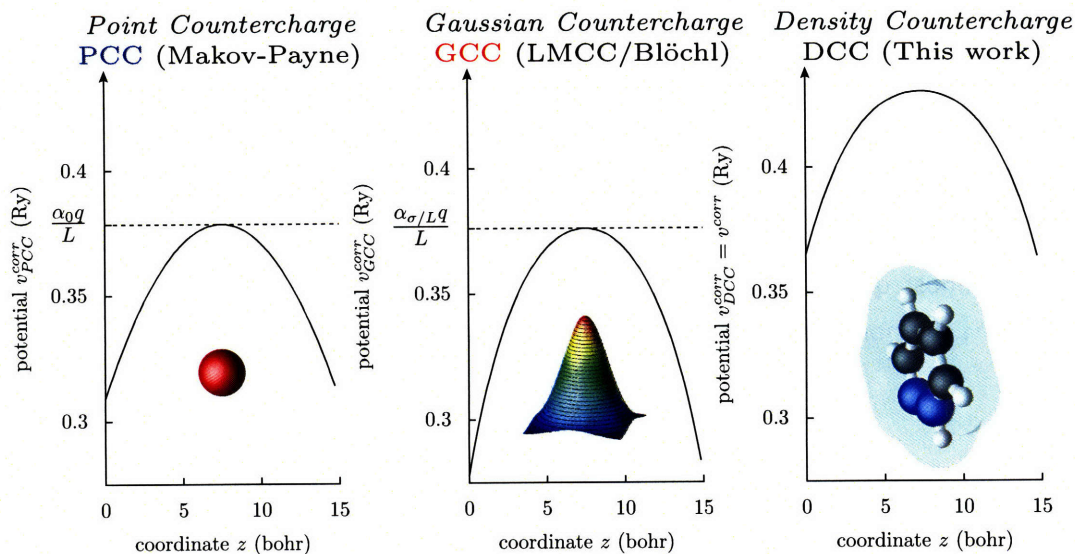
Figure 3-4: Point-countercharge (PCC), Gaussian-countercharge (GCC), and density-countercharge (DCC) corrective potentials for a pyridazine cation $C_4H_5N_2^+$ in a cubic cell of length $L = 15$ bohr. The corrective potentials are plotted along the z-axis perpendicular to the plane of the molecule, as defined in Figure 3-1. The PCC and GCC corrections are calculated up to dipole order. The spread of the Gaussian countercharges is $\sigma = 0.5$ bohr.

from Eq. 3.5:

$$\nabla^2 v_0^{corr}(r = 0) = -\frac{4\pi}{L^3}. \tag{3.10}$$

Hence, the point-charge correction can be expanded as:

$$v_0^{corr}(\mathbf{r}) = \frac{\alpha_0}{L} - \frac{2\pi}{3L^3}r^2 + O(|\mathbf{r}|^4). \tag{3.11}$$

The terms in this parabolic expansion bear a strong resemblance to those entering into the Makov-Payne correction [31]. This correspondence is discussed further in Sec. 3.2.4.

The above expansion allows us to approximate the electrostatic correction induced by a set of compensating charges. Indeed, introducing N charges, we can define a parabolic point-countercharge (PCC) potential v_{PCC}^{corr} as:

$$v_{PCC}^{corr}(\mathbf{r}) = \sum_{n=1}^{N} q_n \left(\frac{\alpha_0}{L} - \frac{2\pi}{3L^3}(\mathbf{r} - \mathbf{r}_n)^2 \right). \tag{3.12}$$

This expression may be rewritten:

$$v_{PCC}^{corr}(\mathbf{r}) = \frac{\alpha_0 q}{L} - \frac{2\pi q}{3L^3}r^2 + \frac{4\pi}{3L^3}\mathbf{p}\cdot\mathbf{r} - \frac{2\pi Q}{3L^3},\tag{3.13}$$

where $q = \sum_n q_n$ is the total charge, $\mathbf{p} = \sum_n q_n\mathbf{r}_n$ denotes the total dipole moment, and $Q = \sum_n q_n r_n^2$ stands for the total quadrupole moment of the countercharge distribution. Eq. 3.13 indicates that parabolic PCC schemes can correct periodic-image errors up to quadrupole-moment order. Note that no more than $N_{max} = 7$ countercharges are sufficient to obtain the most accurate parabolic correction (one charge for q, two for $\mathbf{p}$, and four for Q). To obtain higher-order PCC corrections, one would need to determine more terms in the expansion of the point-charge correction, beyond the parabolic contributions. An example of accurate calculations using harmonic expansions can be found in Ref. [55].

An alternative approach is to employ countercharges whose corrective potential can be computed handily. A popular choice is to use Gaussian densities, as proposed by Blöchl [44]. Repeating the preceding analysis for a Gaussian density of charge $q = +e$, we can expand the Gaussian corrective potential $v_{\sigma,L}^{corr}$ as:

$$v_{\sigma,L}^{corr} = \frac{\alpha_{\sigma/L}}{L} - \frac{2\pi}{3L^3}r^2 + O(|\mathbf{r}|^4),\tag{3.14}$$

where $\alpha_{\sigma/L}$ is the Madelung constant of an assembly of Gaussians of width σ immersed in a compensating jellium in a cubic cell of length L. It is more convenient, however, to write the corrective potential directly as:

$$\begin{aligned}v_{\sigma,L}^{corr}(\mathbf{r}) &= v_\sigma(\mathbf{r}) - v_{\sigma,L}'(\mathbf{r})\\ &= \frac{\mathrm{erf}(r/\sigma)}{r} - \frac{1}{L^3}\sum_{\mathbf{g}\neq 0}\frac{4\pi}{g^2}e^{-\sigma^2 g^2/4}e^{i\mathbf{g}\cdot\mathbf{r}},\end{aligned}\tag{3.15}$$

where v_σ is the electrostatic potential of an isolated Gaussian charge, and $v_{\sigma,L}'$ is the potential corresponding to a periodically repeated Gaussian in a jellium background. The sum in the right-hand side of the equation converges very rapidly, and can be calculated using FFT techniques. Superimposing N compensating charges, the Gaussian-countercharge (GCC) corrective potential v_{GCC}^{corr} can be expressed as:

$$v_{GCC}^{corr}(\mathbf{r}) = \sum_{n=1}^{N} q_n v_{\sigma,L}^{corr}(\mathbf{r} - \mathbf{r}_n).\tag{3.16}$$

This results in the following approximation for the open-boundary potential v:

$$v(\mathbf{r}) \approx v'(\mathbf{r}) + v_{GCC}^{corr}(\mathbf{r}).$$ (3.17)

We underscore that this scheme is equivalent to the Gaussian scheme introduced by Blöchl [44] and the LMCC method proposed by Schultz [45]. The equivalence with LMCC approach can be established by recasting Eq. 3.17 as:

$$\begin{cases} v(\mathbf{r}) \approx v_{PBC}(\mathbf{r}) + v_{GCC}(\mathbf{r}) \\ v_{PBC}(\mathbf{r}) = v'(\mathbf{r}) - v'_{GCC}(\mathbf{r}), \end{cases}$$ (3.18)

where $v_{GCC}(\mathbf{r}) = \sum q_n v_\sigma(\mathbf{r} - \mathbf{r}_n)$ is the electrostatic potential generated by the isolated countercharge distribution, and $v'_{GCC}(\mathbf{r}) = \sum q_n v'_{\sigma,L}(\mathbf{r} - \mathbf{r}_n)$ is the corresponding periodic potential.

We are now in a position to compare the corrective potentials v_{PCC}^{corr} and v_{GCC}^{corr} with the potential v^{corr}, obtained as the direct difference between the open-boundary potential and its periodic counterpart. For our comparative analysis, we refer to the exact corrective potential v^{corr} as the density-countercharge (DCC) potential. The DCC potential is obtained by evaluating the Coulomb integral defining v at each grid point in the unit cell. (A cheaper alternative to this procedure is presented in the next section.) The PCC, GCC, and DCC potentials for a charged pyridazine cation in a cubic cell of length $L = 15$ bohr are plotted in Figure 3-4. The PCC and GCC corrections are computed up to dipole order. First, it should be noted that the maximal energy of the PCC potential is slightly above its GCC counterpart, reflecting the fact that the Madelung energy of an array of point charges immersed in a jellium is higher than that of a jellium-neutralized array of Gaussian charges (cf. Appendix A). In addition, the maximal DCC energy is found to be approximately 0.05 Ry above $\alpha_0 q/L$, indicating that the dipole PCC and GCC corrections tend to underestimate the energy of the system. Moreover, the parabolic PCC potential is not as steep as its GCC counterpart, suggesting that the energy underestimation will be more significant for the GCC correction. Owing to the cubic symmetry of the cell, the PCC and GCC potentials display the same curvature in each direction of space, equal to one third of $-4\pi\langle\rho\rangle$. In contrast, the curvature of the DCC potential is not uniform, due to the nonspherical nature of the molecular charge density. This shape dependence suggests that the accuracy of the GCC correction could be improved by optimizing the geometry of the Gaussian countercharges.

In summary, we have shown that the PCC (Makov-Payne), GCC (LMCC), and DCC cor-
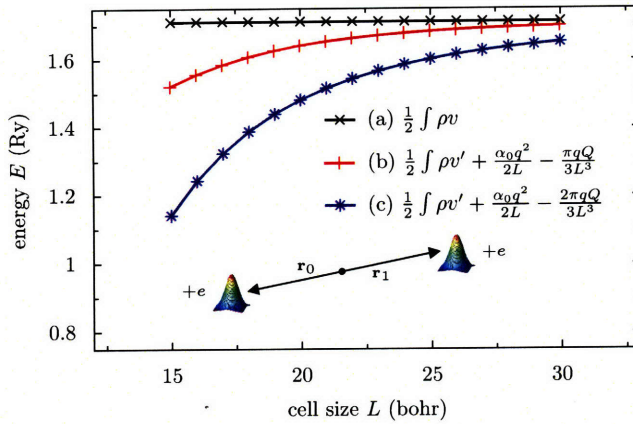
Figure 3-5: Electrostatic energy of two Gaussians of unit charge and unit spread calculated via (a) real-space integration, (b) reciprocal-space integration with the PCC energy correction given by Eq. 3.21, and (c) reciprocal-space integration with the Makov-Payne energy correction given by Eq. 15 in Ref. [31]. The Gaussian charges are positioned at $\mathbf{r}_0 = (-5, -5, -5)$ and $\mathbf{r}_1 = (5, 5, 5)$ (corresponding to a quadrupole moment Q of 153 a.u.).

rections belong to the same class of periodic-image corrections. The analysis of the corrective potential has established that the parabolic PCC correction cannot eliminate periodic-image interactions beyond quadrupole order. Difficulties inherent in the GCC scheme have also been evidenced. To overcome these limitations, an efficient implementation of the DCC correction is presented in Sec. 3.3.

3.2.4 Energy Correction

To conclude this preliminary analysis, we give the expression of the energy correction ΔE^{corr} in terms of the corrective potential v^{corr}. The total electrostatic energy of the system being equal to:

$$E = \frac{1}{2} \int v(\mathbf{r})\rho(\mathbf{r})d\mathbf{r}, \tag{3.19}$$

the corrective energy can be expressed as [48]:

$$\Delta E^{corr} = \frac{1}{2} \int v^{corr}(\mathbf{r})\rho(\mathbf{r})d\mathbf{r}. \tag{3.20}$$

it is worth mentioning that in the case of a single point countercharge $q = \int \rho(\mathbf{r})d\mathbf{r}$, the

PCC energy correction can be written as:

$$\Delta E_0^{corr} = \frac{1}{2} \int q v_0^{corr}(\mathbf{r}) \rho(\mathbf{r}) d\mathbf{r}$$

$$= \frac{\alpha_0 q^2}{2L} - \frac{\pi q Q}{3L^3}. \tag{3.21}$$

The first term corresponds to the Madelung energy correction, as proposed by Leslie and Gillian [38]. Note that the second term differs from Eq. 15 in Ref. [31] by a factor 1/2. The validity of the energy correction given by Eq. 3.21 is illustrated in Figure 3-5.

3.3   Implementation of the Density-countercharge Correction

3.3.1   Density-countercharge Algorithm

In the preceding section, the corrective potential $v^{corr} = v_{DCC}^{corr}$ was calculated directly by subtracting the periodic potential from its open-boundary counterpart. The computational cost of this direct method is prohibitively high, on the order $O(N^2)$ (where N is the number of grid points), corresponding to the evaluation of Coulomb integrals at each point of the grid. In this section, we present a scheme that reduces this computational burden. The scheme exploits both the Poisson equation for v^{corr} (Eq. 3.5) and the fact that v^{corr} is smoothly varying.

First, we note that taking into account appropriate boundary conditions, Eq. 3.5 can be solved efficiently using multigrid solvers [56–61]. Multigrid algorithms typically scale as $O(N \log N)$, that is, comparable to the scaling of an FFT computation. Hence, the overall cost of the calculation can be reduced from $O(N^2)$ to $O(N^{5/3})$, corresponding to the expense arising from the determination of the boundary conditions. Although a similar approach may be employed to directly solve the electrostatic equation defining v (Eq. 3.1), we emphasize that Eq. 3.5 allows a considerable reduction in numerical error in the finite-difference evaluation of the electronic Laplacian—since v^{corr} is much smoother than v.

Further exploiting this idea, it is possible to solve Eq. 3.5 on a grid much coarser than that used to discretize the charge density. To illustrate this fact, we consider a pyridazine cation in a periodic cubic cell of varied size (Figure 3-6). The total energy of the system is calculated using density-functional theory [62]. An energy cutoff $E_{cut} = 250$ Ry is applied to

Figure 3-6: DCC total energy as a function of cell size for a pyridazine cation varying the coarse-grid cutoff E_{cut}^{corr} from 10 Ry ($M = 13 \times 13 \times 13$) to 250 Ry ($M = N = 73 \times 73 \times 73$). Also depicted is the corrective potential v^{corr} in the plane of the molecule as a function of the coarse-grid resolution at a cell size of 15 bohr.
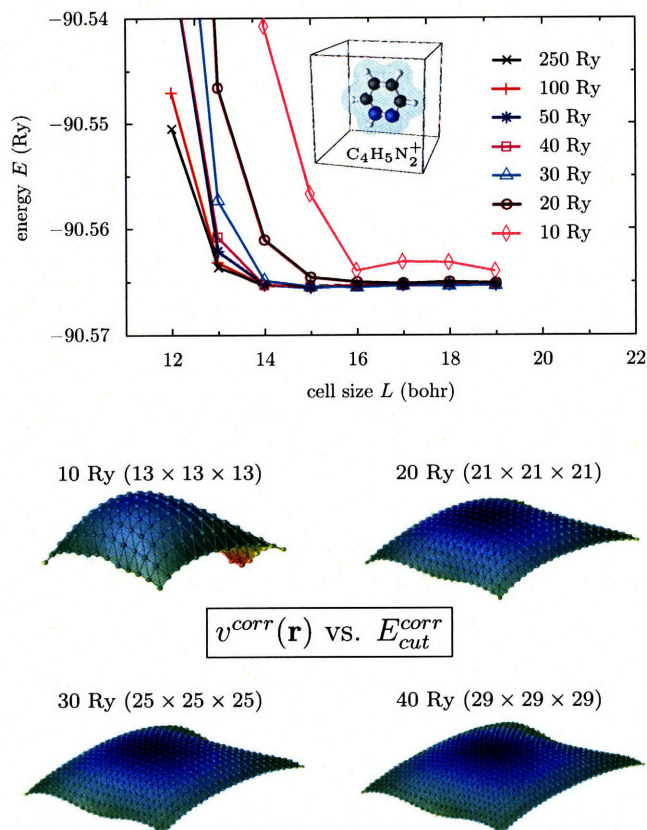
the plane-wave expansion of the charge density. The total energies are corrected using the DCC scheme by solving the electrostatic equation of v^{corr} on a coarse grid for several values of the energy cutoff, denoted E_{cut}^{corr}. Reducing the energy cutoff E_{cut}^{corr} from 250 to 40 Ry, the corrected energies are observed to depart by less than 5×10^{-3} Ry from their converged values for cell sizes greater than 13 bohr. The ability to decrease the number of grid points without a significant loss of accuracy enables a substantial reduction of the additional computational cost from $O(N^{5/3})$ to $O(M^{5/3})$, where M is the number of coarse-grid points. Note that diminishing the plane-wave energy cutoff from 250 to 40 Ry at $L = 15$ bohr reduces the cost of the boundary-condition calculation by a factor $29^5/73^5 \approx 1/100$.

Before presenting the algorithm, we draw attention to the fact that the DCC scheme relies on the central idea that most of the structural characteristics of the open-boundary potential v can be removed by subtracting out its periodic counterpart v'. The residual v^{corr} (that is, the amount by which v' fails to reproduce v) is smooth and can be determined on a coarse grid at low computational cost. Additional computational savings come from the ability to

avoid updating the potential v^{corr} at each step of the self-consistent-field (SCF) calculation, but instead at fixed interval between electronic iterations.

The DCC algorithm for a typical electronic-structure calculation can be described as follows. Let N^{corr} denote the number of SCF steps between each update of the corrective potential.

DCC Algorithm

1. Start from an initial charge distribution ρ on the fine grid.

2. Calculate the periodic potential v' corresponding to ρ.

3. Transfer ρ and v' on the coarse grid (tricubic interpolation [63]) to obtain the coarse-grid density $\tilde{\rho}$ and coarse-grid periodic potential $\tilde{v}'$.

4. Calculate the real-space potential $\tilde{v}$ at the boundaries of the coarse grid from $\tilde{\rho}$ to obtain the Dirichlet boundary conditions $\tilde{v}^{corr} = \tilde{v} - \tilde{v}'$.

5. Solve $\nabla^2 \tilde{v}^{corr} = -4\pi\langle\rho\rangle$ (multigrid techniques) to obtain the corrective potential $\tilde{v}^{corr}$.

6. Transfer $\tilde{v}^{corr}$ on the fine grid (tricubic interpolation) to obtain v^{corr}, and calculate $v = v^{corr} + v'$.

7. Perform N^{corr} electronic SCF steps.

8. Iterate from Step 2 until reaching SCF convergence.

Note that we employ real-space tricubic interpolation techniques in order to avoid oscillatory distortions inherent in Fourier-transform interpolation schemes. We also underscore that the DCC algorithm can be efficiently parallelized, since its most expensive step (namely, the calculation of the Dirichlet boundary conditions) scales linearly with the number of processors.

The above procedure can be adapted to one- and two-dimensional systems by considering the linear or planar average of the charge density for calculating the corrective potential [47]. (The validity the linear- or planar-average approximations will be discussed in the final section.) The computational cost of this approach is moderate, on the order of $O(M^{1/3})$ and $O(M)$ for one and two dimensions, respectively.

It should also be mentioned that the DCC algorithm can be used in combination with multipole-expansion methods for a rapid evaluation of the Dirichlet boundary conditions (Step

Figure 3-7: Total energy as a function of cell size for a neutral pyridazine molecule without correction and corrected using the PCC, GCC, and DCC schemes. The PCC and GCC corrections are calculated up to quadrupole order. The inset shows a pyridazine molecule in a cell of size $L = 15$ bohr.
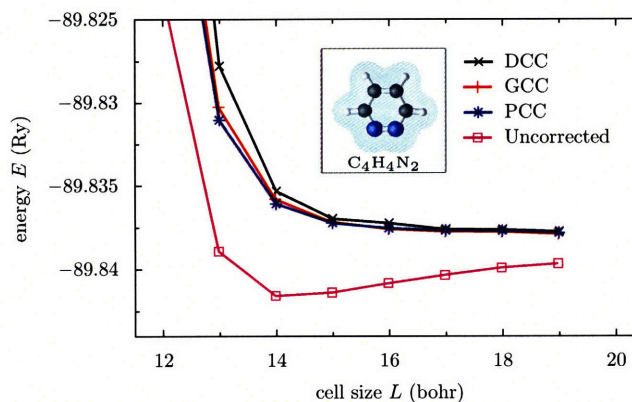
4). The accuracy of this approach depends on the precision of the multipole expansion at the boundary of the supercell. (A mathematical discussion on the long-range accuracy of multipole expansions is presented in Sec. 3.4. of Greengard's dissertation [64].) The performance the multipole-expansion approach is reported in Appendix B.

3.3.2 Applications

The energy of a pyridazine molecule as a function of cell size L for each countercharge correction is reported in Figure 3-7. For this neutral species, the uncorrected energy shows a characteristic minimum at $L = 14$ bohr before slowly approaching its asymptotic value. In contrast, the corrected energies are seen to converge monotonically towards their common energy limit. Although the three schemes demonstrate comparable convergence, it should be noted that the PCC method is slightly more accurate. In addition to further validating the energy expansion given by Eq. 3.21, this comparison suggests that the PCC correction can be preferred for studying neutral species, with the notable exception of elongated systems (*e.g.*, polymer fragments or terminated nanotubes).

We now consider the energy of a pyridazine cation as a function of cell size (Figure 3-8). We use energy cutoffs of 35 and 250 Ry for expanding the wavefunctions and the charge density, and select a coarse-grid cutoff of 35 Ry for calculating the DCC correction. Expectedly, the uncorrected energy converges very slowly with respect to L (at 19 bohr, the energy error is still larger than 0.15 Ry). The PCC and GCC corrections substantially improve the convergence of the total energy, reducing periodic-image errors by one order of magnitude. Using the DCC scheme, the energy is observed to converge even more rapidly, reflecting the exponential disappearance of energy errors arising from charge density spilling across periodic
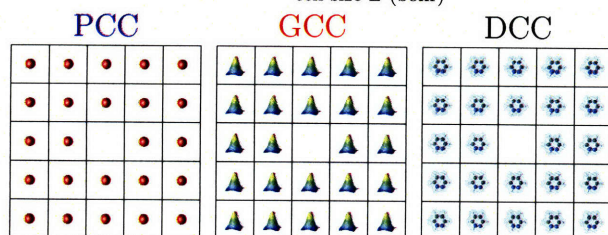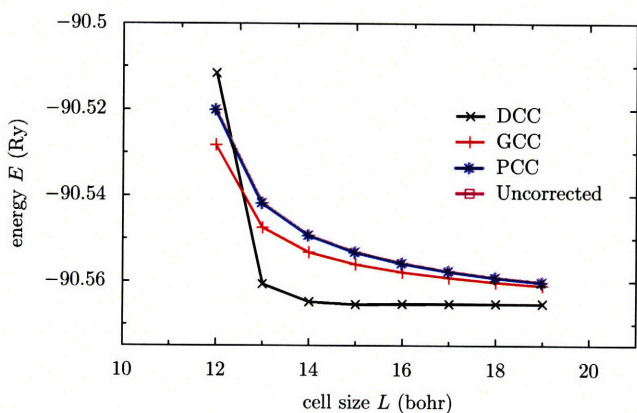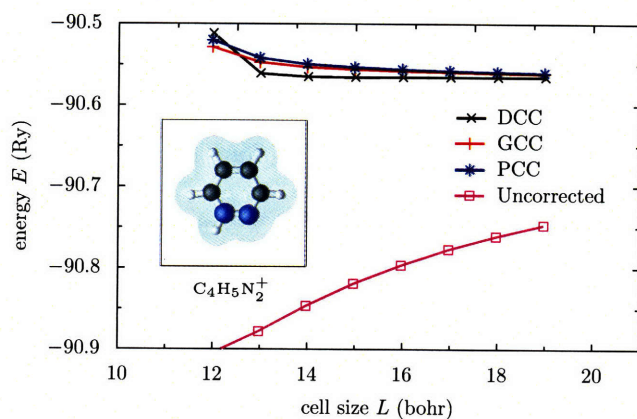
Figure 3-8: Total energy as a function of cell size for a pyridazine cation without correction and corrected using the PCC, GCC, and DCC schemes. The PCC and GCC corrections are calculated up to quadrupole order. The inset of the top graph shows a pyridazine cation in a cell of size $L = 15$ bohr.

cells: at a cell size of 15 bohr, which is barely larger than the size of the molecule, the DCC energy is converged within 10^{-4} Ry. The performance of each scheme as a function of the total computational time is shown on a logarithmic energy scale in Figure 3-9. Each curve corresponds to cell sizes in the range 12-19 bohr. For meaningful comparison with the DCC scheme, the PCC and GCC corrective potentials are also updated at fixed SCF intervals. We observe that the computational cost of the corrected calculations is comparable to that without correction for a considerable improvement in accuracy. For this charged system, the DCC approach constitutes the most advantageous alternative, improving the energy precision by two orders of magnitude over the PCC and GCC corrections for cell sizes above 15 bohr.
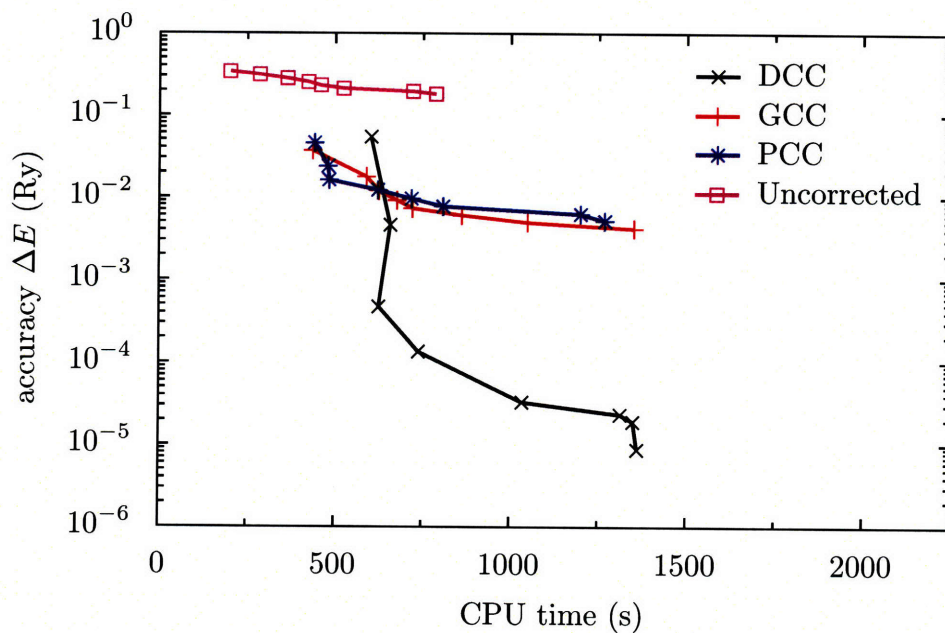
Figure 3-9: Accuracy of the total energy as a function of computational time for an isolated cation without correction and using the PCC, GCC, and DCC schemes for cell sizes in the range 12-19 bohr. For each scheme, the corrective potential is updated every five SCF iterations.

Figure 3-10: Total energy as a function of transverse cell size for a polyvinylidene fluoride (PVDF) chain without correction, and using the GCC and DCC schemes.
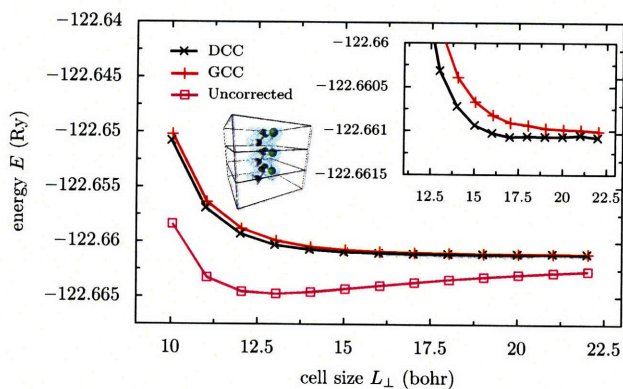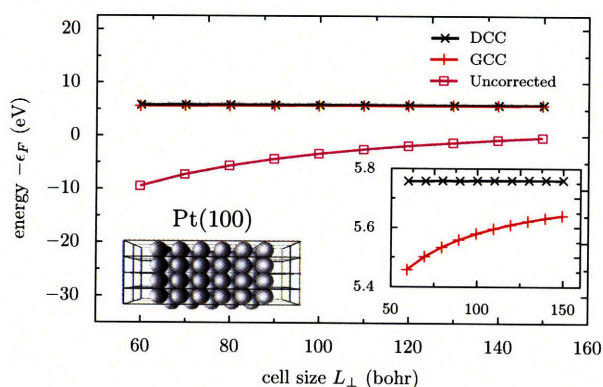
Figure 3-11: Convergence of the opposite Fermi energy $-\epsilon_F$ as a function of transverse cell size for a Pt(100) slab without correction, and using the GCC and DCC schemes.

The performance of the DCC and GCC corrective schemes for a neutral polyvinylidene fluoride (PVDF) chain is reported in Figure 3-10. The comparison shows a significant improvement of energy convergence for both schemes. As shown in the inset, the performance of the DCC scheme is perceptibly superior to that of the GCC scheme. We emphasize that for systems exhibiting one dimensional periodicity, the additional computational cost due to the electrostatic correction is moderate, on the order of $O(M)$ at most.

The DCC scheme can also be used in the calculation of work functions, as it solves energy-reference issues by automatically setting the vacuum level to zero. Figure 3-11 depicts the convergence of the opposite Fermi energy of a Pt(100) slab as a function of transverse cell size. The wavefunction, charge-density, and corrective potential energy cutoffs are 25, 200, and 150 Ry, respectively. We use a shifted $5 \times 5 \times 1$ mesh with a cold-smearing occupation function [12] (smearing temperature of 0.03 Ry) to sample the Brillouin zone. Without correction, the relative error in the Fermi energy stays above 100% for all cell sizes in the considered range. Using the GCC scheme, the convergence of the Fermi level improves greatly: at 150 bohr, the relative error reduces to approximately 0.1 eV. Employing the DCC corrective scheme, the calculated Fermi energy is converged within 2 meV at 60 bohr and 0.1 meV at 150 bohr. Thus, the DCC scheme allows to directly determine the work function of a metal as the opposite of the calculated Fermi energy using supercells of minimal size. A similar convergence improvement is obtained for the work function of carbon nanotubes [65]. Besides improving the convergence of total energies, the DCC approach can be employed to correct structural and vibrational properties [66], and to calculate linear-response characteristics with a reduced computational effort [66–68].

3.4 Beyond the Linear- and Planar-average Approximations

3.4.1 Treating systems with partial periodicity

In the preceding sections, we have assumed that the corrective potential of a one- or two-dimensional system can be obtained by homogenizing the system along its periodicity directions, as initially proposed by Baldereschi, Baroni, and Resta [47]. This approach, referred to as the linear- or planar-average approximation, has been frequently employed in electronic-structure calculations [46–48, 51, 69].

Alternative schemes adapting the Ewald method to evaluate conditionally convergent lattice sums [70] or generalizing the FMM approach [71, 72] have also been proposed for systems exhibiting partial periodicity. Such schemes are particularly suited to localized-orbital calculations but are of relatively limited applicability for plane-wave implementations. Here, we propose an efficient method to calculate the electrostatic potential for partially periodic systems, taking into account the full three-dimensional structure of the charge distribution. In addition to presenting this methodological extension, we discuss how to assess the validity of the linear- and planar-average approximations *a priori* in terms of structural characteristics of the system.

3.4.2 DCC Scheme for One-dimensional Periodicity

To introduce the DCC approach for one-dimensional systems, we first study the electrostatic problem corresponding to an isolated sinusoidal-density line:

$$\rho(\mathbf{r}) = \delta^{(2)}(\mathbf{r}_\perp) \exp(ig_z z), \tag{3.22}$$

where $\delta^{(2)}$ stands for the two-dimensional Dirac delta function and $\mathbf{r}_\perp$ denotes the transverse coordinates (x, y). Making the ansatz $v(\mathbf{r}) = \mathcal{G}(\mathbf{r}_\perp; g_z) \exp(ig_z z)$ for the Green's function, we obtain:

$$(\nabla_\perp^2 - g_z^2)\mathcal{G}(\mathbf{r}_\perp; g_z) = -4\pi\delta^{(2)}(\mathbf{r}_\perp). \tag{3.23}$$
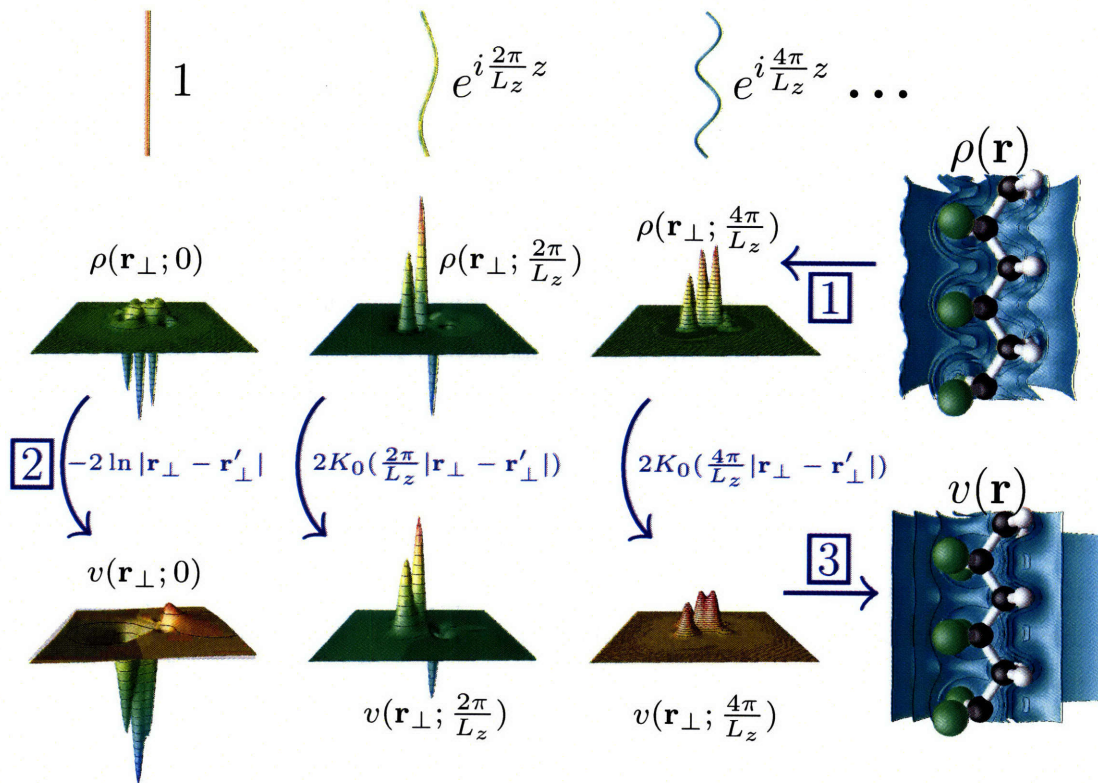
Figure 3-12: Fourier-decomposition calculation of the electrostatic potential $v(\mathbf{r}_\perp, z) = \sum_{g_z} v(\mathbf{r}_\perp; g_z)e^{ig_z z}$ for an infinite polyvinylidene fluoride (PVDF) chain. (1) The longitudinal Fourier transform of the charge density is calculated to obtain the contributions from each axial wavevector g_z; (2) the electrostatic potential generated by each Fourier component of the charge density is calculated using Green's functions; (3) the electrostatic potential is then transformed back to real space.

The solution of this generalized electrostatic problem can be written as:

$$\begin{cases} \mathcal{G}(\mathbf{r}_\perp; 0) &= -2\ln|\mathbf{r}_\perp|, \\ \mathcal{G}(\mathbf{r}_\perp; g_z) &= 2K_0(g_z|\mathbf{r}_\perp|) \quad \text{for } g_z \neq 0 \end{cases} \tag{3.24}$$

where K_0 is the modified Bessel function of the second kind. Note that $K_0(g_z|\mathbf{r}_\perp|) = -\ln|\mathbf{r}_\perp| + \dots$ when $g_z|\mathbf{r}_\perp|$ approaches zero, reflecting the fact that a sinusoidal-density line can be considered as uniform when seen from a distance much smaller than its wavelength. Knowing the electrostatic potential generated by a single line (the Green's function characterizing the generalized electrostatic problem), the potential of an arbitrary one-dimensional charge distribution can be determined analytically, as illustrated in Figure 3-12. The general procedure consists of calculating the one-dimensional Fourier transform of ρ to obtain its longitudinal Fourier components $\rho(\mathbf{r}_\perp; g_z)$ (step 1). Each individual components is then convoluted with the electrostatic potential generated by a sinusoidal density, as expressed in Eq. (3.24) to obtain the Fourier components $v(\mathbf{r}_\perp; g_z)$ of the open-boundary potential (step 2):

$$\begin{cases} v(\mathbf{r}_\perp; 0) &= -2\displaystyle\int \ln|\mathbf{r}_\perp - \mathbf{r}'_\perp|\rho(\mathbf{r}'_\perp; 0)d\mathbf{r}'_\perp, \\ v(\mathbf{r}_\perp; g_z) &= 2\displaystyle\int K_0(g_z|\mathbf{r}_\perp - \mathbf{r}'_\perp|)\rho(\mathbf{r}'_\perp; g_z)d\mathbf{r}'_\perp \quad \text{for } g_z \neq 0. \end{cases} \tag{3.25}$$

Finally, the open-boundary potential is transformed back to real space (step 3). We underscore that this procedure directly extends the linear-average approximation since the linear average of the charge density corresponds to the first term of the one-dimensional Fourier decomposition. Thus, averaging the charge density along the axis of periodicity amounts to restricting the Fourier series to its $g_z = 0$ term.

To estimate errors resulting from this truncation, we analyze the asymptotic behavior of $v(\mathbf{r}_\perp; g_z \neq 0)$ at large $g_z|\mathbf{r}_\perp|$:

$$v(\mathbf{r}_\perp; g_z) \approx \sqrt{\frac{\pi}{2}} \frac{e^{-g_z|\mathbf{r}_\perp|}}{\sqrt{g_z|\mathbf{r}_\perp|}} \quad \text{when } g_z|\mathbf{r}_\perp| \gg 1. \tag{3.26}$$

From Eq. 3.26, the validity of the linear average approach can be assessed by calculating the ratio of the cell size in the transverse direction $L_\perp$ (that is, the distance between periodic replicas) to the typical wavelength $\lambda_\parallel$ characterizing longitudinal inhomogeneities in the system. For large values of the dimensionless parameter $L_\perp/\lambda_\parallel$, periodic-image interactions are predominantly due to the logarithmic first-order contribution $v(\mathbf{r}_\perp; 0)$ corresponding to

the linear average of the charge density. Thus, as expected intuitively, the linear-average approximation is valid in this situation. In contrast, when $\lambda_{\parallel}$ is comparable to the distance $L_{\perp}$ between periodic images, higher-order Fourier components $v(\mathbf{r}_{\perp}; g_z)$ corresponding to $g_z \approx 2\pi/\lambda_{\parallel}$ must also be taken into consideration.

Despite its merit in discussing the validity of the linear-average approximation, determining the open-boundary potential using the preceding approach requires expensive summations for each point $\mathbf{r}_{\perp}$ of the two-dimensional grid and for each longitudinal wavevector g_z. Along the same methodological lines as those of the DCC algorithm, a substantial reduction of computational cost can be achieved by exploiting the periodic potential v', whose longitudinal Fourier components can be computed inexpensively using FFT techniques:

$$
\begin{cases}
v'(\mathbf{r}_{\perp}; 0) & = \displaystyle\sum_{\mathbf{g}_{\perp} \neq 0} \frac{4\pi}{\mathbf{g}_{\perp}^2} \rho(\mathbf{g}_{\perp}) e^{i\mathbf{g}_{\perp} \cdot \mathbf{r}_{\perp}}, \\[2ex]
v'(\mathbf{r}_{\perp}; g_z) & = \displaystyle\sum_{\mathbf{g}_{\perp}} \frac{4\pi}{\mathbf{g}_{\perp}^2 + g_z^2} \rho(\mathbf{g}_{\perp} + g_z \hat{\mathbf{z}}) e^{i\mathbf{g}_{\perp} \cdot \mathbf{r}_{\perp}} \quad \text{for } g_z \neq 0.
\end{cases}
\tag{3.27}
$$

After coarse-grid interpolation, the component of the open-boundary potential $v(\mathbf{r}_{\perp}; g_z)$ can be calculated at the boundaries of the domain, yielding Dirichlet boundary conditions for the smooth corrective components $v^{corr}(\mathbf{r}_{\perp}; g_z) = v'(\mathbf{r}_{\perp}; g_z) - v'(\mathbf{r}_{\perp}; g_z)$. The corresponding g_z-dependent electrostatic problems read:

$$
\begin{cases}
\nabla^2 v^{corr}(\mathbf{r}_{\perp}; 0) & = -4\pi\langle\rho\rangle \\[1ex]
(\nabla^2 - g_z^2) v^{corr}(\mathbf{r}_{\perp}; g_z) & = \quad 0 \quad\quad \text{for } g_z \neq 0
\end{cases}
\tag{3.28}
$$

These differential equations can be solved using efficient multigrid techniques. Once calculated, the longitudinal Fourier components of the electrostatic correction are added to those of the periodic potential, thereby recovering $v(\mathbf{r}_{\perp}; g_z)$. Finally, the potential $v(\mathbf{r})$ is computed via an inverse Fourier transform.

3.4.3   DCC Scheme for Two-dimensional Periodicity

The electrostatic potential of a slab can be calculated in real space using a scheme similar to that presented above. The formalism is to a great extent analogous to that developed by Lang and Kohn for studying interactions between localized external charges and metallic surfaces [73], and to the Green's function approach recently proposed by Otani and Sugino [74]. The prescription consists of performing two-dimensional Fourier transforms to obtain the

Figure 3-13: Total energy as a function of transverse cell size for a $-[CH_2CF_2]_3-[CF_2CH_2]_3-$ polymer chain without correction, corrected using the density-countercharge scheme with full Fourier decomposition (DCC), and by limiting the density-countercharge decomposition to the linear-average $g = 0$ component (DCC/LA).
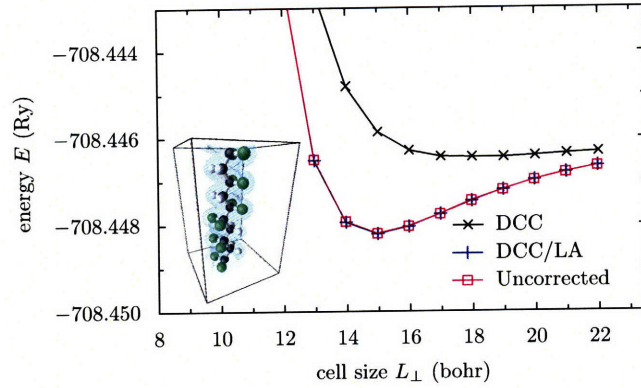
charge-density profile $\rho(z; g_{\parallel})$ associated with each wavevector $g_{\parallel} = (g_x, g_y)$ parallel to the surface. Solving the electrostatic problem for sinusoidal density layers, the two-dimensional Green's functions $\mathcal{G}(z; g_{\parallel})$ can be written as:

$$\begin{cases} \mathcal{G}(z; \mathbf{0}) &= -2\pi |z|, \\ \mathcal{G}(z; \mathbf{g}_{\parallel}) &= 2\pi \dfrac{e^{-g_{\parallel}|z|}}{g_{\parallel}} \quad \text{for } g_{\parallel} \neq 0. \end{cases} \tag{3.29}$$

Hence, as in the one-dimensional case, the density-average approximation is valid provided that the geometrical parameter $L_{\perp}/\lambda_{\parallel}$ is large—this criterion is identical to that derived by Natan, Kronik, and Shapira [49]. In addition, the above expressions allow one to determine the corrective potential of a two-dimensional system by integrating the differential equations:

$$\begin{cases} \frac{d^2}{dz^2} v^{corr}(z; \mathbf{0}) &= -4\pi \langle \rho \rangle \\ (\frac{d^2}{dz^2} - g_{\parallel}^2) v^{corr}(z; \mathbf{g}_{\parallel}) &= 0 \quad \text{for } g_{\parallel} \neq 0 \end{cases} \tag{3.30}$$

Parenthetically, it is important to note that Eq. 3.30 can be solved analytically, taking into account the boundary conditions calculated by superposition—that is, by convoluting the longitudinal components of $\mathcal{G}$ and ρ (similarly to Eq. 3.25), then subtracting out the components of v'. Therefore, the additional cost of the two-dimensional DCC correction is negligible.

3.4.4 Applications

The convergence of the total energy with respect to transverse cell size for a fluoropolymer chain $-[CH_2CF_2]_3 - [CF_2CH_2]_3-$ of long periodicity $\lambda_{\parallel} \approx 24$ bohr is depicted in Figure 3-
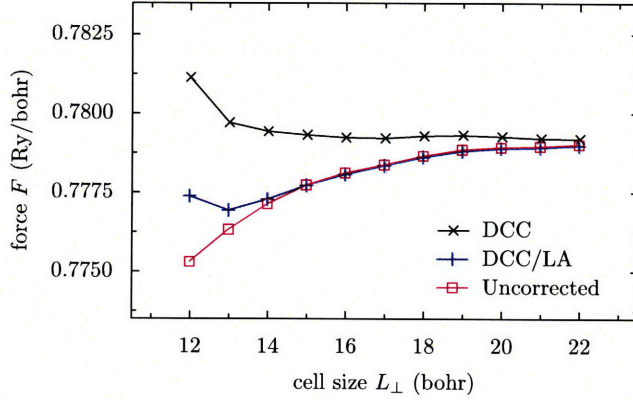
Figure 3-14: Force on one of the fluorine atoms along a transverse lattice direction as a function of transverse cell size for a $-[CH_2CF_2]_3-[CF_2CH_2]_3-$ polymer chain without correction, corrected using the density-countercharge scheme with full Fourier decomposing (DCC), and by limiting the density-countercharge decomposition to the linear-average $g = 0$ component (DCC/LA).

13. We employ ultrasoft pseudopotentials [21] with energy cutoffs of 50 and 500 Ry for the plane-wave expansions of the electronic wavefunctions and charge density, respectively. The energy cutoff for calculating the corrective potential is 80 Ry. We use a shifted $1 \times 1 \times 2$ mesh with cold-smearing occupations [12] (smearing temperature of 0.02 Ry). Within the linear average approximation (DCC/LA), the corrected energy closely coincides with the uncorrected energy due to the absence of polarization in the longitudinal average of the charge density. For the cell parameters considered, the geometrical ratio $L_\perp/\lambda_\parallel$ varies from 0.5 to 0.9, that is, beyond the range of validity of the linear average approximation. As a result, we observe that the DCC/LA energy converges slowly towards its asymptotic value. In contrast, the DCC scheme with full Fourier decomposition significantly improves the convergence of the total energy (at 16 bohr, the accuracy of DCC energy is approximately 5×10^{-5} Ry whereas that of the uncorrected and DCC/LA energies is approximately 10^{-3} Ry). Figure 3-14 depicts the convergence of the force on one of the fluorine atoms. Similarly to the convergence of the total energy, the atomic-force convergence is seen to improve substantially by applying the DCC correction: at 16 bohr, the DCC force is converged within less than 10^{-4} Ry/bohr, while that obtained without correction or using the DCC/LA scheme are converged within 10^{-3} Ry/bohr. We underscore that the additional computational cost of the DCC correction is moderate. Indeed, at 16 bohr, the additional computational cost is $\sim 8\%$.

To conclude this study, we consider the electronic density response of a graphene sheet subject to a perturbation field. Figure 3-15 reports the dependence of the linear-response coefficient $\chi(g_\parallel) = \partial n(g_\parallel)/\partial v(g_\parallel)$ with respect to the interplane distance $L_\perp$ for a longitudinal sinusoidal perturbation of wavevector $g_\parallel = \frac{1}{25}$ bohr^{-1}. The wavelength of the perturbation field being large ($\lambda_\parallel = 157$ bohr), the uncorrected response coefficient does not convergence

Figure 3-15: Longitudinal density response coefficient $\chi(g_\parallel) = \partial n(g_\parallel)/\partial v(g_\parallel)$ as a function of transverse cell size for a graphene sheet without correction, and corrected using the density-countercharge scheme with full Fourier decomposition (DCC).
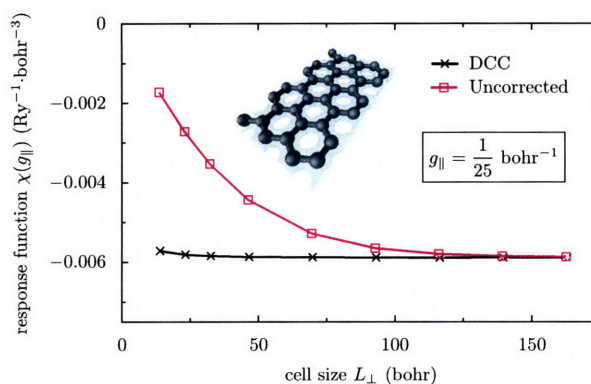
until reaching cell sizes on the order of hundreds of bohrs. Contrary to uncorrected calculations, the DCC-corrected linear response shows considerable convergence improvement with a negligible increase in computation cost. For comparison, at an interplane distance of $L_\perp = 50$ bohr, the relative error in the uncorrected linear-response coefficient $\chi(g_\parallel)$ is on the order of 25%, while it is lower than 1% using the DCC correction.

3.5   Conclusion

We have studied the analytical properties of the corrective potential, defined as the difference between the electrostatic potential and its periodic counterpart, unifying the Makov-Payne (PCC) and LMCC (GCC) schemes in the same class of periodic-image corrections and suggesting possible improvements for both methods. Based on these properties, we have shown that the periodic-image errors can be eliminated at a moderate computational cost of $O(M^{5/3})$, where M is the number of points of the mesh used in the calculation the corrective potential, which is generally about two orders of magnitude smaller than the number of points of the charge-density grid. The resulting density-countercharge (DCC) scheme owes its improved efficiency to the determination of the exact boundary conditions characterizing the electrostatic potential. In several cases of interest, we have shown that the DCC algorithm represents a beneficial compromise between cost and accuracy. The validity of the linear- and planar-average approximations routinely employed in the study of partially periodic systems has also been discussed. An efficient scheme going beyond these conventional approximations for inhomogeneous systems has been proposed and validated.

Relevant applications for the DCC algorithm include the study of molecular adsorption at solid-vacuum interfaces in the constant-charge regime, the determination of structural

parameters, the correction of vibrational spectra, the inexpensive calculation of work functions, and the determination of linear-response properties with a reduced computational effort.

Electrified Metal Surfaces in Ionic Media

4.1 Introduction

THE ELECTRICAL RESPONSE OF ELECTROCHEMICAL CONVERTORS, such as fuel cells, batteries, or electrochemical capacitors, is to a large extent governed by polarization and charge-separation phenomena taking place at the interfaces separating the electrodes from the electrolyte termed electrical double layers [75]. Therefore, predicting the electrical characteristic of an electrochemical system primarily involves elucidating the voltage dependence of the charge distribution inside the double-layer interface [76].

Despite recent advances in the description of electrochemical interfaces from first principles [51,74,77,78], determining the potential dependence of the interfacial charge still represents a challenging problem characterized by length scales that are orders of magnitude greater than the typical sizes accessible to conventional density-functional theory simulations. As a matter of comparison, the polarized charge distribution across the electrode-electrolyte interface can extend as far as thousands of nanometers in dilute electrolyte solutions [79], while the size of typical density-functional theory calculation domains do not exceed tens of nanometers. This inherent restriction precludes a direct first-principles description of important phenomena, such as the dependence of the electrode catalytic activity as a function of the applied electrical potential [77] or the potential dependence of adsorbate vibrational properties—the vibrational Stark effect—on electrode surfaces [80].

In order to surmount these important limitations, we propose a modified Poisson-Boltzmann model that builds on the solvation scheme introduced by Fattebert and Gygi [58], and extends the approach recently proposed by Otani and Sugino [74]. The main interest of this model is

its ability to predict the electrical response of an electrochemical interface embedded in an effectively semi-infinite ionic medium, provided that adequate boundary conditions are imposed at the frontier of the simulation cell. Another notable advantage of this approach lies in the fact that it directly extends standard diffuse-layer models [75,79] by allowing a first-principles description of the metal region, thereby offering a direct comparison with well-established theories.

We first introduce the conventional theoretical framework for studying metal-solution interfaces. Second, we provide a comparative overview of recently proposed first-principles models for studying electrified surfaces. Third, we describe the solvation algorithm, showing that the solvent reaction field can be calculated independently at low computational cost. In the fourth section, we present the diffuse-layer method and draw attention to the particular importance of boundary conditions in calculating the differential capacitance of electrochemical interfaces.

4.2   Theory of Electrochemical Interfaces

4.2.1   Electrical Potential of Metal Electrodes

The electrode potential is a measure of the energy required to displace an electron from the bulk of the metal electrode to the bulk of the ionic solvent. Explicitly, we can define the potential of an electrode $\mathcal{E}$ as [75]:

$$\mathcal{E} = W - \epsilon_C = V_S - V_M - \epsilon_C, \tag{4.1}$$

where $W = V_S - V_M$ denotes the electrostatic work done in moving an electron from the metal to the solvent, and ϵ_C stands for the chemical energy of an electron in the metal. The chemical energy ϵ_C equals the sum of all the non-electrostatic contributions to the energy of an electron in the metal [75]. In the context of density-functional theory, these contributions can be directly identified as the kinetic and exchange-correlation energies of the highest occupied metal electronic states. As a consequence, the chemical energy corresponds to the difference between the Fermi energy ϵ_F and the electrostatic potential of the electron in the metal:

$$\epsilon_C = \epsilon_F - V_M. \tag{4.2}$$

(a) Explicit solvent model
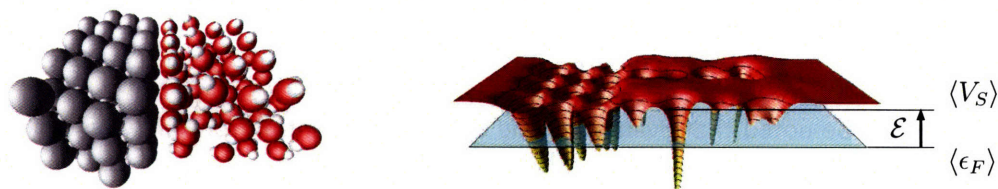
(b) Implicit solvent model
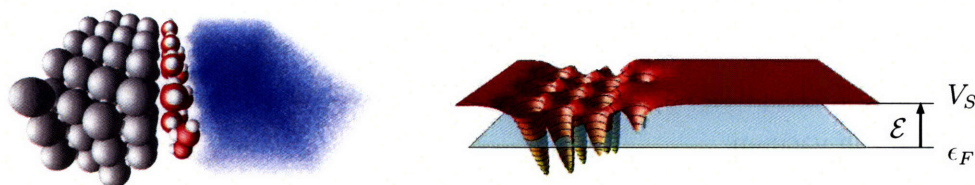
Figure 4-1: Determination of the absolute electrode potential $\mathcal{E}$ using (a) an explicit solvent model, and (b) an implicit solvent models. Within the explicit model, the potential $\mathcal{E}$ is calculated from the dynamical averages of the solvent electrostatic energy $\langle V_S \rangle$ and of the metal Fermi energy $\langle \epsilon_F \rangle$.

Substituting Eq. 4.2 into Eq. 4.1, we can express the electrode potential as the difference between the electrostatic energy of an electron in the bulk of the solvent and the Fermi energy of the metal, as expected intuitively:

$$\mathcal{E} = V_S - \epsilon_F. \tag{4.3}$$

While the preceding expression defines the absolute potential of an electrode, experimental measurements of the electrode potential are generally referenced to the potential of a noble-metal electrode under electrochemical equilibrium with a solvent in standard conditions of temperature, partial pressure, and ionic activity. The referenced electrode potential $\mathcal{E}'$ is related to the absolute electrode potential $\mathcal{E}$ through:

$$\mathcal{E}' = \mathcal{E} - \mathcal{E}^\circ. \tag{4.4}$$

One of the most widely used reference electrode is the standard hydrogen electrode (SHE), which typically consists of a platinum surface in contact with an aqueous solution containing H^+. The accurate determination of the absolute SHE potential is still the subject of active

research. Current estimations of the absolute SHE potential $\mathcal{E}^\circ(H_2/H^+)$ lie in a relatively large energy range [75]:

$$4.44 \text{ eV} < \mathcal{E}^\circ(H_2/H^+) < 4.78 \text{ eV}. \tag{4.5}$$

It should be noted that evaluating the electrode potential from first-principles simulations requires determining the value of the effective electrostatic energy of an electron in the solvent V_S. The definition of V_S in the context of explicit solvent models is not straightforward [78]. In contrast, implicit solvent models allow a direct determination of V_S as the asymptotic value of the electrostatic potential in the bulk of the ionic continuum (Figure 4-1).

It should be emphasized that Eq. 4.3 is similar to the definition of the work function Φ for surfaces in vacuum:

$$\Phi = V_0 - \epsilon_F, \tag{4.6}$$

where V_0 is the vacuum electrostatic energy measured at a large distance from the surface. Note that the electrode work function is only determined for neutral interface as a result of the linear divergence of the electrostatic potential outside charged surfaces. In contrast, the electrostatic potential of a charged electrode in contact with an ionic solution does not diverge due to ionic screening inside the electrolyte. Hence, even in the case of charged interfaces, the electrode potential $\mathcal{E}$ is defined.

From Eq. 4.3 and Eq. 4.6, the potential of a neutral electrode—the potential of zero charge $\mathcal{E}_{pzc}$—is related to the electrode work function through:

$$\mathcal{E}_{pzc} = \Phi - \chi_S. \tag{4.7}$$

where $\chi_S = V_S - V_0$ is commonly referred to as the dipole potential (or surface potential) of the solvent. The energy χ_S corresponds to the supplementary electrostatic work for taking a metal electron across the polarized solvent layer. Experimental correlations between the potential of zero charge and the electrode potential for various single-crystal electrodes indicate that the solvent dipole potential χ_S is moderately affected by surface orientation but depends mainly on the electronic nature of electrode material (i.e., on whether the electrode is made of a s-, p-, or d-metal) [3, 79].

4.2.2　Capacitance of Metal Electrodes

The capacitance of an electrode-electrolyte interface relates the local state of charge of the electrode surface to the applied external potential. The specific differential capacitance of a
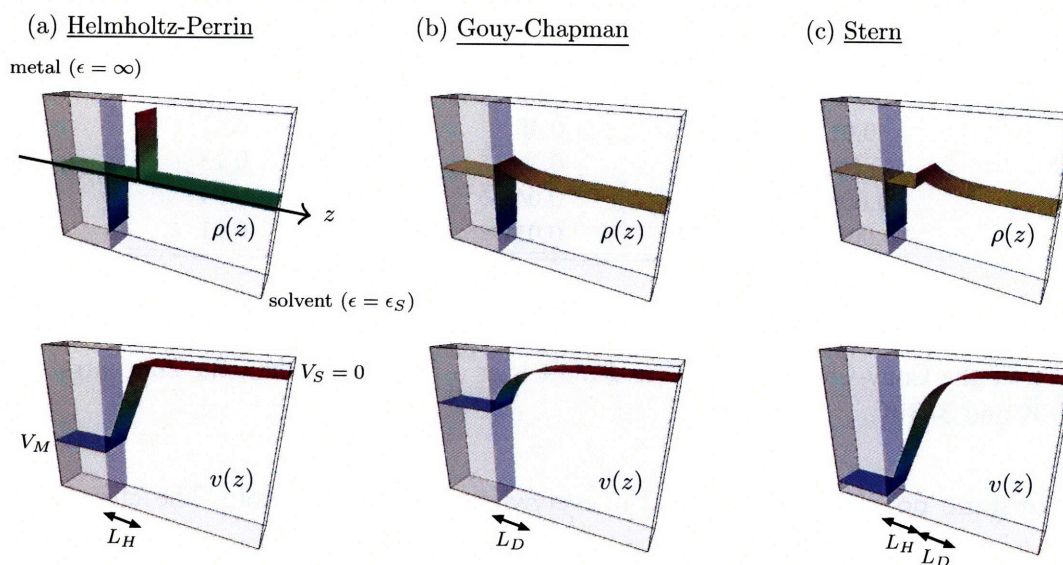
Figure 4-2: Charge-density and electrostatic-potential profiles for the Helmholtz-Perrin, Gouy-Chapman, and Stern double-layer models.

double-layer interface C is defined as:

$$C = \frac{d\sigma}{d\mathcal{E}}, \tag{4.8}$$

where σ is the surface charge, and $\mathcal{E}$ is the electrode potential.

Experimental measurements of electrode capacitances indicate that the electrical response of electrode-electrolyte interfaces is strongly nonlinear. In particular, at low ionic concentrations, the differential capacitance typically shows a sharp minimum at the potential of zero charge. This steep decrease can be explained by considering the electrical response of the ionic solvent. Three standard theories for describing the ionic contribution to the electrode capacitance—namely, the Helmholtz-Perrin, the Gouy-Chapman, and the Gouy-Stern double-layer theories—are presented in next the section.

4.2.3 Standard Double-layer Models

In the conventional double-layer models described below, the metal electrode is represented by a polarizable continuum of infinite dielectric constant $\epsilon_M = +\infty$. Consequently, the

c_d ($z_d = 1$)	$T = 300$ K		$T = 373$ K	
	L_D (Å)	$C_{d,pzc}$ (F/m^2)	L_D (Å)	$C_{d,pzc}$ (F/m^2)
0.1 M	9	1.43	11	1.28
0.01 M	30	0.45	34	0.41
0.001 M	96	0.14	107	0.13
0.0001 M	305	0.04	340	0.04
0.00001 M	964	0.01	1074	0.01

Table 4.1: Debye length L_D and diffuse-layer capacitance at the potential of zero charge $C_{d,pzc}$ of the Gouy-Chapman and Stern models as a function of the ionic concentration c_d at 300 K and 373 K.

electrostatic potential is equal to V_M everywhere inside the metal. The chemical energy contribution ϵ_C is neglected. The ionic solution is modeled by a countercharge distribution immersed in a uniform solvent medium of dielectric constant ϵ_S.

The Helmholtz-Perrin model is presented in Figure 4-2a. It consists of representing the ionic countercharges by a thin charged layer—the outer Helmholtz plane—located at a distance L_H from the surface. The intermediate solvent region that separates the metal layer from the outer Helmholtz plane is referred to as the Helmholtz layer. Taking the origin of the transverse z-axis to be at the position of the metal-solvent interface and selecting the energy reference to be the electrostatic energy in the bulk of the solvent ($V_S = 0$), the potential profile $v(z)$ across the double layer can be written as:

$$\begin{cases} v(z) = -V_M = 4\pi\sigma L_H/\epsilon_S & \text{if } z \leq 0 \\ v(z) = 4\pi\sigma(L_H - z)/\epsilon_S & \text{if } 0 \leq z \leq L_H \\ v(z) = 0 & \text{if } L_H \leq z. \end{cases} \tag{4.9}$$

Thus, in the absence of chemical-energy contribution, the absolute electrode potential can be expressed in terms of the surface charge as:

$$\mathcal{E} = \frac{4\pi\sigma}{\epsilon_S} L_H. \tag{4.10}$$

As a result, the differential capacitance of the Helmholtz-Perrin model equals:

$$C_H = \frac{\epsilon_S}{4\pi L_H}. \tag{4.11}$$

The main limitation of the Helmholtz-Perrin model is that it predicts a linear dependence of the

surface charge as a function of the applied voltage, contradicting experimental observations.

In order to correct this crucial discrepancy, the Gouy-Chapman model (Figure 4-2b) con-
sists of representing the countercharge profile as a diffuse Boltzmann distribution of ions in
thermal equilibrium with its electrostatic surrounding. Explicitly, the diffuse ionic distribution
ρ_d can be expressed in terms of the electrostatic potential v as:

$$\rho_d = z_d c_d \left(e^{-z_d v/k_B T} - e^{z_d v/k_B T}\right),$$ (4.12)

where c_d is the concentration of the ionic solution, z_d is the ionic valence (the anion and
cation valences are supposed to be equal), k_B is the Boltzmann constant, and T is the solvent
temperature. As a consequence, the potential in the ionic solution satisfies the electrostatic
equation:

$$\frac{d^2 v}{dz^2}(z) = \frac{8\pi}{\epsilon_S} z_d c_d \sinh \frac{z_d v(z)}{k_B T}.$$ (4.13)

Integrating Eq. 4.13 with vanishing-electric-field boundary conditions ($dv/dz \to 0$ as $z \to$
$+\infty$) and using standard trigonometric relations, we obtain:

$$\frac{dv}{dz}(z) = -\left(\frac{32\pi c_d k_B T}{\epsilon_S}\right)^{\frac{1}{2}} \sinh \frac{z_d v(z)}{2k_B T}.$$ (4.14)

(Note that the potential and its derivative are of opposite sign, in agreement with the fact
that the ionic solution shields the electric field.) By determining the magnitude of the electric
field at the electrode-electrolyte interface ($z = 0$) in function of the surface charge (Gauss'
law), we can rewrite Eq. 4.14 as:

$$\sigma = -\left(\frac{2\epsilon_S c_d k_B T}{\pi}\right)^{\frac{1}{2}} \sinh \frac{z_d V_M}{2k_B T}.$$ (4.15)

As a result, the differential capacitance of the diffuse-layer model can be expressed as:

$$\begin{cases} C_D = C_{D,pzc} \cosh(z_d \mathcal{E}/2k_B T) \\ C_{D,pzc} = \left(\frac{\epsilon_S c_d z_d^2}{2\pi k_B T}\right)^{\frac{1}{2}} \end{cases}$$ (4.16)

where $C_{D,pzc}$ is the value of the diffuse layer capacitance at zero charge. Alternatively, the
capacitance at the point of zero charge can be written as $C_{D,pzc} = \epsilon_S/4\pi L_D$, where the

Debye length L_D is the characteristic screening length in the double layer:

$$L_D = \left(\frac{\epsilon_S k_B T}{8\pi c_d z_d^2} \right)^{\frac{1}{2}}.$$ (4.17)

It should be noted that the Debye length also appears in the low-potential—or long-range—linearization of Eq. 4.14:

$$\frac{dv}{dz}(z) \approx -\frac{v(z)}{L_D} \text{ when } \mathcal{E} \to 0 \text{ (or } z \to +\infty).$$ (4.18)

In this regime, the electrostatic potential vanishes exponentially across the diffuse ionic layer with a characteristic decay length equal to L_D.

Typical values of the Debye length and of the double-layer capacitance at the potential of zero charge obtained from the Gouy-Chapman model for a monovalent ionic solution are reported in Table 4.1. At ambient temperature, the Debye length equals 9 Å, 96 Å, and 964 Å for solution concentrations of 0.1 M, 0.001 M, and 10^{-5} M, respectively: diluting the ionic concentration by a factor of one hundred decreases the differential capacitance by one order of magnitude. We emphasize, once more, that the large values of the screening length L_D preclude a direct treatment of the ionic solvent in density-functional theory simulations. The computational method presented in Sec.4.5 overcomes this essential limitation.

The Gouy-Chapman model predicts a nonlinear dependence of the surface charge as a function of the electrode potential. The double-layer capacitance reaches a characteristic minimum at zero charge, thus reproducing experimental trends. Nevertheless, the Gouy-Chapman differential capacitance is largely overestimated when the electrode potential deviates from the potential of zero charge. The Stern double-layer model—also referred to as the modified Gouy-Chapman theory—(Figure 4-2c) improves on the Gouy-Chapman description by inserting an Helmholtz layer of thickness L_H between the metal and the diffuse layer, thereby excluding ions from the direct proximity of the metal surface. Hence, the Stern double layer can be identified as consisting of an Helmholtz solvent layer placed in series with a Gouy-Chapman diffuse layer. From this analogy, the Stern capacitance $C_{H,D}$ can be expressed as:

$$\frac{1}{C_{H,D}} = \frac{1}{C_H} + \frac{1}{C_D}.$$ (4.19)

As a result, the dependence of the Stern capacitance as a function of the electrode potential

can be written as:

$$C_{H,D} = \frac{\epsilon_S}{4\pi} \left(L_H + \frac{L_D}{\cosh(z_d \mathcal{E}/2k_B T)} \right)^{-1}. \tag{4.20}$$

Note that the capacitance $C_{H,D}$ reaches a minimum at the potential of zero charge, similarly to the Gouy-Chapman model. For large deviations from the potential of zero charge, the capacitance of the Stern double layer equals that of the Helmholtz layer C_H, reflecting the rapid decay of the electric field in the ionic layer at high electrode voltages.

As a final note, it is worth mentioning that contrary to the idealized picture proposed by Stern, the capacitance contribution from the metal and from the Helmholtz layer is not negligible. In order to take into account the electrode-potential dependence of $C_{M,H}$, a microscopic description of the metal surface covered by solvent overlayers in the presence of adsorbed and solvated ions is necessary. Therefore, the first-principles description of solvated metal surfaces represents a fundamental complement to the theoretical understanding of electrode-electrolyte interfaces.

4.3   Review of First-principles Studies

Recently, several schemes have been proposed to model electrochemical interfaces subject to an applied voltage. Studying oxygen reduction on transition-metal surfaces, Nørskov et al. proposed to model the influence of the electrode potential by shifting the energies of all the electronic states of metal character by a constant amount $\Delta \mathcal{E} = \mathcal{E} - \mathcal{E}_{pzc}$ [77]. As pointed out by Nørskov et al., this approach neglects the interaction of the surface electric field with the molecular adsorbates. This interaction can significant affect the value of the adsorption energy, especially when the induced surface polarization is strong [77]. In the same study, Nørskov et al. underscore that developing a detailed first-principles model for electrical double layers constitutes one the principal challenges for achieving a realistic description of molecular adsorption on electrified surfaces.

The double-reference model proposed by Taylor, Wasileski, Filhol, and Neurock consists of calculating the electrode potential of a charged metal surface in contact with water. The electrode potential is obtained by reference to the potential of a neutral surface, which is itself determined with respect to a precalculated vacuum energy [78]. In this model, the excess charge of the system is compensated by a uniform jellium background representing the ionic countercharge distribution. The jellium density being inversely proportional to the volume of the supercell, the capacitance obtained from this scheme depends on the size of

Figure 4-3: Dielectric constant ϵ as a function of the reduced density ρ/ρ_0 varying the value of the smoothness exponent β.

$$\epsilon = 1 + \frac{\epsilon_S - 1}{2}\left(1 + \frac{1-(\rho/\rho_0)^{2\beta}}{1+(\rho/\rho_0)^{2\beta}}\right)$$
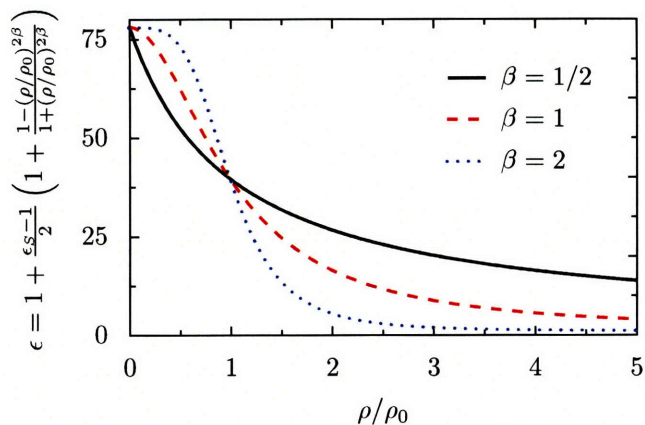
the simulation cell [78]. Additionally, as already mentioned, the determination of the average electrostatic potential in the solvent is problematic, as it involves considering number of dynamical configurations [78].

The scheme of Lozovoi and Alavi consists of determining the potential of a periodically repeated charged slab by introducing a countercharge layer in the vacuum region, thus defining the value of the reference potential and eliminating periodic-image interactions [51]. Similarly to the Helmholtz-Perrin thin-layer theory, the Lozovoi-Alavi model predicts a linear relation between the electrode potential and the surface charge.

The model introduced by Otani and Sugino consists of studying interfaces in the presence of a counterion density immersed in a solvent continuum [74]. The counterion density is obtained by solving a nonlinear electrostatic problem similar to that defined by Eq. 4.13. In their study, Otani and Sugino emphasize the influence of boundary conditions to describe solvated surfaces. (The significance of boundary conditions for metal-vacuum interfaces is also highlighted in a recent study by Lozovoi and Alavi [81].) The necessity of imposing adequate electrochemical boundary conditions in order to correctly predict the charge-voltage response of electrical double layers is discussed further in Section 4.5.

4.4 Solvation Model

4.4.1 Electrostatics in Dielectric Media

The electrostatic potential v induced by a charge distribution ρ immersed in a polarizable medium satisfies the following differential equation:

$$\nabla^2 v = -4\pi(\rho + \rho_p), \tag{4.21}$$

where $\rho_p = -\nabla \cdot \mathbf{P}$ is the charge distribution corresponding to the polarization density $\mathbf{P}$ [58]. In the linear-response regime, the induced polarization is related to the electric field $\mathbf{E} = -\nabla v$ through:

$$\mathbf{P} = \chi \mathbf{E} \tag{4.22}$$

where χ denotes the susceptibility of the medium. Substituting Eq. 4.22 into Eq. 4.21, we obtain the Poisson equation:

$$\nabla \cdot \epsilon \nabla v = -4\pi\rho, \tag{4.23}$$

where $\epsilon = 1 + 4\pi\chi$ is the dielectric constant of the polarizable continuum.

Correspondingly, the electrostatic energy can be expressed as:

$$
\begin{aligned}
E &= \frac{1}{2} \int v(\mathbf{r})\rho(\mathbf{r})d\mathbf{r} \\
&= \frac{1}{8\pi} \int \epsilon(\mathbf{r})|\nabla v(\mathbf{r})|^2 d\mathbf{r}.
\end{aligned}
\tag{4.24}
$$

In the continuum solvent model introduced by Fattebert and Gygi, the dielectric constant ϵ is taken to be locally dependent on the charge density ρ: the dielectric constant is equal to ϵ_S in regions of low charge density, while it approaches unity at higher density. As proposed by Fattebert and Gygi, the density dependence of the dielectric constant can be chosen to be a smooth analytical function of the form:

$$\epsilon(\rho) = 1 + \frac{\epsilon_S - 1}{2}\left(1 + \frac{1 - (\rho/\rho_0)^{2\beta}}{1 + (\rho/\rho_0)^{2\beta}}\right), \tag{4.25}$$

where ρ_0 is the charge-density cutoff defining the transition between the solvent and the metal, and β is the exponent characterizing the smoothness of the transition. The analytical behavior of the dielectric constant is illustrated in Figure 4-3.

Figure 4-4: Electrostatic potential in a solvent v, periodic potential v', and electrostatic correction v^{corr} averaged in the $xy-$plane parallel to the interface for a solvated Pt(100) slab. The parameters of the solvation model are $\beta = 1.25$ and $\rho_0 = 0.0005$ bohr^{-3}.
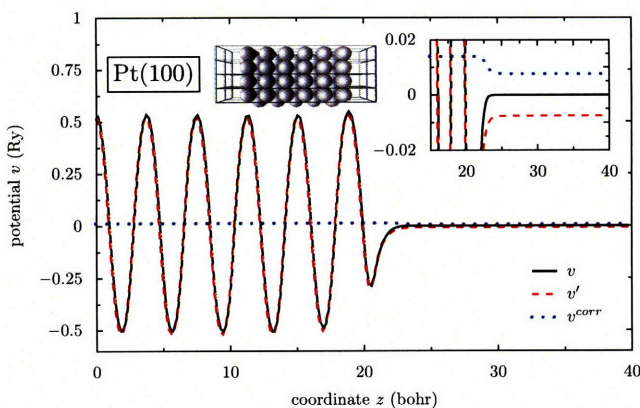
It is important to note that in the context of density-functional theory calculations, the charge-density dependence of the dielectric constant contributes an additional term to the effective electronic Hamiltonian. This additional contribution v_S can be expressed as [58]:

$$v_S(\mathbf{r}) = -\frac{1}{8\pi}|\nabla v(\mathbf{r})|^2 \frac{\partial \epsilon}{\partial \rho}(\mathbf{r}). \tag{4.26}$$

4.4.2 Definition and Analytical Characterization of the Corrective Solvation Potential

The Poisson equation in the presence of a surrounding polarizable medium can be solved efficiently using multigrid techniques [56–61]. In Figure 4-4, we compare the calculated potential to that of a periodically repeated Pt(100) slab in vacuum, obtained using conventional FFT techniques. Following the analysis presented in Chap. 3, we define the corrective potential v^{corr} as the difference between the potential of the solvated systems and its periodic counterpart:

$$v^{corr} = v - v' \tag{4.27}$$

The potential v^{corr} is seen to be constant inside the slab and in the bulk of the solvent. The two regions are connected by a smooth transition corresponding to the contribution from the solvent surface dipole (cf. Sec. 4.2). This observation suggests that the electrostatic potential v of solvated systems can be calculated by taking advantage of the periodic potential v' straightforwardly obtained from a fast Fourier transform. An efficient computational scheme exploiting this idea is presented in the next section.
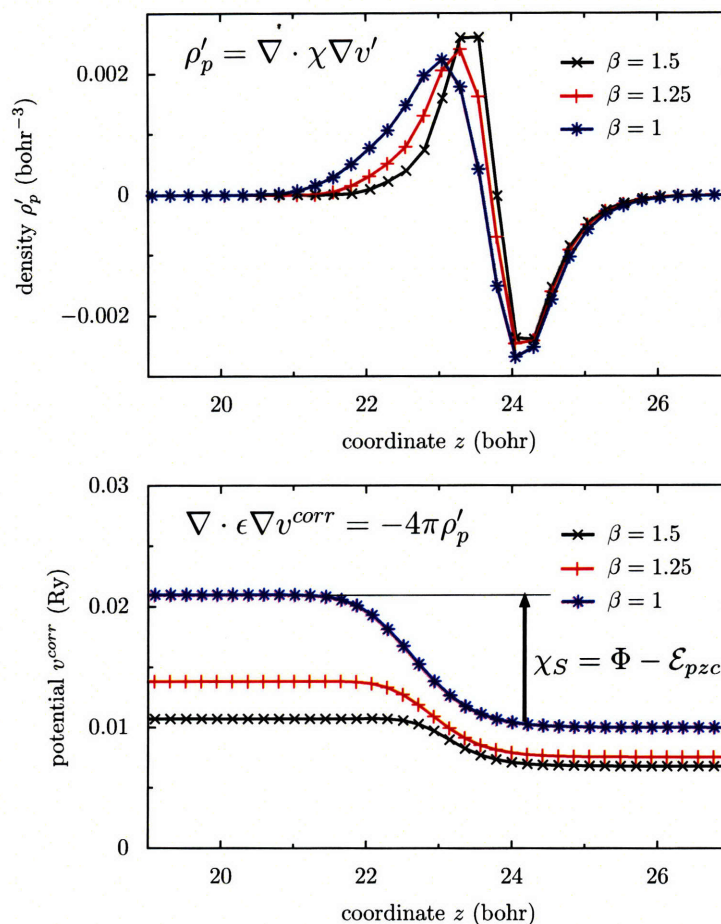
Figure 4-5: Corrective polarization charge density ρ'_p and corrective solvation potential v^{corr} for a solvated Pt(100) surface varying the value of the exponent β defining the smoothness of the dielectric transition. The value of the charge density cutoff ρ_0 is set to 0.0005 bohr^{-3}.

4.4.3 Computation of the Corrective Solvation Potential

As discussed in Chapter 3, the periodic potential obtained from a Fourier transform satisfies the following differential equation:

$$\nabla^2 v' = -4\pi(\rho - \langle\rho\rangle), \tag{4.28}$$

where $\langle\rho\rangle$ denotes the average of the total charge density inside the calculation cell, reflecting the contribution from the compensating jellium background. Substituting Eq. 4.28 into Eq.

4.23 and using the definition of the corrective potential, it can be shown that v^{corr} verifies the following differential equation:

$$\begin{cases} \nabla \cdot \epsilon \nabla v^{corr} = -4\pi(\langle \rho \rangle + \rho'_p) \\ \rho'_p = \nabla \cdot \chi \nabla v', \end{cases} \qquad (4.29)$$

where ρ'_p is the polarization charge density induced by the periodic potential. (Note that the Laplacian operator includes the dielectric constant ϵ, since the polarization charge density ρ'_p is calculated from the periodic potential v'.) Typical profiles of the polarization charge density as a function of the smoothness parameter β are plotted in Figure 4-5. It is worth noting that decreasing the value of the exponent β tends to raise the dipole potential $\chi_S = \Phi - \mathcal{E}_{pzc}$. Thus, for a given value of the charge-density cutoff ρ_0, the solvation parameter β can be direcly connected to a relevant electrochemical observable. Additionally, it should be mentioned that the corrective potential v^{corr} can be separated into two contributions: the first contribution corresponds to the corrective potential induced by the jellium background for periodic systems in vacuum; the second contribution is that from the polarization charge density of the solvent, commonly referred to as the solvent reaction field.

From the differential equation characterizing the electrostatic correction (Eq. 4.29), one can calculate the corrective solvation potential v^{corr} using an algorithm similar to that employed in the density-countercharge (DCC) method, the essential idea of which is to solve the corrective-potential differential equation on a coarse mesh with adequate boundary conditions. An application of this computational scheme is presented below.

4.4.4 Application

The convergence of the total energy of a solvated water molecule as a function of the number of grid points using the direct approach (Eq. 4.23) and the corrective-potential method (Eq. 4.29) is reported in Figure 4-6. The energy obtained from the direct approach is seen to converge slowly with respect to the resolution of the calculation mesh: for a grid of $M = 89 \times 89 \times 89$ points (equivalent to a plane-wave cutoff of $E_{cut} = 350$ Ry), the error in the total energy is larger than 0.2 Ry. This relatively poor precision contrasts with the rapid convergence obtained by calculating the corrective potential v^{corr} from Eq. 4.29. For comparison, at $M = 45 \times 45 \times 45$ points ($E_{cut} = 100$ Ry), the total energy is converged within $5 \cdot 10^{-3}$ Ry. This performance comparison clearly illustrates the interest of the corrective approach to determine the electrostatic potential of solvated systems.
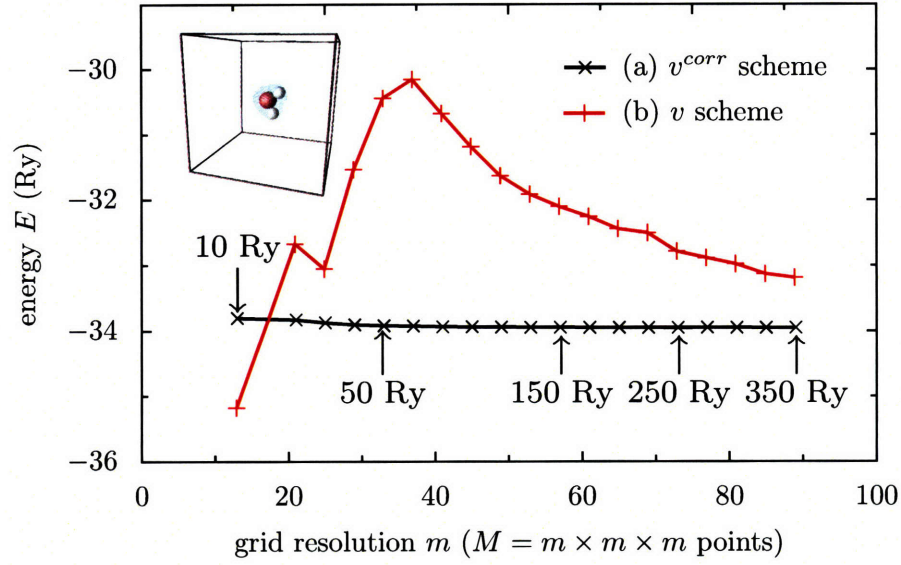
Figure 4-6: Total energy as a function of the resolution of the Poisson-solver grid for a solvated water molecule using (a) the corrective-potential method (Eq. 4.29), and (b) the direct resolution method (Eq. 4.23). The differential operator is approximated via a first-order finite-element discretization.

4.5 Modified Poisson-Boltzmann Diffuse-ionic-layer Model

4.5.1 Electrostatics in Ionic Media

We now present the modified Poisson-Boltzmann scheme for calculating the profile of the electrostatic potential across a metal-solution interface in the presence of a diffuse ionic distribution. The electrostatic potential is obtained by solving the Poisson-Boltzmann problem:

$$\nabla \cdot \epsilon \nabla v = -4\pi(\rho + \rho_d), \tag{4.30}$$

where ρ_d stands for the ionic countercharge density. In the present model, the density-dependent dielectric constant ϵ is determined from Eq. 4.25, and the countercharge distribution is chosen to be:

$$\rho_d = \begin{cases} z_d c_d \left(e^{-z_d v / k_B T} - e^{z_d v / k_B T} \right) & \text{if } \rho < \rho_1 \\ 0 & \text{if } \rho \geq \rho_1 \end{cases} \tag{4.31}$$

where the parameter ρ_1 sets the the boundary of the countercharge region. The energy reference is chosen to be the energy in the bulk of the solvent V_S.

Parenthetically, it is important to note that in the long-range or high-dilution limit Eq. 4.30 can be recast as:

$$\nabla \cdot \epsilon \nabla v + \epsilon_S \kappa^2 v = -4\pi\rho, \tag{4.32}$$

where the density-dependent wavevector κ can be expressed in terms of the Debye length L_D:

$$\kappa = \begin{cases} \dfrac{1}{L_D} & \text{if } \rho < \rho_1 \\ 0 & \text{if } \rho \geq \rho_1 \end{cases} \tag{4.33}$$

We underscore that Eq. 4.32 yields a constant interfacial capacitance as a function of the applied electrode potential. Hence, contrary to the Debye-Hueckel theory for describing ionic species in solution [82], the linearized form of the Poisson-Boltzmann equation is generally inadequate for predicting the electrical response of double-layer interfaces.

4.5.2 Diffuse-ionic-layer Algorithm

As proposed by Otani and Sugino [74], the nonlinear problem defined by Eqs. 4.30 and 4.31 can be solved via a self-consistent procedure. Our scheme consists of determining the corrective potential v^{corr} as the solution of the following self-consistent equation:

$$\nabla \cdot \epsilon \nabla v^{corr} = -4\pi(\langle \rho \rangle + \rho_p' + \rho_d) \tag{4.34}$$

The main advantage of this approach is that it allows the use of optimized linear multigrid solvers [56–61] despite the nonlinear nature of the electrostatic equation. Note that in most cases, no more than five self-consistent iterations are necessary to converge the corrective solvation potential v^{corr} within 10^{-10} Ry at each grid point.

We employ this scheme to calculate the electrostatic profile of a Pt(100) slab of surface charge $\sigma \approx 0.1$ C·m^{-2} immersed in a monovalent ionic solution of concentration $c_d = 0.0001$ M at ambient temperature. Homogeneous Dirichlet boundary conditions are imposed to the electrostatic potential v. The profile of the electrode potential as a function of cell size is reported in Figure 4-8a. We observe that the convergence of the electrostatic profile is very slow due to the poor screening of the electric field in the dilute electrolyte.

In order to improve the convergence of the electrostatic profile with respect to the size
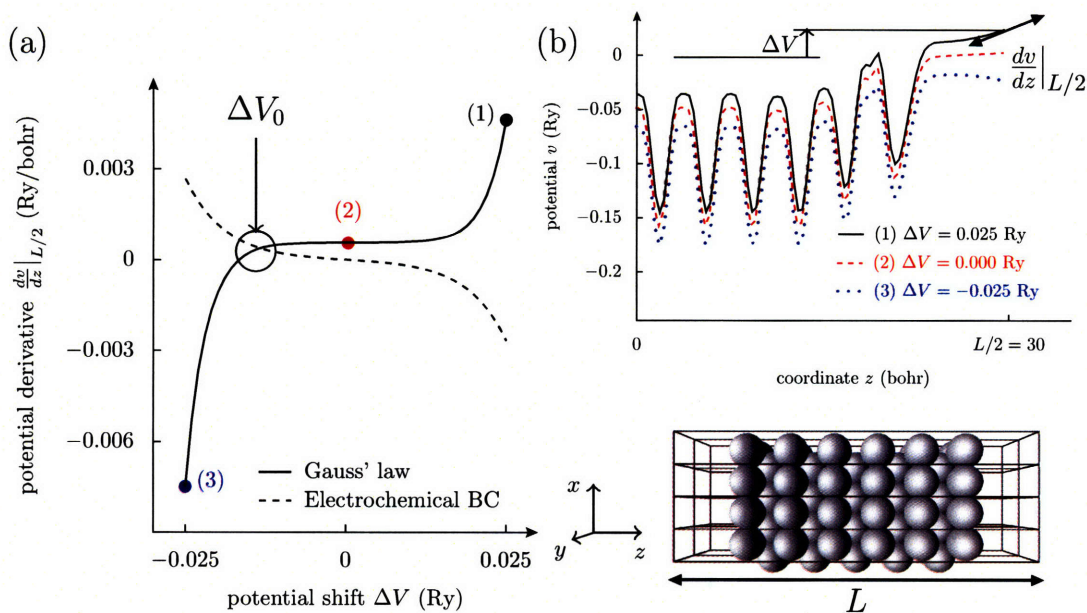
Figure 4-7: Determination of the electrochemical boundary conditions for solvated interfaces. Graph a illustrates the calculation of the potential shift ΔV_0 at the boundaries $z = \pm L/2$ by equating the electrostatic-potential derivatives that are obtained from Gauss' law and from the electrochemical boundary condition. Changes in the electrostatic-potential profile as a function of the potential shift are depicted in graph b.

of the calculation domain, adequate boundary conditions must be applied to the electrostatic potential. Boundary conditions specific to solvated electrodes can be derived from the standard double-layer models. Indeed, at a long distance from the interface, the electrostatic potential is related to the electric field through Eq. 4.14. In what follows, the boundary conditions defined by this asymptotic relation will be referred to as *electrochemical boundary conditions*.

In order to impose electrochemical boundary conditions at the boundary of the supercell, we employ the method that is illustrated in Figure 4-7. The procedure consists of applying a constant energy shift ΔV_0 to the electrostatic potential v in order to simultaneously satisfy Gauss' law and electrochemical conditions at the cell boundaries. It is important to note that in applying Gauss' law, the total charge in the unit cell must be calculated taking into account charge redistribution in the ionic layer. Once the adequate energy shift ΔV_0 is found, the potential is relaxed with fixed boundary conditions. The procedure is repeated until convergence of the electrostatic profile.

Figure 4-8: Electrostatic-potential profile for a Pt(100) surface immersed in a dilute ionic solvent imposing (a) homogeneous Dirichlet boundary conditions ($v(\pm L/2) = 0$), and (b) electrochemical boundary conditions (Eq. 4.14).

Figure 4-9: Electrode potential as a function of transverse cell size for a Pt(100) surface immersed in a dilute ionic solvent imposing (a) homogeneous Dirichlet boundary conditions ($v(\pm L/2) = 0$), and (b) electrochemical boundary conditions (Eq. 4.14).
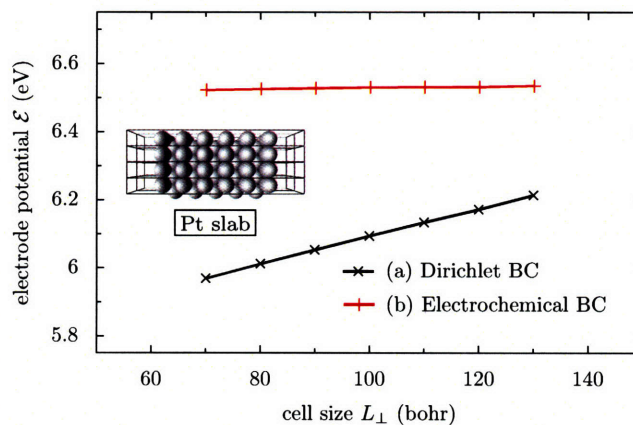
Exploiting the corrective-potential scheme presented in Sec. 4.4 and the potential-shift method outlined above, we introduce a diffuse-ionic-layer (DIL) algorithm for solving the modified Poisson-Boltzmann self-consistent problem subject to electrochemical boundary conditions. The DIL algorithm is described below:

DIL Algorithm

1. Start with an initial charge distribution ρ and an initial potential v on the fine grid. Calculate the periodic potential v' in vacuum (FFT techniques), the density-dependent dielectric constant ϵ, and the polarization charge density ρ'_p.

2. Interpolate ρ, v, v', ϵ, and ρ'_p on a coarse grid (tricubic interpolation [63]) to obtain $\tilde{\rho}$, $\tilde{v}$, $\tilde{v}'$, $\tilde{\epsilon}$, and $\tilde{\rho}'_p$.

3. Determine the potential shift ΔV_0 to satisfy Gauss' law and the electrochemical boundary condition (dichotomy procedure).

4. Calculate the diffuse ionic density $\tilde{\rho}_d$ on the coarse grid.

5. Set the boundary condition for the corrective potential $(\tilde{v}^{corr} = \tilde{v} + \Delta V_0 - \tilde{v}')$.

6. Solve $\nabla \cdot \epsilon \nabla \tilde{v}^{corr} = -4\pi(\langle \rho \rangle + \rho'_p + \rho_d)$ (multigrid techniques) to obtain the corrective potential $\tilde{v}^{corr}$.

7. Update the electrostatic potential $\tilde{v} = \tilde{v}' + \tilde{v}^{corr}$.

8. Iterate from Step 3 until convergence.

9. Transfer the electrostatic correction $\tilde{v}^{corr}$ to the fine grid (tricubic interpolation) to obtain v^{corr}.

10. Compute the corrected electrostatic potential $v = v' + v^{corr}$.

This computational procedure can be efficiently incorporated in most electronic-structure self-consistent-field (SCF) schemes with a moderate increase in computational cost: in the calculations presented above, the additional computational cost is of $\sim$8%. One key advantage of the algorithm is that, similarly to the DCC scheme, it offers the option of updating the corrective potential at fixed interval between SCF iterations, which results in a significant gain in efficiency. The improved convergence of the electrostatic profile v as a function of

CHAPTER 4 MODIFIED POISSON-BOLTZMANN DIFFUSE-IONIC-LAYER MODEL

cell size obtained by imposing electrochemical boundary conditions is illustrated in Figure 4-8b. A comparison of the convergence of the electrode potential is reported in Figure 4-9. We observe that while the error in $\mathcal{E}$ is on the order of 0.5 eV using homogeneous Dirichlet boundary conditions, the potential rapidly converges within a few meV using electrochemical boundary conditions.

To close this section, we draw attention to the electrostatic energy contribution E_d from the ionic solvent outside the calculation cell. This energy contribution can be written as:

$$E_d = \frac{1}{2} \int_{L/2}^{+\infty} \rho_d(z) v(z) dz.$$ (4.35)

Using the long-range linearization of the Gouy-Chapman electrostatic problem (Eq. 4.18) at sufficiently large unit cells, the electrostatic energy E_d can be approximated as:

$$E_d \approx c_d S L_D k_B T \left(1 - \cosh \frac{z_d v(L/2)}{k_B T} \right),$$ (4.36)

where S is the area of the unit cell in the xy-plane.

4.5.3 Applications

The charge-voltage and capacitance-voltage characteristics of a Pt(100) interface as a function of the ionic concentration are depicted in Figures 4-10 and 4-11. The metal electrode is modeled using an eleven-layer-thick slab. The size of supercell in the transverse direction is of 80 bohr. We employ ultrasoft pseudopotentials with plane-wave energy cutoffs of 40 and 400 Ry. The Brillouin zone is sampled using a $5 \times 5 \times 1$ mesh with cold-smearing occupations (the smearing temperature is 0.05 Ry). The parameters of the DIL model are selected to be $\epsilon_S = 78$, $k_B T = 0.0025$ Ry, $\rho_0 = 0.0005$ bohr^{-3}a, $\rho_1 = 0.0001$ bohr^{-3}, and $\beta = 1.25$.

Using homogeneous Dirichlet boundary conditions, we observe that the electrical response of the platinum electrode remains linear for all concentrations in the range 0.0001 to 0.1 M (Figure 4-10a). This behavior contrasts with the significant decrease in the charge-voltage slope occuring at the potential of zero charge for electrodes subject to electrochemical boundary conditions (Figure 4-10b). The significance of electrochemical boundary conditons is also highlighted in Figure 4-11. Indeed, the contribution from the ionic layer—which causes a marked drop in electrode capacitance at low concentration—is almost completely suppressed when homogeneous Dirichlet boundary conditions are imposed. These results confirm the
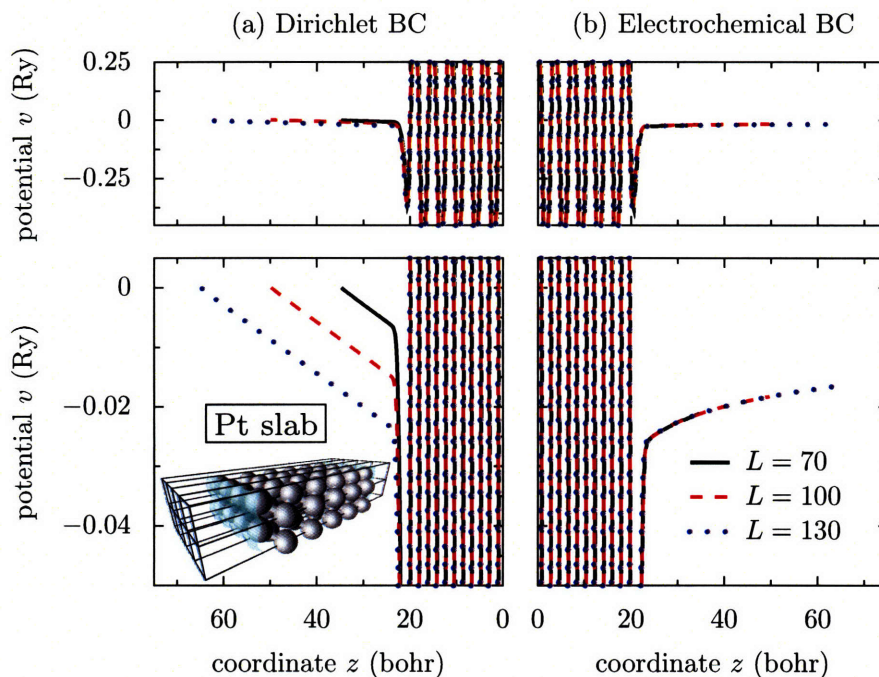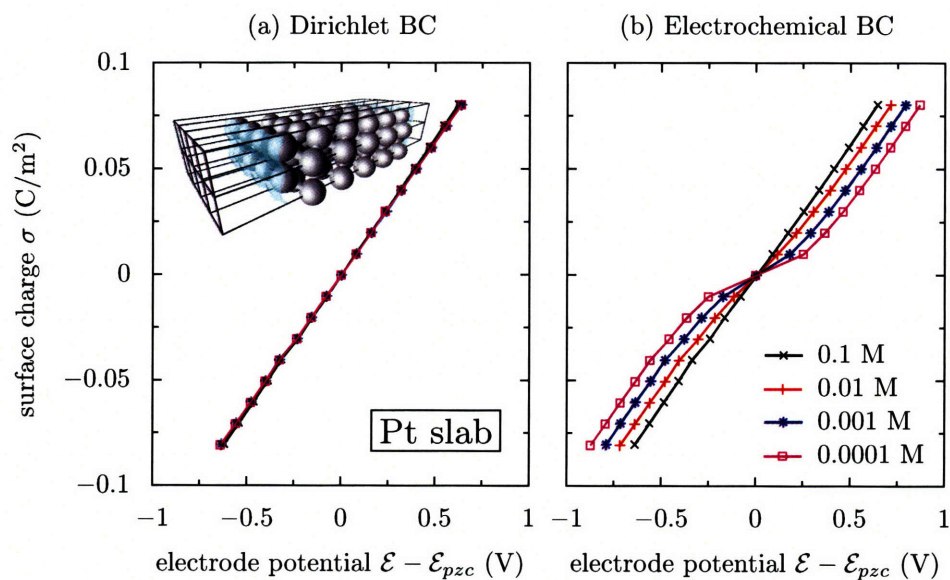
Figure 4-10: Surface charge as a function of the electrode potential for a Pt(100) surface immersed in an ionic solvent imposing (a) homogeneous Dirichlet boundary conditions, and (b) electrochemical boundary conditions.

Figure 4-11: Differential capacitance as a function of the electrode potential for a Pt(100) surface immersed in an ionic solvent imposing (a) homogeneous Dirichlet boundary conditions, and (b) electrochemical boundary conditions.
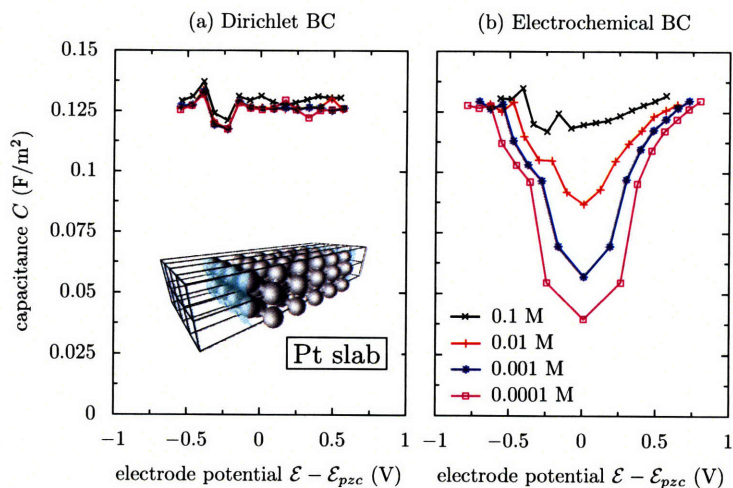
importance of electrochemical boundary conditions to study electrical double layers in dilute ionic solutions.

4.6 Conclusion

This study has presented a modified Poisson-Boltzmann diffuse-ionic-layer (DIL) model for studying electrified interfaces under electrochemical conditions, particularly focusing on important length-scale limitations for the description of the ionic electrolyte. We have shown that the electrostatic contribution from the ionic solvent can be calculated independently at low computational cost using multigrid techniques and taking advantage of the periodic solution of the electrostatic problem. We have also emphasized the necessity of imposing adequate electrochemical boundary conditions to properly describe the predominant electrical response of ionic layer at the point of zero charge. The DIL algorithm improves on recently proposed methods by allowing a direct and inexpensive first-principles representation of electrified-metal-solution interphases beyond high-concentration conditions. .

Vibrational Recognition of Adsorption Sites for Carbon Monoxide on Platinum-Ruthenium Surfaces

5.1 Introduction

FUEL CELLS ARE ENERGY CONVERSION SYSTEMS of potentially high environmental benefit [6] that provide electricity and heat by catalytic conversion of a fuel, such as hydrogen or methanol. Despite their advantages, several technological obstacles have hindered the deployment of fuel-cell systems. For low-temperature fuel cells that use platinum as electrode material, one major limitation is CO poisoning, whereby CO occupies active sites on the platinum catalyst and prevents fuel oxidation [83]. Typically, in polymer electrolyte membrane fuel cells (PEMFCs), CO concentrations must be brought below 10-50 ppm to maintain an acceptable catalytic performance. For comparison, CO concentrations are generally on the order of thousands of ppm in reformed hydrogen fuels [84, 85]. CO poisoning is even more problematic for direct methanol fuel cells (DMFCs) since CO is always present in critical amounts as an intermediate in methanol oxidation [86].

Ruthenium islands on platinum catalysts have been shown to considerably attenuate CO poisoning [87–89], although the microscopic details of this phenomenon are not completely understood. Two main mechanisms have been proposed to explain this improved tolerance to CO. Within the bifunctional mechanism model, adsorbed OH species generated by water dissociation at the platinum/ruthenium edge promote the oxidation of CO (*the promo-*

tion effect) [86,88–92]. According to an alternative view, ruthenium modifies the electronic structure of neighboring platinum atoms, reducing their affinity for CO (*the ligand/intrinsic effect*) [86,92]. To investigate further these mechanisms of central interest to fuel-cell technology, it is necessary to elucidate the nature of the chemical interaction between CO and bimetallic surfaces.

In most cases, density-functional theory provides a reliable description of molecular adsorption and dissociation on transition metals [93–98]. However, CO adsorption on transition-metal surfaces is unexpectedly problematic. Indeed, at low CO coverage, local and generalized-gradient density-functional calculations predict CO adsorption on Pt(111) to take place at the fcc site, contradicting low-temperature experiments, which unambiguously indicate atop adsorption. This well-known qualitative discrepancy (the "CO/Pt(111) puzzle") [99] precludes an accurate description of important phenomena, such as the surface diffusion of CO adsorbates and the thermal population of CO adsorption sites. Similar qualitative errors have been reported for CO adsorbed on rhodium and copper surfaces [99–101], and a wide body of literature exists on the subject [102–113].

In this work, we highlight and rationalize the accuracy of density-functional calculations in predicting the stretching frequencies of CO adsorbed on platinum and platinum-ruthenium surfaces, notwithstanding the failure in predicting the most stable adsorption site. We first present density-functional theory and density-functional perturbation theory results for the energetic, structural and vibrational properties of adsorbed CO. Second, we introduce a novel orbital-resolved force analysis to clarify the electronic origins of the C–O frequency shifts as a function of the adsorption site. Last, we rationalize the accuracy of the stretching-frequency predictions by analyzing the influence of donation and backdonation using a GGA + molecular U model recently introduced by Kresse, Gil, and Sautet [102].

5.2   Theoretical Basis

The (111) transition-metal surface is modeled using a periodically repeated slab composed of four layers, each layer containing four atoms per supercell. A $\sqrt{3} \times 2$ adsorption structure corresponding to a coverage of 1/4 of the monolayer (ML) is adopted for the CO overlayer. Atomic cores are represented by ultrasoft pseudopotentials [21] (cf. Appendix C). The exchange-correlation energy is calculated within the Perdew-Burke-Ernzerhof generalized-gradient approximation (PBE-GGA) [16]. The size of the vacuum region separating the periodic slabs is ≈ 13 Å. We use a shifted $4 \times 4 \times 1$ mesh with cold-smearing occupations [12]

site	atop	bridge	hcp	fcc
E_{ads} (eV)	1.61 $(1.30)^2$	1.71	1.72	1.74
d(C–O) (Å)	1.153 $(1.15\pm0.05)^3$	1.177 $(1.15\pm0.05)^3$	1.188	1.189
d(M–C) (Å)	1.864 $(1.85\pm0.1)^3$	2.029 $(2.08\pm0.07)^3$	2.116	2.121
h(C) (Å)[1]	2.017	1.543	1.380	1.373
θ(CO) (deg)[1]	1.4	1.4	0.5	0.4
ν(C–O) (cm^{-1})	2050 $(2070)^4$	1845 $(1880)^4$	1752 $(1760)^4$	1743 $(1760)^4$
ν(M–C) (cm^{-1})	584 $(470)^5$	413 $(380)^5$	358	344
bending modes (cm^{-1})	392 386	393 346	329 315	328 300
other modes (cm^{-1})	0 to 230	0 to 231	0 to 196	0 to 186

[1]h(C) denotes the distance from C to the first surface layer, and θ(CO) denotes the tilt angle of CO. [2]Ref. [115]. [3]Ref. [116]. [4]Ref. [4]. [5]Ref. [117].

Table 5.1: Adsorption energies, structural properties, and vibrational frequencies calculated using density-functional theory and density-functional perturbation theory for CO adsorbed on clean Pt(111) surfaces.

(smearing temperature of 0.4 eV) to sample the Brillouin zone. Energy cutoffs of 24 and 192 Ry are applied to the plane-wave expansions of the wavefunctions and charge density, respectively. As discussed in Ref. [99], the system is not spin-polarized. Using the above slab thickness and calculation parameters, we verify that the adsorption energies are converged within less than 10 meV and the atomic forces within a few meV/Å.

The bond length and stretching frequency of CO in the gas phase are calculated to be 1.140 Å and 2140 cm^{-1} (experimental values are 1.128 Å and 2170 cm^{-1}). The PBE-GGA lattice parameter and bulk modulus of platinum are 3.993 Å and 2.36 Mbar, in good agreement with experimental values of 3.923 Å and 2.30 Mbar [114]. All our calculations use fully relaxed configurations.

site	atop	hcp	fcc	atop	hcp	fcc
slab	1 ML Ru/ 3 ML Pt	1 ML Ru/ 3 ML Pt	1 ML Ru/ 3 ML Pt	2 ML Ru/ 2 ML Pt	2 ML Ru/ 2 ML Pt	2 ML Ru/ 2 ML Pt
E_{ads} (eV)	2.24	2.27	2.15	1.96	2.05	1.88
d(C–O) (Å)	1.161	1.196	1.192	1.161	1.201	1.190
d(M–C) (Å)	1.892	2.132	2.104	1.922	2.122	2.111
h(C) (Å)[1]	2.014	1.375	1.412	1.970	1.318	1.437
θ(CO) (deg)[1]	3.3	0.9	2.6	4.1	0.6	1.44
ν(C–O) (cm^{-1})	1979 (1970)[2]	1702	1724	1969 (1970)[2]	1666	1739
ν(M–C) (cm^{-1})	510	356	358	482	355	351
bending modes (cm^{-1})	412 409	258 247	221 215	396 389	315 301	251 231
other modes (cm^{-1})	0 to 208	0 to 205	0 to 201	0 to 265	0 to 254	0 to 226

[1]h(C) denotes the distance from C to the first surface layer, and θ(CO) denotes the tilt angle of CO. [2]Ref. [4].

Table 5.2: Adsorption energies, structural properties, and vibrational frequencies calculated using density-functional theory and density-functional perturbation theory for CO adsorbed on ruthenium-covered Pt(111) surfaces.

5.3 Results

We report the results of our density-functional calculations in Tables 5.1 and 5.2. For platinum surfaces, the calculated atop binding energy E_{ads}(atop) = 1.61 eV is consistent with that reported in Ref. [118] (1.55 eV in the same adsorption structure). As a matter of comparison, the experimental heat of adsorption at 1/4 ML CO is 1.30 eV. The relative adsorption energy E_{ads}(atop) − E_{ads}(fcc) is calculated to be 0.13 eV, in accordance with the gradient-corrected relative adsorption energies (ranging from −0.10 to −0.25 eV) reported in Ref. [99]. As expected, our density-functional calculations favor CO adsorption at the threefold fcc and hcp adsorption sites for platinum and platinum-ruthenium surfaces, confirming the aforementioned disagreement with experiments. (Note that bridge adsorption of CO on platinum-ruthenium surfaces is predicted to be energetically unstable.) Despite this noteworthy failure, the bond length d(C–O) is calculated to be 1.153 Å at the atop site and 1.177 Å at the bridge site on platinum, in good agreement with experimental bond lengths (1.15±0.05 Å at both the atop and fcc sites). Similarly, the distance d(Pt–C) from the carbon to its nearest platinum neighbor, calculated to be 1.864 Å at the atop site and 2.029 Å at the fcc site, is always

within experimental error (experimental bond lengths are 1.85±0.1 Å and 2.08±0.07 Å at the atop and fcc sites, respectively). Note that both bond lengths increase with coordination.

The full phonon spectra for CO adsorbed at the atop, bridge, hcp, and fcc sites on platinum and platinum-ruthenium surfaces are calculated using density-functional perturbation theory (DFPT) [19]. Within this approach, the full dynamical matrix of the system is computed exactly by solving the self-consistent linear-response problem describing the electron response to atomic perturbations of arbitrary wavelength. The DFPT spectra reported in Tables 5.1 and 5.2 exhibit some common and expected features. The highest vibrational frequency in the range [1700 cm^{-1}, 2100 cm^{-1}] corresponds to the localized C–O stretching mode. The second highest frequency ν(M–C) in the range [300 cm^{-1}, 600 cm^{-1}] is related to the stretching of the metal-carbon bond. This mode is followed by two CO bending modes with frequencies lying 20-200 cm^{-1} below ν(M–C). All the other modes involving displacements of the heavy metal atoms are found in the frequency range [0 cm^{-1}, 300 cm^{-1}].

We now focus on the dependence of the C–O stretching frequency as a function of the adsorption site. Upon atop adsorption on platinum, the predicted ν(C–O) is reduced from 2140 cm^{-1} to 2050 cm^{-1}, corresponding to a red shift $\Delta\nu$(C–O) of −90 cm^{-1}. For comparison, the experimental stretching frequency, as obtained by means of sum-frequency generation (SFG) spectroscopy [4], decreases from 2170 cm^{-1} to 2070 cm^{-1}, corresponding to $\Delta\nu$(C–O) = −100 cm^{-1}. The frequency shifts are even more marked at high-coordination sites: ν(C–O) is predicted to be 1845 cm^{-1}, 1752 cm^{-1}, and 1743 cm^{-1} at the bridge, hcp, and fcc sites, corresponding to red shifts of up to −397 cm^{-1}. These DFPT stretching frequencies show remarkable agreement with their SFG counterparts: ν(C–O) = 1830 cm^{-1} at the twofold bridge site, ν(C–O) = 1760 cm^1 at the threefold hcp and fcc sites, corresponding to a maximum red shift of −410 cm^{-1}. Accurate DFPT frequencies are also obtained for CO adsorbed on platinum-ruthenium bimetallic surfaces. Indeed, the calculated stretching frequencies 1979 cm^{-1} (1 Ru ML) and 1969 cm^{-1} (2 Ru ML) at the atop site compare very closely to the SFG result of 1970 cm^{-1}.

In conclusion, all calculated CO stretching frequencies deviate by less than 2% from the measured ones, irrespective of the adsorption site and nature of the metal surface. The correct prediction of the frequency red shifts allows the direct recognition of CO adsorption sites and confirms that CO preferentially occupies atop sites on platinum-ruthenium bimetallic surfaces. This very close agreement with experiment is made more remarkable by the lack of accuracy of the PBE-GGA adsorption energies. In the remainder of this work, we show how this accuracy can be rationalized in terms of the hybridization of the CO molecular orbitals

	gas phase	atop	bridge	hcp	fcc
$f_{2\pi_x^*}/2 + f_{2\pi_y^*}/2$	0.00	0.25	0.37	0.41	0.41
$f_{5\sigma}$	1.00	0.92	0.92	0.92	0.92
$f_{1\pi_x}/2 + f_{1\pi_y}/2$	1.00	1.00	0.99	0.99	0.99
$f_{4\sigma^*}$	1.00	1.00	1.00	1.00	1.00
$f_{3\sigma}$	1.00	1.00	1.00	1.00	1.00
bond order	3.00	2.35	2.16	2.09	2.09

Table 5.3: Molecular occupations and bond order for CO in the gas phase and for CO adsorbed on platinum.

with the metal bands.

5.4 Discussion

5.4.1 Electronic Origins of the Frequency Shifts

The hybridization of the metal d bands with the $2\pi^*$ lowest unoccupied molecular orbitals (LUMOs) and the 5σ highest occupied molecular orbital (HOMO) plays a predominant role in the adsorption energy of CO on transition metals. According to the Blyholder model [119], these electronic interactions result in electron donation (i.e., partial depletion of the 5σ orbital) and electron backdonation (i.e., partial filling of the $2\pi^*$ orbital). It has been shown that the trends of the adsorption energies of CO on transition-metal surfaces can be correlated to the amounts of donation and backdonation (Hammer-Morikawa-Nørskov model) [93]. Among the suggested solutions to the "CO/Pt(111) puzzle"—e.g., nonequivalent GGA description of different bond orders [103], incorrect singlet-triplet CO excitation energies [104], effect of metal semicore polarization [105]—Kresse, Gil, and Sautet have proposed that the inaccuracy of density-functional calculations in determining the most stable adsorption site is due to an overestimation of the interaction between the $2\pi^*$ orbitals and the metal bands, resulting from an underestimation of the HOMO-LUMO gap [102]. As discussed in the next section, this interpretation recovers the essential features of CO adsorption on transition metals: it identifies the tendency of local and generalized-gradient DFT to delocalize and overhybridize electronic states. Nevertheless, as shown below, the site-dependence of the C–O bond length and vibrational frequency is not affected by the LUMO and HOMO hybridizations. In other words, the hybridizations that subtly determine the relative CO adsorption energies do not

(a) Atop DOS
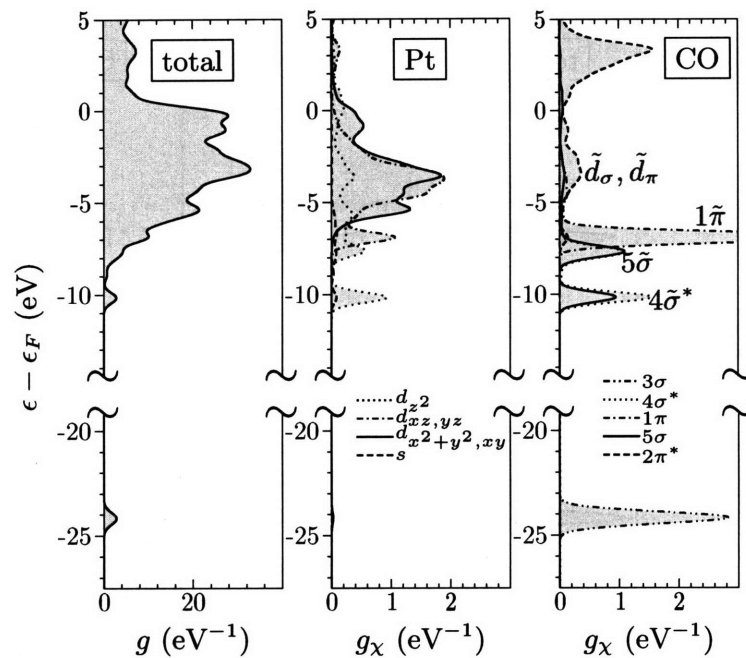
(b) Fcc DOS
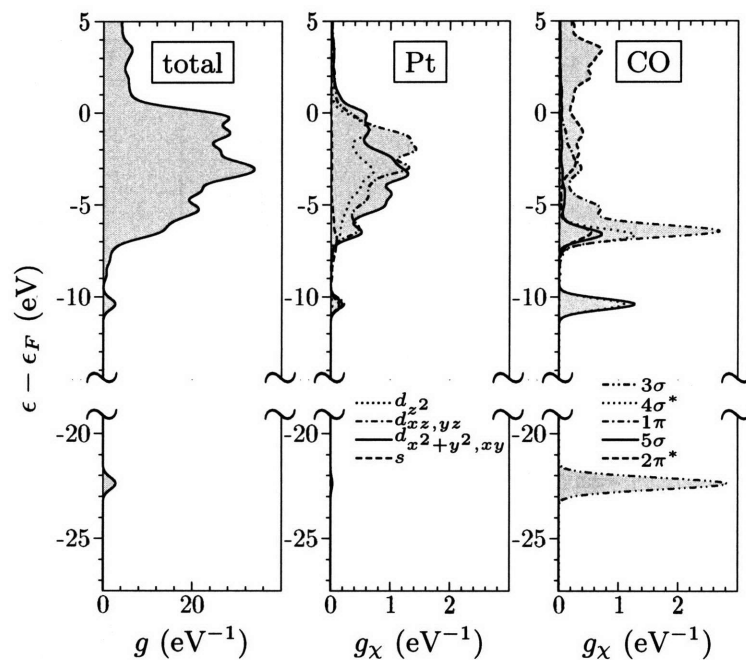
Figure 5-1: Total density of states, density of states projected on the Pt atomic orbitals, and density of states projected on the CO molecular orbitals for atop and fcc adsorption of CO on Pt(111).

(a) Atop FDOS
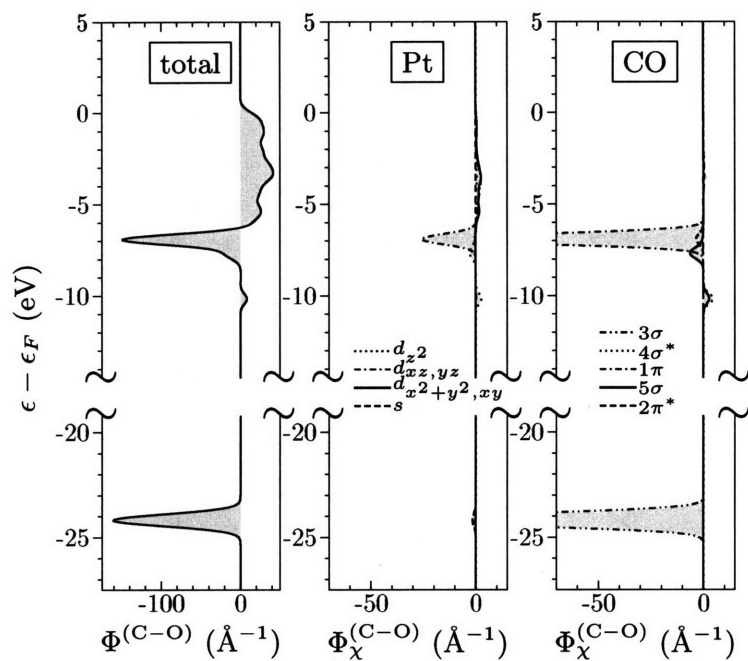
(b) Fcc FDOS
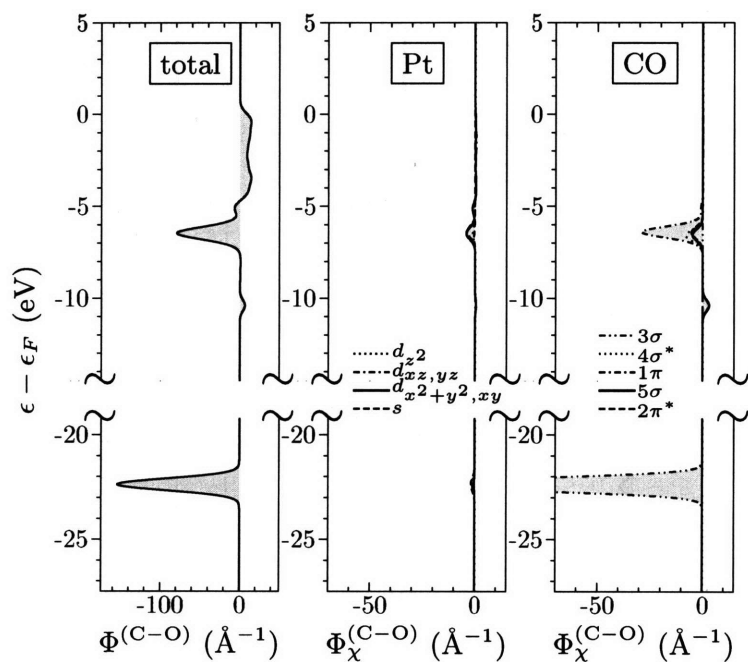
Figure 5-2: Total force density of states, force density of states projected on the Pt atomic orbitals, and force density of states projected on the CO molecular orbitals for atop and fcc adsorption of CO on Pt(111).
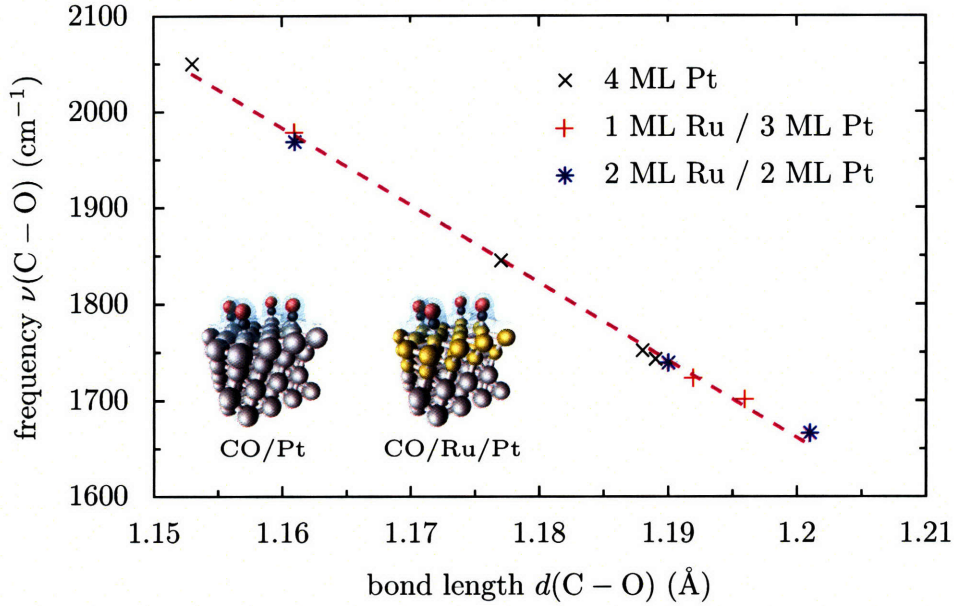
Figure 5-3: Correlation between bond length and intramolecular frequency for CO on clean and ruthenium-covered Pt(111) surfaces.

influence the structural and vibrational predictions.

To establish this fact, we first introduce a spectral force analysis. The main objective of this analysis is to separate and assess the contribution from each CO molecular orbital to the force F acting on a given atom. The central quantity we introduce is $\Phi_{I,\chi}(\epsilon)$, the force density of states (FDOS) of the orbital χ, which is defined as the χ-resolved density of states weighted by the wavefunction contribution to the force $\mathbf{F}_I$ acting on atom I. To be more explicit, the FDOS of a given CO molecular orbital χ can be expressed as:

$$\Phi_{I,\chi}(\epsilon) = \sum_i \mathbf{F}_{I,i} |\langle \chi | \psi_i \rangle|^2 \delta(\epsilon - \epsilon_i), \qquad (5.1)$$

where ψ_i denotes the electronic wavefunction, ϵ_i is the electronic energy, and $\mathbf{F}_{I,i} = -f_i \int |\psi_i|^2 \partial v / \partial \mathbf{R}_I$ is the wavefunction contribution to the force $\mathbf{F}_I$. (The calculation of the overlap $\langle \chi | \psi_i \rangle$ in the ultrasoft formalism is detailed in Appendix D.) It should be noted that, by summing the integrated FDOS $\Phi_{I,\chi}(\epsilon)$ over a complete set of orbitals satisfying orthonormality, one obtains the total electronic force acting on atom I. As a consequence,

the FDOS can be quantitatively connected to relevant observables. Additionally, by projecting the force density of states along the normalized atomic displacements Δ_I^{C-O} corresponding to the C–O stretching mode, we obtain the force density of states along the stretching mode $\Phi_\chi^{C-O}(\epsilon) = \sum_I \Delta_I^{C-O} \cdot \Phi_{I,\chi}(\epsilon)$, to be heuristically identified as the orbital contribution to the intramolecular force.

The orbital-projected density of states (DOS) $g_\chi(\epsilon) = \sum_i |\langle \chi | \psi_i \rangle|^2 \delta(\epsilon - \epsilon_i)$ is commonly used to provide an insightful picture of the electronic hybridizations that take place when CO is adsorbed on platinum. Similarly, $\Phi_\chi^{C-O}(\epsilon)$ describes the influence of electronic hybridizations on the force along the C–O stretching mode. The projected densities of states $g_\chi(\epsilon)$ and projected force densities of states $\Phi_\chi^{C-O}(\epsilon)$ for different adsorption sites are plotted in Figures 5-1 and 5-2. A detailed analysis of the orbital-resolved densities of states is given in Ref. [102]. For the purpose of our study, we emphasize the following features. When CO adsorbs on Pt(111), the $4\sigma^*$ and 5σ orbitals hybridize with the metal d_{z^2} band, generating $4\tilde{\sigma}^*$ and $5\tilde{\sigma}$ states with mainly adsorbate character (adopting the terminology of Ref. [120], the tilde symbol denotes hybrid states). These $4\tilde{\sigma}^*$ and $5\tilde{\sigma}$ states are found in the energy ranges $[-12$ eV, -9 eV$]$ and $[-9$ eV, -5 eV$]$ relative to the Fermi level. Above -5 eV, the 5σ orbital and the d_{z^2} band generate a $\tilde{d}_\sigma$ band with predominant metal character. This interaction results in a partial depletion of the 5σ HOMO (electron donation). In addition, the interaction between the 1π and $2\pi^*$ orbitals and the d_{xz} and d_{yz} bands produces $1\tilde{\pi}$ states in the range $[-9$ eV, -5 eV$]$ and a broad $\tilde{d}_\pi$ band above -5 eV, causing partial occupation of the $2\pi^*$ LUMOs (electron backdonation) [119]. The changes in molecular orbital occupations due to CO adsorption are reported in Table 5.3.

In order to understand how the generation of these hybrid states affects the intramolecular force, we turn to the FDOS (Figure 5-2). The graphs are plotted according to the convention that bonding states (i.e., opposed to the stretching of the C–O bond) correspond to negative values of Φ_χ^{C-O}. First, we note that the bonding contribution from the 3σ state does not vary with the adsorption site, confirming that the 3σ state retains a strong molecular character. Additionally, we observe that the $5\tilde{\sigma}$ and $1\tilde{\pi}$ states are bonding while the $4\tilde{\sigma}^*$ is antibonding, as expected intuitively. In the energy region above -5 eV, another contribution appears. This contribution corresponds to high-energy wavefunctions located inside the platinum slab, as evidenced by the absence of any molecular-orbital force contribution above -5 eV. Nevertheless, due to their metal character, the contribution of these high-energy wavefunctions is mostly canceled by the positively charged platinum cores. Consequently, the local contribution from the hybrid states of strong molecular character prevails.

Besides these observations, the main feature of the FDOS graphs is the predominant bonding contribution between -9 eV and -5 eV. At the atop site, the curve displays a sharp negative peak which corresponds mainly to the 1π orbital-resolved contribution $\Phi_{1\pi}^{C-O}(\epsilon)$. At the fcc site, both the magnitude and the relative share of the peak are reduced, clearly indicating that the $1\tilde{\pi}$ states have more influence on the change in intramolecular bonding than any of the other hybrid wavefunctions. The $1\tilde{\pi}$ states maintain a predominant 1π character at the atop site, whereas at high-coordination sites this molecular character is significantly reduced due to a stronger hybridization with the substrate. Therefore, the 1π bonding contribution to the intramolecular force decreases with site coordination. As intramolecular bonding decreases, the C–O bond length increases. The predominance of the 1π bonding contribution is confirmed by the density-distribution analysis initially introduced by Zupan, Burke, Ernzerhof, and Perdew [121], as discussed in Appendix E.

For CO adsorbed on transition metal surfaces, the intramolecular bond length and the intramolecular stretching frequency are strongly correlated. An extensive study of Gajdoš, Eichler, and Hafner [122] showed a linear correlation between d(C–O) and ν(C–O) for CO adsorbed on close-packed transition metals: ν(C–O) shifts down in frequency as d(C–O) increases. As illustrated in Figure 5-3, a similar trend is observed for CO adsorbed on ruthenium-covered platinum surfaces. Therefore, the increase in C–O bond length at high-coordination sites, which reflects a decrease in 1π bonding contribution, is accompanied by a reduction of the C–O stretching frequency.

While the preceding is consistent with the interpretation given in Refs [119, 120, 122], it is important to make one central observation: although the LUMO $2\pi^*$ filling is a reasonable measure of the amount of hybridization between the 1π, $2\pi^*$ orbitals and the metal d_{xz}, d_{yz} bands, filling the $2\pi^*$ orbitals does not directly weaken the bond, as evidenced by the very low values of $\Phi_{2\pi^*}^{(C-O)}$ in the energy range $[-9$ eV, -5 eV$]$. This interpretation helps explaining the fact that the CO adsorption energies do not show a well-defined relationship with the C–O stretching frequency [123, 124].

The main conclusion of this section is as follows. At variance with the CO adsorption energies, electron backdonation and electron donation have little direct bearing on the intramolecular forces. Their immediate effect on the molecular bond length and stretching frequency cannot account for the observed shifts. Instead, the changes in bond length and stretching frequency are primarily related to the hybridization of the 1π molecular orbitals. This provides important indications as to why the structural and vibrational properties of CO adsorbed on platinum and platinum-ruthenium surfaces are accurately predicted. The GGA

+ molecular U study presented in the next part provides additional quantitative evidence in support to this conclusion.

5.4.2 Influence of Donation and Backdonation on the Accuracy of the Frequency Predictions

As mentioned above, the failure of density-functional calculations in predicting CO adsorption energies is traceable to an overhybridization of the CO molecular orbitals with the metal bands [102, 125]. To assess the influence of this overhybridization on the accuracy of the calculated adsorption energies, bond lengths, and vibrational properties, we have performed a sensitivity analysis. This analysis consists of controlling and varying the HOMO and LUMO hybridizations, while monitoring the variations of the mentioned observables. To this end, we have used the GGA + molecular U approach introduced by Kresse, Gil, and Sautet [102]. This approach (inspired by the LDA + U method [28]) consists of adding an orbital-dependent term to the GGA energy functional, thus imposing a penalty on orbital hybridization.

We employ the following GGA + molecular U energy functional:

$$E_{GGA+U} = E_{GGA} + \frac{U_{2\pi^*}}{2} \sum_{\sigma} \text{Tr}\{\mathbf{f}_{2\pi^*,\sigma}(\mathbf{I} - \mathbf{f}_{2\pi^*,\sigma})\} + \frac{U_{5\sigma}}{2} \sum_{\sigma} f_{5\sigma,\sigma}(1 - f_{5\sigma,\sigma}),$$

where $f_{5\sigma,\sigma}$ is the occupation of the 5σ orbital of spin σ and $\mathbf{f}_{2\pi^*,\sigma}$ is the occupation matrix associated with the $2\pi_x^*$ and $2\pi_y^*$ orbitals of spin σ. The parameters $U_{2\pi^*}$ and $U_{5\sigma}$ penalize noninteger occupations of the $2\pi^*$ and 5σ orbitals: $U_{2\pi^*}$ reduces $2\pi^*$ backdonation while $U_{5\sigma}$ reduces 5σ donation, as illustrated in Figure 5-4. The parameters $U_{2\pi^*}$ and $U_{5\sigma}$ can also be interpreted as shifting the effective single-electron energies. Heuristically, U_χ modifies the single-electron energy ϵ_χ by an amount $U_\chi(1/2 - f_\chi)$. Thus, $U_{2\pi^*}$ increases the $2\pi^*$ energies, whereas $U_{5\sigma}$ decreases the 5σ energy, causing the HOMO-LUMO gap to increase.

The present functional differs slightly from that introduced by Kresse, Gil, and Sautet. The GGA + molecular U energy in Eq. 5.2, whose expression is based on the matrix formulation introduced by Cococcioni and de Gironcoli [29], is invariant with respect to the choice of the x- and y-axes. In other words, an arbitrary rotation of the molecular orbitals does not affect the GGA + molecular U energy. Additionally, the functional allows the freedom to vary both the amount of electron backdonation and that of electron donation. The necessity of simultaneously varying backdonation and donation will be discussed later.

Although a molecular U term is admittedly a simplified energy correction, it reproduces
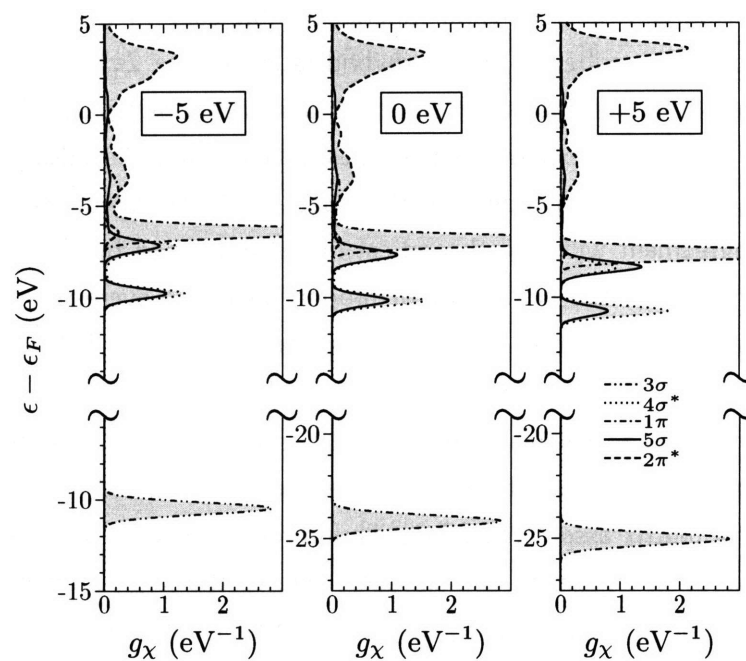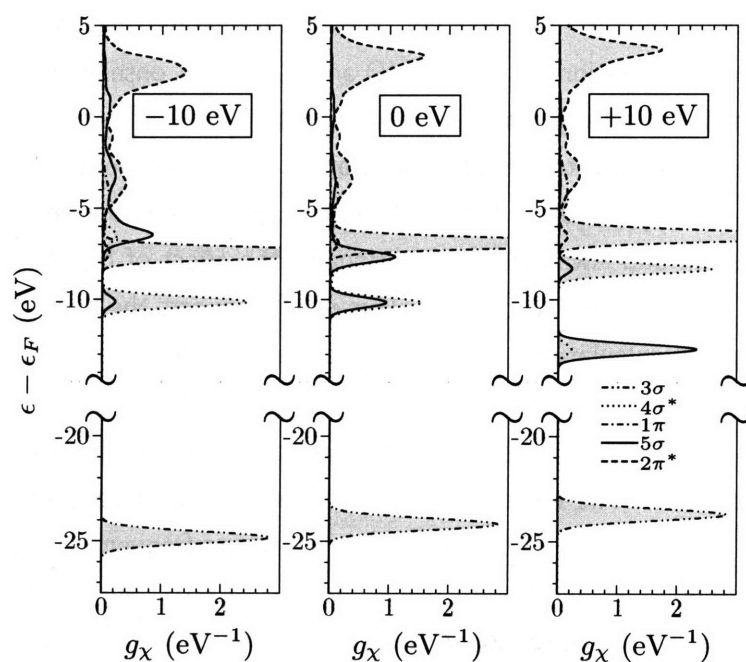
(a) Atop DOS vs. $U_{2\pi^*}$

(b) Atop DOS vs. $U_{5\sigma}$

Figure 5-4: Density of states projected on the CO molecular orbitals as a function of $U_{2\pi^*}$ and $U_{5\sigma}$ controlling the hybridization of the LUMO and HOMO orbitals for atop adsorption of CO on Pt(111).

the essential features of the energetics of CO adsorption [102]. The cluster calculations of Gil et al., based on the B3LYP hybrid functional [18], confirm that the inaccuracy of the GGA energies can be ascribed to an overhybridization of the $2\pi^*$ molecular orbitals [125]. This conclusion is supported by the recent periodic-slab B3LYP calculations of Neef and Doll [106, 107]. Moreover, experimental studies indicate that the adsorption energy of CO on platinum shows a linear dependence with respect to the energy of the center of the metal d bands,35 in agreement with the theoretical model developed by Hammer, Morikawa and Nørskov [93]. However, the coefficient of proportionality is overestimated within density-functional calculations, indicating that the interaction between the $2\pi^*$ orbitals and the metal d bands is excessive.

We thus proceeded to calculate the energetic, structural, and vibrational properties for CO adsorbed on platinum. Stretching frequencies are now obtained by diagonalizing the two-by-two dynamical matrix associated off-equilibrium displacements of the carbon and oxygen atoms in the direction normal to the surface. Due to the large atomic mass of platinum, the resulting stretching frequencies deviate by less than 1 cm^{-1} from the full DFPT phonon frequencies.

The results of the calculations are presented in Figure 5-5, and in Appendix F, along with methodological details. As expected, adsorption energies decrease with increasing penalization on the hybridizations of the HOMO and LUMOs. Consequently, both donation and backdonation favor CO adsorption, in agreement with Ref. [102]. Moreover, we observe that electron backdonation tends to decrease the relative adsorption energy $E_{ads}(atop) - E_{ads}(fcc)$, confirming that $2\pi^*$ backdonation favors CO adsorption at high-coordination sites, as demonstrated by Anderson and Awad [126]. Additionally, the effect of $U_{5\sigma}$ on the relative binding energy is much weaker than that of $U_{2\pi^*}$. This result supports the hypothesis that the failure of density-functional calculations in predicting the most stable adsorption site is principally related to an overestimation of $2\pi^*$ backdonation [100–102].

Considering now the structural and vibrational properties, we observe more complex $U_{2\pi^*}$- and $U_{5\sigma}$-dependencies. The effect of electron donation must clearly be taken into account when analyzing the sensitivity of the calculated stretching frequencies. Note that the invariance of the stretching frequency with respect to $U_{2\pi^*}$ for CO adsorbed at the atop site, as already observed in Ref. [100] for copper surfaces, can be explained by the fact that the $U_{2\pi^*}$-axis is tangent to the contour line $\nu(C-O) = 2050$ cm^{-1}. Despite this fact, the dependence of $\nu(C-O)(atop)$ with respect to $U_{5\sigma}$ is appreciable, supporting the idea that $2\pi^*$ backdonation alone does not control the site-dependence of the C–O stretching frequency.

(a) $E_{\text{ads}}(\text{atop}) - E_{\text{ads}}(\text{fcc})$ (eV)

(b) $E_{\text{ads}}(\text{atop})$ (eV)

(c) $E_{\text{ads}}(\text{fcc})$ (eV)

(d) $\nu(\text{C–O})(\text{atop})$ (cm^{-1})
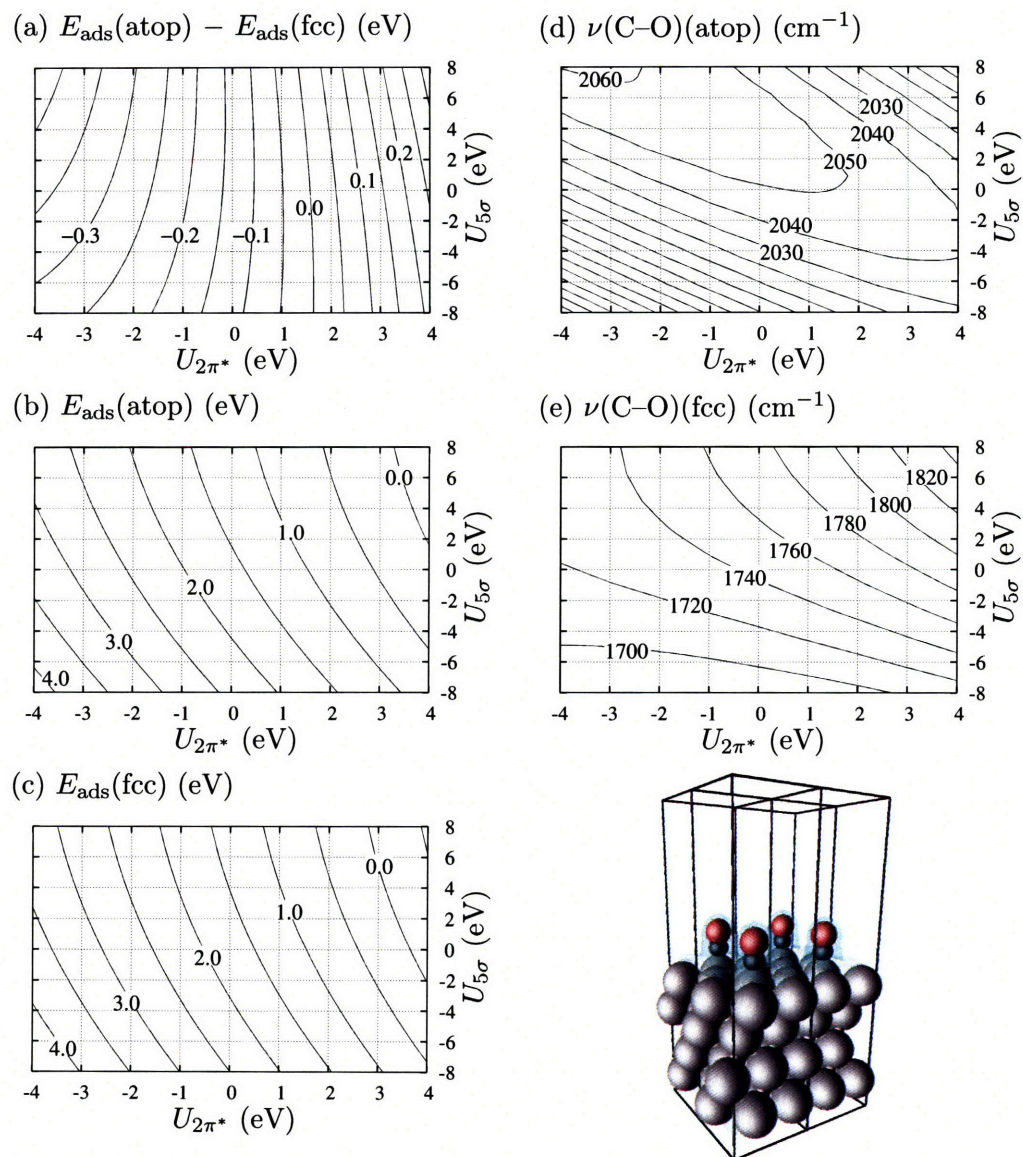
(e) $\nu(\text{C–O})(\text{fcc})$ (cm^{-1})

Figure 5-5: Adsorption energy and intramolecular stretching frequency as a function of $U_{2\pi^*}$ and $U_{5\sigma}$ controlling the hybridization of the LUMO and HOMO orbitals for atop and fcc adsorption of CO on Pt(111).

Figure 5-6: Ranges of variation (indicated by black error bars) of the adsorption energy, bond length, and stretching frequency of CO on Pt(111) for a very broad range of hybridizations (0 eV $< U_{2\pi^*} < 5$ eV and -10 eV $< U_{5\sigma} < 10$ eV).
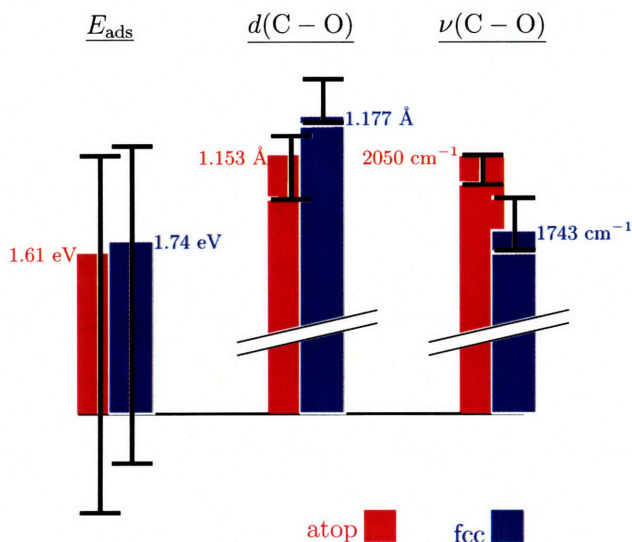
To conclude this section, we report the results of our sensitivity analysis (Figure 5-6). Large ranges for $U_{2\pi^*}$ and $U_{5\sigma}$ are selected: 0 eV $< U_{2\pi^*} < 5$ ev and -10 eV $< U_{5\sigma} < 10$ eV. Note that the parameter $U_{2\pi^*}$ is kept positive since the GGA + molecular U calculations clearly indicate that $2\pi^*$ backdonation is overestimated. We emphasize that these energy ranges correspond to large shifts in the single-electron energies (up to $\Delta\epsilon_{2\pi^*} = 1$ eV and $|\Delta\epsilon_{5\sigma}| = 4$ eV) and to large variations of the adsorption energies (up to $|\Delta E_{ads}| = 1.5$ eV). Thus, the relative variations of the adsorption energies are comparable to their absolute values. Despite these sizable variations of the adsorption energies, we observe little variations of the bond lengths and stretching frequencies:

$$\begin{cases} 1.127 \text{ Å} & < & d(\text{C}-\text{O})(\text{atop}) & < & 1.165 \text{ Å} \\ 1.173 \text{ Å} & < & d(\text{C}-\text{O})(\text{fcc}) & < & 1.199 \text{ Å} \\ 1933 \text{ cm}^{-1} & < & \nu(\text{C}-\text{O})(\text{atop}) & < & 2055 \text{ cm}^{-1} \\ 1666 \text{ cm}^{-1} & < & \nu(\text{C}-\text{O})(\text{fcc}) & < & 1878 \text{ cm}^{-1} \end{cases} \qquad (5.2)$$

These small variations account for the remarkable accuracy of the bond lengths and stretching frequencies calculated within PBE-GGA. In particular, they justify the correct ordering of the C–O stretching frequencies despite important qualitative errors in predicting the relative CO adsorption energies. These results provide strong support to the conclusion of

the preceding section: the variations of d(C–O) and ν(C–O) are not directly due to electron donation and backdonation, but rather to the hybridization of the 1π orbitals.

5.5   Conclusion

This study has evidenced that the PBE-GGA predictions for the stretching frequencies of CO adsorbed on platinum are in excellent agreement with SFG experiments despite the well-known failure of local and generalized-gradient calculations in predicting the most stable adsorption site. Similar agreement is obtained for CO adsorbed on platinum-ruthenium bimetallic surfaces, allowing the direct recognition of CO adsorption sites.

Our orbital-resolved force analysis has demonstrated that the variations of bond length and stretching frequency as a function of the CO adsorption site are principally due to the 1π hybridization, rather than the $2\pi^*$ and 5σ hybridizations. Using the GGA + molecular U approach, we have performed a sensitivity analysis to quantify the influence of the $2\pi^*$ and 5σ hybridizations on the structural and vibrational properties for CO on platinum. The effect of $2\pi^*$ backdonation has been shown to be small and comparable to that of 5σ donation, contradicting the widespread idea that backdonation controls the frequency shifts.

These results explain the remarkable accuracy of the PBE-GGA frequency predictions despite errors in the hybridizations of the $2\pi^*$ and 5σ orbitals. Furthermore, they suggest a promising way to connect density-functional calculations with experiments in some of the most problematic cases of molecular adsorption on transition metals.

Vibrational Stark Effect for Carbon Monoxide on Platinum-Ruthenium Surfaces

6.1 Introduction

IN RECENT DECADES, A WIDE RANGE of *in-situ* techniques for the microscopic characterization of electrode-electrolyte interfaces have been developed. Notably, vibrational spectroscopy has delivered unique insight into the structure and catalytic activity of electrochemical surfaces under operating conditions. These accurate spectroscopic measurements are now frequently analyzed in light of increasingly predictive first-principles models, thereby providing a detailed chemical interpretation of experimental observations.

Among the systems recurrently studied in electrochemical spectroscopy, CO adsorbed on transition metal surfaces has attracted considerable attention. It is revealing to note that the theoretical interpretation for the site dependence of the C–O stretching frequency was at the origin of Blyholder's *electron donation model*. This model and its extensions [93] are widely employed to this day in the description of adsorbate-substrate interactions and in the elucidation of catalytic trends.

Notwithstanding the remarkable performance of density-functional theory calculations in predicting the site-dependent C–O red shifts, the vibrational response of CO as a function of the applied electrode voltage (the vibrational Stark effect) is still not completely understood. First-principles simulations have primarily focused on the influence of an externally applied electric field on the vibrational properties of adsorbed CO [127–129]. A notable exception to this trend is the recent study of Lozovoi and Alavi who considered the local influence of an

excess surface charge [81].

In this work, we propose a computational scheme that extends the approach of Lozovoi and Alavi by relating the surface charge to the difference of voltage across the electrical double layer. The model relies on the DIL model presented in Chap. 4. The outline of this study is as follows. First, we provide an overview of existing density-functional theory models for calculating the electrode-potential dependence of adsorbate frequencies. Second, we present density-functional theory predictions for the vibrational Stark shifts of CO adsorbed on clean and ruthenium-covered platinum surfaces. The last section provides an electrochemical interpretation of the results.

6.2 First-principles Vibrational Stark Effect Studies for CO on Transition Metals

Following a series of important theoretical contributions from Ray and Anderson [130], Holloway and Nørskov [131], and Korzeniewski et al. [132], the Hartree-Fock cluster simulations of Bagus et al. [133] constitute one of the first ab-initio studies of adsorbate vibrational Stark shifts for CO on transition metal surfaces. From their first-principles calculations, Bagus et al. concluded that the vibrational Stark shifts predominantly originate from the electrostatic interaction between the adsorbate dipole and the applied field. Chemical effects were indeed found to have little direct bearing on the predicted tuning rates [133,133,134]. The assertion of Bagus et al. was reexamined in subsequent first-principles studies, which concluded that electric and chemical contributions are in fact inseparable [135,136].

A systematic assessment of the reliability of density-functional theory cluster models was undertaken by García-Hernández et al. [127]. For neutral adsorbates, the study demonstrated the relatively good convergence of the calculated Stark shifts as a function of the size of the cluster. Using hybrid density-functional theory, the field-dependent Stark tuning slope $d\nu(\text{C–O})/dF$ for atop adsorption of CO on a 13-atom platinum cluster was predicted to be 104 cm^{-1}·Å/V.

These results were first confirmed by the generalized-gradient density-functional theory study of Koper et al. [128], in which values of 102 and 125 cm^{-1}·Å/V were reported for CO adsorbed at the atop and hollow adsorption sites on a Pt_{13} cluster, respectively. Subsequently, using a refined generalized-gradient cluster model [129], Wasileski, Koper, and Weaver calculated the field-dependent Stark slopes to be 120 and 130 cm^{-1}·Å/V at the atop and hollow

sites, respectively [137]. Wasileski *et al.* ascribed the large discrepancy between UHV and electrochemical measurements to the electrostatic contribution from the ionic solvent. (This disagreement will be discussed further in Sec. 6.4.

In a recent periodic-slab study, Lozovoi and Alavi calculated the Stark tuning slope by adding a fractional amount of charge to the system, thereby generating an electric field at the surface of the metal [81]. In order to compensate the excess surface charge, a thin layer of static charges was inserted between the periodically repeated slabs [51]. Using this approach, the frequency-field slope was calculated to be 45.2 $cm^{-1} \cdot Å/V$ at a coverage of 1/4 of the monolayer (in the 2 × 2 adsorption structure) for CO at the atop site on Pt(111). This result is in good agreement with the value $d\nu(C-O)/dF = 56$ $cm^{-1} \cdot Å/V$ obtained from UHV measurements [138]. A double-layer model that completes the approach of Lozovoi and Alavi is presented below.

6.3 Stark-shift Predictions for CO on Platinum and Platinum-Ruthenium Surfaces

6.3.1 The Electrode Charge as Fundamental Parameter

Before presenting predictions for the C–O Stark shifts on clean and ruthenium-covered platinum surfaces, we underscore that at variance with experiments in which one typically controls intensive thermodynamic variables (*e.g.*, the pressure P applied to the system), one generally work with fixed extensive variables (*e.g.*, the volume V of the system) when performing first-principles calculations.

Therefore, the approach that we adopted here consists of controlling the electrical conditions—that is, the electric field for ultra-high-vacuum experiments, and the electrode voltage for electrochemical measurements—by varying the corresponding extensive quantity, namely, the charge of the system. As mentioned in the previous section, a similar methodology was employed by Lozovoi and Alavi [81] in the case of electrified metal-vacuum interfaces.

6.3.2 Vibrational Stark Effect under Ultra-high-vacuum Conditions

In this study, we adopt a periodic-slab model to determine the field-dependent Stark tuning slope $d\nu(C-O)/dF$ for CO adsorbed on clean and ruthenium-covered platinum surfaces. In order to eliminate periodic-image errors arising from the use of periodic boundary conditions,
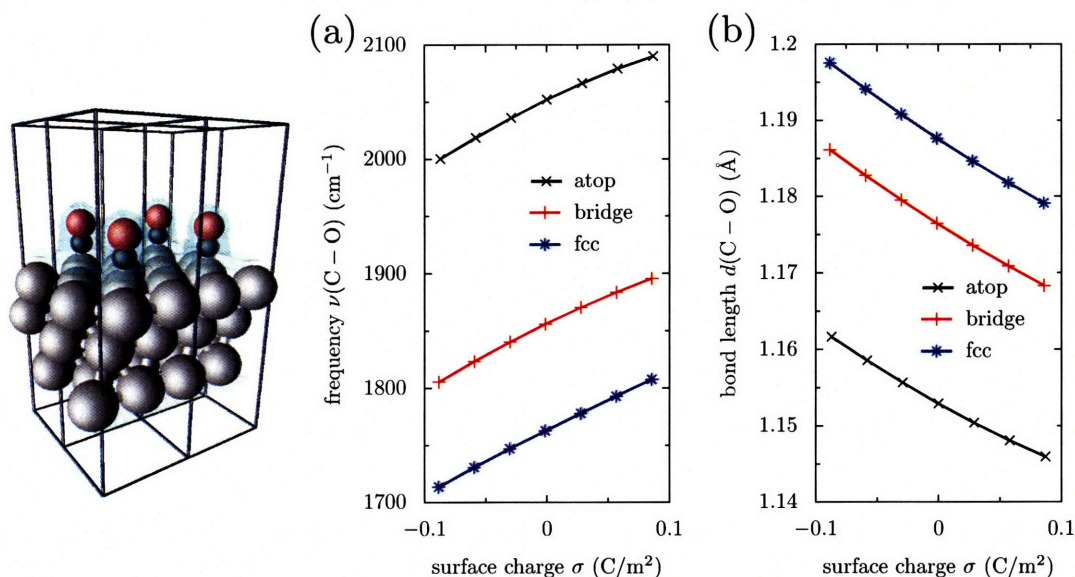
Figure 6-1: (a) Intramolecular stretching frequency ν(C–O), and (b) intramolecular bond length d(C–O) for CO adsorbed at the atop, bridge, and fcc sites on Pt(111).

site	slab	$\frac{d}{d\sigma}\nu(\text{C–O})$ (cm^{-1}·m^2/C)	$\frac{d}{dF}\nu(\text{C–O})$ (cm^{-1}·Å/V)	$\frac{d}{dq}d(\text{C–O})$ (Å·m^2/C)	$\frac{d}{dF}d(\text{C–O})$ (Å^2/V)
atop	3 ML Pt	519	45.9 (UHV Exp, 56)[1] (DFT, 45.2)[2]	−0.091	−8.05 · 10^{-3}
bridge	3 ML Pt	517	45.8	−0.102	−9.03 · 10^{-3}
fcc	3 ML Pt	531	47.0	−0.106	−9.38 · 10^{-3}
atop	4 ML Pt	519	45.9	−0.093	−8.23 · 10^{-3}
atop	1 ML Ru/3 ML Pt	572	50.6	−0.108	−9.56 · 10^{-3}

[1]Ref. [138]. [2]Ref. [81] (1/4 ML, periodic slab, PBE generalized-gradient approximation).

Table 6.1: Field-dependent and charge-dependent slopes of the intramolecular stretching frequency ν(C–O) and bond length d(C–O) at the point of zero charge for CO adsorbed on clean and ruthenium-covered Pt(111) surfaces.

we employ the density-countercharge (DCC) correction (cf. Chap. 3). As extensively discussed in Chap. 3, applying this approach to charged systems with two-dimensional periodicity amounts to introducing a parabolic correction to the electrostatic potential.

The metal surface is modeled using three- and four-layer-thick slabs. Each layer contains four atoms per supercell. The structure of the CO adlayer is $\sqrt{3} \times 2$ corresponding to a coverage of 1/4 ML. We employ the generalized-gradient Perdew-Burke-Ernzerhof (PBE-GGA) [16] functional as an approximation to the exchange-correlation energy. We use ultrasoft pseudopotentials [21] for the ionic cores. The Brillouin zone is sampled with a shifted $3 \times 3 \times 1$ mesh and cold-smearing occupations [12] (smearing temperature of 0.03 Ry). The wavefunction and charge-density energy cutoffs are 25 and 200 Ry, respectively. The PBE-GGA lattice parameter for platinum is calculated to be 3.993 Å. For this elongated system, the DCC correction is calculated within the planar-average approximation (cf. Chap. 3). The intramolecular stretching frequencies are obtained via frozen-phonon calculations—$i.e.$, by diagonalizing the dynamical matrix associated with off-equilibrium normal displacements of the carbon and oxygen atoms. It was verified that this frozen-phonon approach yields stretching frequencies within 2% of their full-phonon counterparts (cf. Chap 5).

The surface-charge dependence of the CO structural and vibrational properties are presented in Figure 6-1 and in Table 6.1. In order to facilitate comparisons with previous studies, we also report the results in terms of field-dependent Stark tuning slopes. Note that a surface charge of $\sigma = 1$ C/m^2 corresponds to an electric field of $F = 4\pi\sigma = 11.29$ V/Å (the relation between surface charge and surface electric field will be examined further in the Sec. 6.4). First, we observe that augmenting the surface charge tends to increase the C–O stretching frequency and to decrease the C–O bond length. In addition, the stretching-frequency and bond-length variations tend to become less marked as the surface charge increases, in agreement with previous studies [81,129,139]. The field-dependent frequency slope is calculated to be 45.9 cm^{-1}·Å/V for CO adsorbed at the atop site on Pt(111), in very close accordance with the value $d\nu$(C–O)$/dF = 45.2$ cm^{-1}·Å/V reported by Lozovoi and Alavi [81]. We also note that the Stark slope does not vary when increasing the slab thickness from three to four monolayers. As already alluded to, the periodic-slab field-dependent slopes are significantly lower than those obtained from cluster calculations (ranging from 100 to 120 cm^{-1}·Å/V [127–129]) and are found to be in good agreement with the UHV experimental value 56 cm^{-1}·Å/V [138]. The field-dependent slopes at the bridge and fcc sites on clean platinum surfaces are calculated to be 45.8 and 47.0 cm^{-1}·Å/V, respectively. The UHV Stark tuning rates for CO on Pt(111) are thus only moderately affected by site coordination. For CO adsorbed at the atop

Figure 6-2: Electrode-potential dependence of the intramolecular stretching frequency for CO adsorbed at the atop site on Pt(111). The concentration of the diffuse ionic solution is $c_d = 0.1$ M.

site on Pt(111) covered with 1 ML of ruthenium, the frequency-field slope is calculated to be $d\nu(\text{C–O})/dF = 50.6$ cm$^{-1}\cdot$Å/V, corresponding to a notable increase in the Stark tuning rate of about 10%, in qualitative agreement with the cluster calculations reported in Ref. [128]. As a final note, it should be mentioned that the field dependence of the C–O bond length is only roughly correlated to that of C–O the stretching frequency with a proportionality factor of approximately -5300 cm^{-1}/Å. Note that this factor is significantly lower in absolute value than the stretching frequency vs. bond length correlation slopes typically measured for CO on neutral transition metal surfaces—ranging from -7000 to -8000 cm^{-1}/Å (cf. Refs [122] and [129], and Fig. 5-3).

6.3.3 Vibrational Stark Effect under Electrochemical Conditions

We now consider the electrical response of CO-covered Pt(111) interface under electrochemical conditions. The electrode potential corresponding to a given surface charge is determined
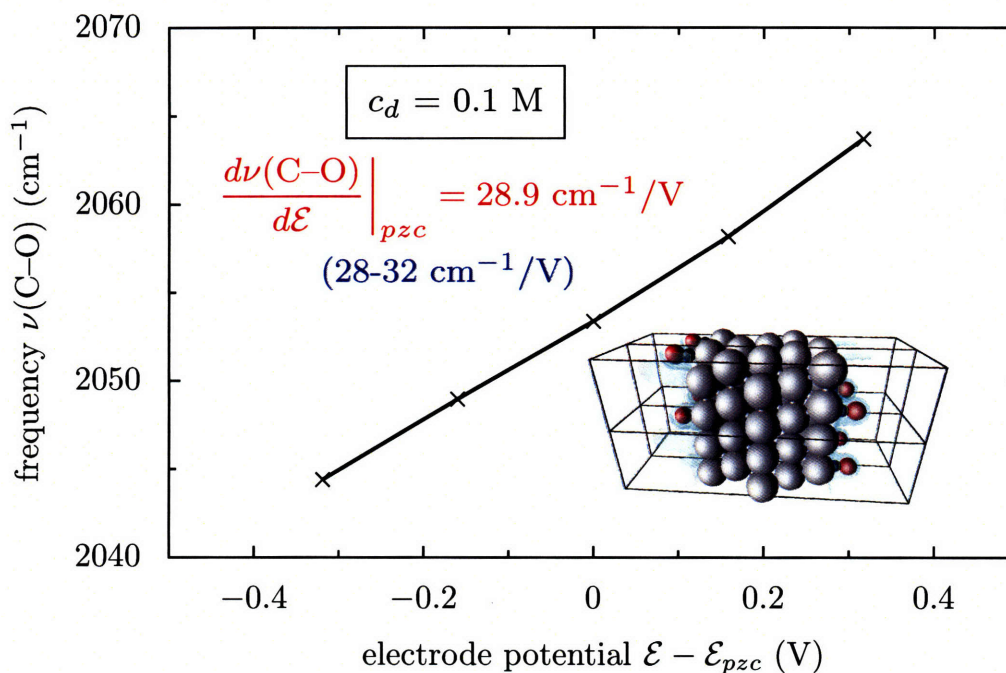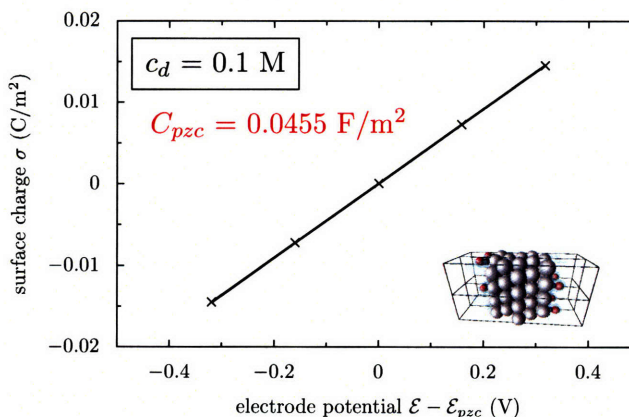
Figure 6-3: Electrode-potential dependence of the surface charge for CO adsorbed at the atop site on Pt(111). The concentration of the diffuse ionic solution is $c_d = 0.1$ M.

from the profile of the electrostatic potential across the charged metal-solution interface. (As explained in Chap. 4, the electrostatic potential is calculated as the difference between the electrostatic energy in the bulk of the solvent and the Fermi energy of the metal.) The double-layer electrostatic profile is computed using the solvation model introduced by Fattebert and Gygi [58] and the diffuse-ionic-layer (DIL) algorithm presented in Chap. 4.

The system is modeled using a symmetric five-layer-thick Pt(111) slab (ABCBA layer stacking) with CO covering each lateral face in the $\sqrt{3} \times 2$ adsorption structure. Similarly to the UHV calculations above, we employ the PBE-GGA functional, ultrasoft pseudopotentials, and plane-wave cutoffs of 25 and 200 Ry. The Brillouin zone is sampled using a $4 \times 4 \times 1$ mesh with cold-smearing occupations. For the solvation model, the dielectric constant of the aqueous solvent is set to $\epsilon_S = 78$. In calculating the density-dependent dielectric constant ϵ, the charge density is smeared in the directions parallel to the surface (Gaussian spread of 5 bohr) in order to eliminate penetration of the implicit solvent into the adlayer. The charge-density cutoff delimiting the solvation shell ρ_0, and the smoothness exponent controlling the magnitude of the solvent dipole are set to 0.0005 bohr^{-3} and 1.25, respectively. These solvation parameters are close to those used in previous studies [58, 59]. The charge-density cutoff defining the depth of the ionic penetration was selected to be $\rho_1 = 0.0001$ bohr^{-3}. As discussed in Sec. 6.4, value of the ionic cutoff yields a double-layer thickness in agreement with experimental measurements.

The dependence of the C–O stretching frequency as a function of the electrode potential is depicted in Fig. 6-2. The vibrational Stark tuning rate is predicted to be $\gamma(\text{C–O}) = 28.9$ cm^{-1} at the potential of zero, in excellent agreement with the SFG Stark tuning rate of 28 cm^{-1} (0.1 M H$_2$SO$_4$) [4]. This calculation constitutes the first accurate prediction of the

C–O vibrational Stark tuning rate using a comprehensive first-principles model.

Additionally, the charge-potential response for a CO-covered platinum surface in contact with an ionic solution of concentration $c_d = 0.1$ M is presented in Figure 6-3. At this relatively high ionic concentration, the electrical response of the system is observed to be closely linear, reflecting the rapid decay of the electric field in the ionic layer. From these results, the differential capacitance of the surface is calculated to be $C = 0.0455$ F/m^2 at the point of zero charge. Consequently, the frequency-charge slope is calculated to be 635 cm^{-1}·m^2/C, which is close to UHV value of 519 cm^{-1}·m^2/C. The agreement between the predicted Stark slopes in vacuum and under electrochemical conditions is rather surprising due to long-standing discrepancies between UHV and in-situ experiments [81, 128, 129, 137, 138]. This concordance is discussed further in the next section.

6.4 Electrochemical Origin of the Vibrational Stark Effect

In order to elucidate the accuracy of the Stark shift predictions, we first analyze the electrostatic-potential profile of a positively charged CO-covered platinum surface immersed in an ionic solution (Figures 6-4). Using the same notation as those in Chaps. 3 and 4, v denotes the electrostatic potential of the system, v' stands for the potential of the periodically repeated system in vacuum, and the difference $v^{corr} = v - v'$ refers to the corrective potential corresponding to the electrostatic contributions from the excess surface charge and from the ionic solvent. First, we observe that the electrostatic correction v^{corr} is curved inside the slab and converges to a constant in the bulk of the solvent. In the transition region, a significant potential drop due to the response of the polarizable continuum occurs. As illustrated in Figure 6-5, the curvature of the corrective potential inside the metal slab is directly related to the surface charge, in agreement with the analytical study presented in Chap. 4. The parabolic behavior of the corrective potential inside the slab region is identical to that observed for charged surfaces in vacuum (cf. Chap. 3). The close similarity between the corrective potentials in UHV and electrochemical environments confirms the common electrostatic origin of the vibrational Stark shifts under UHV and electrochemical conditions.

We now analytypicall disagreement between UHV and electrochemical predictions by comparing the electrostatic profile of a charged platinum surface covered with CO (Figure 6-6a) with that obtained for a neutral surface v_{pzc}. The difference between v and v_{pzc} is plotted in
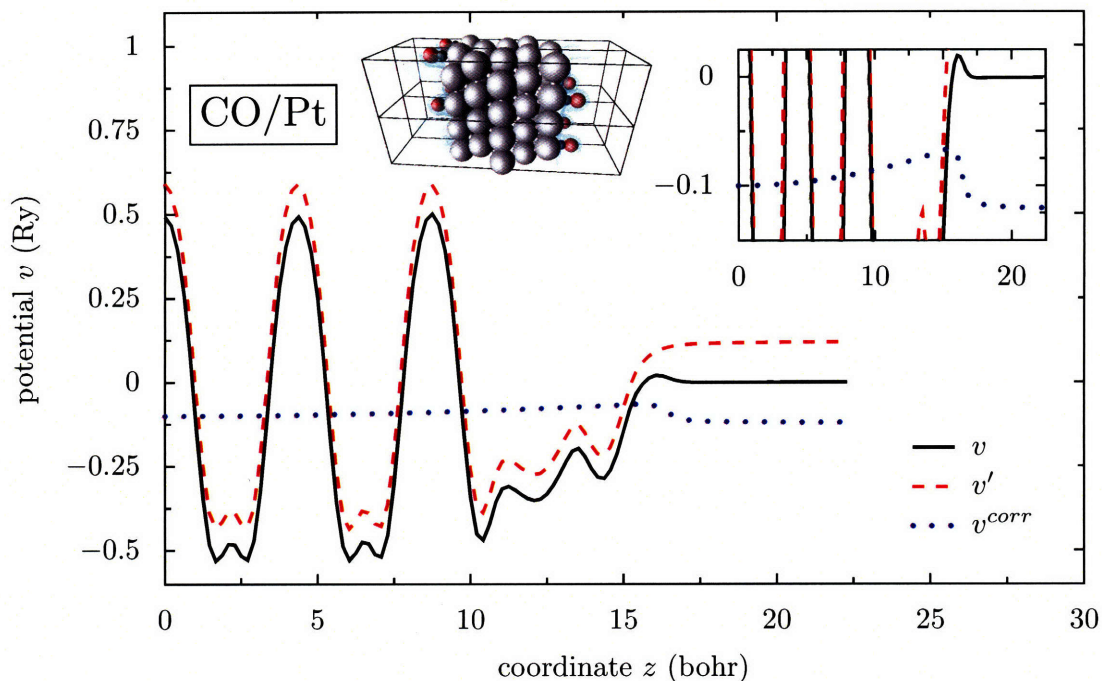
Figure 6-4: Electrostatic potential v, periodic potential v', and electrostatic correction v^{corr} averaged in the xy-plane parallel to the interface for CO adsorbed at the atop site on a charged Pt(111) surface in contact with a diffuse ionic solution. The charge of the surface is $\sigma = 0.014$ C/m² (corresponding to -0.05 e per supercell). The concentration of the diffuse ionic solution is $c_d = 0.1$ M.
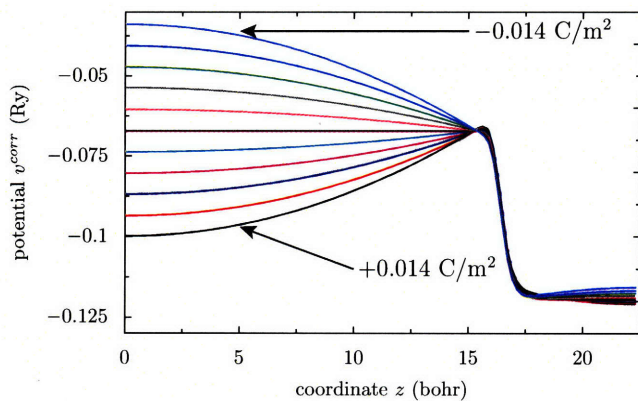
Figure 6-5: Electrostatic correction v^{corr} averaged in the xy-plane parallel to the interface for CO adsorbed at the atop site on a charged Pt(111) surface in contact with a diffuse ionic solution. The charge of the surface σ is varied from -0.014 C/m² to $+0.014$ C/m².
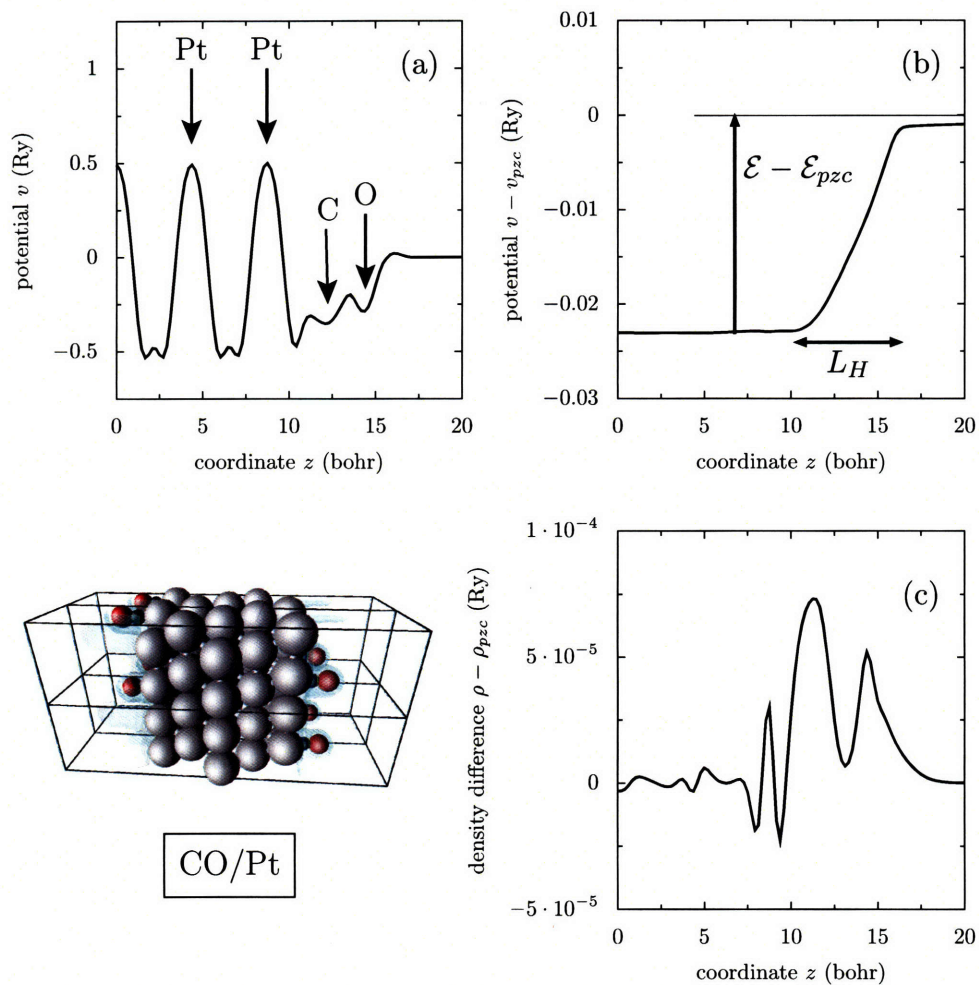
Figure 6-6: (a) Electrostatic potential v of a charged CO-covered platinum surface, (b) electrostatic-potential variation $v - v_{pzc}$ with respect to the point of zero charge, and (c) charge-density variation $\rho - \rho_{pzc}$ with respect to the point of zero charge for CO adsorbed at the atop site on a Pt(111) surface in contact with a diffuse ionic solution of concentration 0.1 M. Note that the contributions from the ionic solvent are not included in the charge-density profile.

Figure 6-6b. As expected intuitively, the excess surface charge induces an important shift in the electrostatic potential inside the metal slab. The magnitude of the shift corresponds to the difference between the electrode potential $\mathcal{E}$ and the potential of zero charge $\mathcal{E}_{pzc}$. This noteworthy feature constitutes a direct confirmation the model introduced by Nørskov et al., which consists of including the electrode voltage by shifting the energies of the metal electrons by a constant amount $\Delta\mathcal{E} = \mathcal{E} - \mathcal{E}_{pzc}$ [77]. In addition, we observe that the surface charge generates an electric field at the metal-solution interface. The size of the double-layer region L_H obtained with the selected value of the solvation parameter ρ_1 equals approximately 3 Å, in agreement with typical estimates of the double-layer thickness [75, 77, 129]. Nevertheless, it is fundamental to note that the electric field is not linear in the adlayer region, as evidenced by the presence of a significant amount of excess surface charge on the CO adsorbate (Figure 6-6c). This nonlinear behavior translates into a notable reduction in the intramolecular electric field $F_H = (\mathcal{E} - \mathcal{E}_{pzc})/L_H$ in comparison with the long-range electric field $F_{UHV} = -4\pi\sigma$ measured in UHV experiments. As a matter of comparison, for a charge of 0.014 C/m^2 corresponding to a bias of 0.31 V, the electric field F_H and F_{UHV} are evaluated to be 0.10 and 0.16 V/Å, respectively. This observation rationalizes the discrepancies between UHV and electrochemical Stark tuning measurements.

6.5 Conclusion

We have employed a periodic-slab model to study the vibrational Stark effect under UHV and electrochemical conditions. In both cases, the local surface electric field was modified by adding a given amount of surface charge and by applying adequate electrostatic corrections. At variance with cluster studies, the predicted Stark shifts are found to be in very good agreement with both UHV and electrochemical spectroscopic measurements.

By comparing the electrostatic-potential profiles of isolated and solvated electrified slabs, we have evidenced the common electrostatic origin of the surface-charge dependence of the adsorbate vibrational properties. In addition to offering a direct confirmation and extension of the model recently proposed by Nørskov et al. [77], our electrostatic-profile analysis clarifies the long-standing discrepancy between UHV and electrochemical vibrational Stark tuning measurements.

This study highlights the interest of the modified Poisson-Boltzmann DIL model for the microscopic elucidation of important electrochemical trends.

Concluding Remarks

THIS DISSERTATION FOCUSES on the development and validation of a comprehensive approach to study quantum mechanical systems under realistic electrochemical conditions.

The methodology consists of controlling the applied voltage by varying the electronic charge of the system. As a prelude to the simulation of electrified surfaces in ionic solvents, we have studied fundamental aspects of the electrostatics of polarized and charged systems in periodic boundary conditions. We have shown that the difference between the periodic potential, straightforwardly obtained from a Fourier transform, and the exact potential can be characterized analytically. In light of this observation, we have presented an efficient density-countercharge (DCC) scheme to describe charged species and electrified interfaces in vacuum. This periodic-image correction scheme owes its improved accuracy to the exact determination of the open boundary conditions characterizing the electrostatic problem.

We have then analyzed and incorporated the electrostatic contributions from the aqueous solvent and from the counterions, thereby reproducing realistic electrochemical conditions. The resulting diffuse-ionic-layer (DIL) model, which relies on a density-functional theory description of the interface region and on a modified Poisson-Boltzmann representation of the semi-infinite ionic solvent, allows the direct prediction of the electrical response of electrochemical interfaces. In the presentation of the DIL model, we have emphasized the importance of imposing adequate electrochemical boundary conditions to overcome length-scale limitations and properly relate the microscopic state of charge of the surface to the macroscopic difference of voltage across the double-layer interphase.

In implementing these novel computational approaches, particular effort has been devoted to overcoming inherent accuracy and efficiency limitations by simultaneously exploiting

highly optimized fast Fourier transform and multigrid algorithms. The DCC and DIL corrective schemes have been shown to constitute beneficial alternatives to existing computational methods. Summarizing, one of the central methodological conclusions of this study is as the following: the electrostatic description of electrochemical systems from first-principles computations requires adopting appropriate boundary conditions.

As a probe of the predictive performance of the DCC and DIL schemes, we have analyzed the vibrational properties of CO on clean and ruthenium-covered platinum surfaces. In the first stage of this analysis, we have highlighted the remarkable precision of generalized-gradient density-functional theory calculations in describing the adsorption-site dependence of the C–O stretching frequency, notwithstanding well-known qualitative errors in the predicted adsorption energies. The excellent accuracy of semilocal density-functional theory calculations in determining the vibrational properties of adsorbed CO has been rationalized by introducing an orbital-resolved analysis of the force density of states and by performing a sensitivity analysis to evaluate the influence of donation and backdonation on the calculated observables. The orbital-resolved force analysis has established that the site-dependence of the C–O frequency is mainly related to the hybridization of the low-lying 1π orbitals. The sensitivity analysis has demonstrated that the influence of backdonation is small and comparable to that of donation, contradicting the widespread idea that backdonation controls the frequency shifts.

Based on these results, we have studied the electrode-potential dependence of adsorbate vibrational properties—the vibrational Stark effect—for CO adsorbed on transition metals, a subject that has attracted considerable attention and for which fundamental questions persist. At variance with previous studies, the calculated vibrational Stark shifts, obtained from the DCC and DIL periodic-slab models, were found to be in very good agreement with both ultra-high-vacuum and electrochemical experiments. This simultaneous concordance is made more remarkable by the long-standing discrepancy between UHV and electrochemical measurements. By comparing the electrostatic-potential profiles of isolated and solvated electrified slabs, we have highlighted the common electrostatic origin of the vibrational Stark effect in vacuum and under operating conditions, and provided important indications as to the electrostatic origins of the discrepancy between UHV and electrochemical Stark shifts in terms of delocalization of excess surface charge onto the CO adlayer.

As related projects, we have implemented an ensemble density functional theory (eDFT) molecular-dynamics scheme for simulating metallic systems. Additionally, we have developed a parameter-free LDA + U$\alpha\beta$ method to efficiently eliminate self-interaction errors with the ultimate aim of correcting the propensity of density-functional theory calculations to overhy-

bridize electronic states—a tendency that ultimately translates into overestimated adsorption energies.

The present computational electrochemistry toolkit extends the applicability of density-functional theory in electrochemistry and open promising perspectives for the direct application of first-principles methods to guide the microstructural optimization of fuel cells and the development of efficient electrochemical convertors.

APPENDIX A

Madelung Constants and Gaussian Potentials

In this appendix, we determine the Madelung constants of periodic point charges immersed in a compensating jellium background in one, two, and three dimensions for lattices characterized by a single geometric parameter L. A compilation of high-precision values for these fundamental constants is generally not found in the literature.

These values are computed using the asymptotic expansion of the Madelung constant $\alpha_{\sigma/L}$ of an array of Gaussian charges of spread σ in a compensating jellium, which is defined as:

$$\alpha_{\sigma/L} = (v_\sigma(0) - v'_{\sigma,L}(0))L^{d-2}, \tag{A.1}$$

where d is the spatial dimension. To obtain the expansion of $\alpha_{\sigma/L}$ in the limit $\sigma/L \to 0$, we may write $v'_{\sigma,L}(0)$ as:

$$v'_{\sigma,L}(0) = \frac{L^2}{\Omega_d} w_d\left(\frac{\sigma^2}{L^2}\right), \tag{A.2}$$

$$w_d\left(\frac{\sigma^2}{L^2}\right) = \sum_{\mathbf{g}' \neq 0} \frac{4\pi}{g'^2} \exp\left(-\frac{g'^2}{4}\frac{\sigma^2}{L^2}\right), \tag{A.3}$$

where Ω_d is the volume of d-dimensional unit cell, and $\mathbf{g}' = L\mathbf{g}$ denotes the dimensionless wavevector. Differentiating w_d with respect to σ^2/L^2, we obtain:

$$
\begin{aligned}
\frac{dw_d}{d(\sigma^2/L^2)} &= -\pi \sum_{\mathbf{g}' \neq 0} \exp\left(-\frac{g'^2}{4}\frac{\sigma^2}{L^2}\right) \\
&= \pi - \pi \sum_{\mathbf{g}'} \exp\left(-\frac{g'^2}{4}\frac{\sigma^2}{L^2}\right).
\end{aligned}
\tag{A.4}
$$

Figure A-1: Convergence of the Madelung constant as a function of the geometric parameter L/σ for a cubic unit cell using the approximation given by Eq. A.6. Note the negligible contribution of the complementary-error-function term beyond $L/\sigma = 3$ and the improvement in convergence brought about by the term $\pi\sigma^2/L^2$.
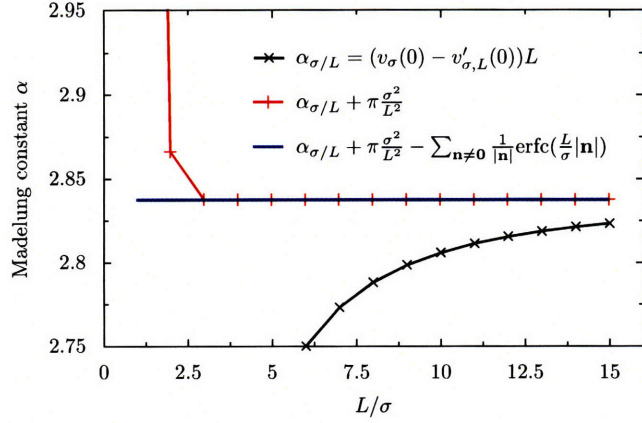
In the limit $\sigma/L \to 0$, this derivative becomes:

$$\frac{dw_d}{d(\sigma^2/L^2)} = \pi - \frac{\Omega_d}{\pi^{d-1}}\left(\frac{\sigma^2}{L^2}\right)^{-d/2}\int_{R^d} e^{-u^2}\,d\mathbf{u} + \dots \tag{A.5}$$

Integrating this expression, we obtain the asymptotic expansions of $v'_{\sigma,L}(0)$ and $\alpha_{\sigma/L}$ listed in Table A.1.

Hence, the Madelung constant α_0 can be calculated with high accuracy from the expansion of $\alpha_{\sigma/L}$. In the case of a cubic lattice of point charges, we obtain:

$$\begin{aligned}
\alpha_0 &\approx \alpha_{\sigma/L} + \frac{\pi\sigma^2}{L^2} - \sum_{\mathbf{n}\neq 0}\frac{1}{|\mathbf{n}|}\mathrm{erfc}(\frac{L}{\sigma}|\mathbf{n}|) \\
&\approx \frac{1}{L^2}\sum_{\mathbf{g}\neq 0}\frac{4\pi}{g^2}e^{-\sigma^2 g^2/4} - \frac{2L}{\sqrt{\pi}\sigma} + \frac{\pi\sigma^2}{L^2} - \sum_{\mathbf{n}\neq 0}\frac{1}{|\mathbf{n}|}\mathrm{erfc}(\frac{L}{\sigma}|\mathbf{n}|)
\end{aligned} \tag{A.6}$$

where $\mathbf{n} = (i, j, k)$ denotes an integer vector. Figure A-1 illustrates the rapid convergence of the Madelung constant calculated from Eq. A.6 for a cubic cell. This expression converges noticeably faster than the expression frequently found in the literature:

$$\alpha_0 \approx \frac{1}{L^2}\sum_{\mathbf{g}\neq 0}\frac{4\pi}{g^2}e^{-\sigma^2 g^2/4} - \frac{2L}{\sqrt{\pi}\sigma} - \sum_{\mathbf{n}\neq 0}\frac{1}{|\mathbf{n}|}\mathrm{erfc}(\frac{L}{\sigma}|\mathbf{n}|). \tag{A.7}$$

Although a similar procedure can be applied without additional difficulty for any dimensionality, we draw attention to the fact that in two dimensions, $\alpha_{\sigma/L}$ is not equal to the Madelung constant α in the limit $\sigma/L \to 0$, due to the logarithmic divergence of the potential. For a more complete discussion of the two-dimensional case, we refer the reader to the study of

3 D lattice	α_0	2 D lattice	α	1 D lattice	α_0
cubic	2.837 297 479	squared	2.621 065 852	linear	$-\pi/3$
body-centered	3.639 233 449	hexagonal	2.786 075 893		
face-centered	4.584 862 074				

$$v_\sigma(r) = \tfrac{1}{r}\mathrm{erf}(\tfrac{r}{\sigma})$$
$$v'_{\sigma,L}(r) = \tfrac{1}{V}\sum_{\mathbf{g}\neq 0}\tfrac{4\pi}{g^2}e^{-\sigma^2 g^2/4 + i\mathbf{g}\cdot\mathbf{r}}$$

$$v_\sigma(r) = -\ln(\tfrac{r^2}{\sigma^2}) + \mathrm{Ei}(-\tfrac{r^2}{\sigma^2})$$
$$v'_{\sigma,L}(r) = \tfrac{1}{S}\sum_{\mathbf{g}\neq 0}\tfrac{4\pi}{g^2}e^{-\sigma^2 g^2/4 + i\mathbf{g}\cdot\mathbf{r}}$$

$$v_\sigma(z) = -2\pi(\mathrm{zerf}(\tfrac{z}{\sigma}) + \tfrac{\sigma}{\sqrt{\pi}}e^{-\frac{z^2}{\sigma^2}})$$
$$v'_{\sigma,L}(z) = \tfrac{1}{L}\sum_{g\neq 0}\tfrac{4\pi}{g^2}e^{-\sigma^2 g^2/4 + ig\cdot z}$$

$$v_\sigma(0) = \tfrac{2}{\sqrt{\pi}\sigma}$$
$$v'_{\sigma,L}(0) = \tfrac{2}{\sqrt{\pi}\sigma} - \tfrac{\alpha_0}{L} + \tfrac{\pi\sigma^2}{L^3} + ...$$
$$\alpha_{\sigma/L} = \alpha_0 - \tfrac{\pi\sigma^2}{L^2} + ...$$

$$v_\sigma(0) = \gamma$$
$$v'_{\sigma,L}(0) = \ln(\tfrac{L^2}{\sigma^2}) - \alpha + \gamma + \tfrac{\pi\sigma^2}{L^2} + ...$$
$$\alpha_{\sigma/L} = -\ln(\tfrac{L^2}{\sigma^2}) + \alpha - \tfrac{\pi\sigma^2}{L^2} + ...$$

$$v_\sigma(0) = -2\sqrt{\pi}\sigma$$
$$v'_{\sigma,L}(0) = -L\alpha_0 - 2\sqrt{\pi}\sigma + \tfrac{\pi\sigma^2}{L} + ...$$
$$\alpha_{\sigma/L}(0) = \alpha_0 - \tfrac{\pi\sigma^2}{L} + ...$$

Table A.1: Madelung constants in one, two, and three dimensions computed using the procedure described in Appendix A, along with the quantities used in the calculation. Ei denotes the exponential integral and $\gamma = 0.577\ 215\ 665$ is the Euler constant.

Cichocki and Felderhof [55]. As a final remark, we note that the one-dimensional Madelung constant can be determined analytically from the relation:

$$\sum_{n=1}^{+\infty} \frac{1}{n^2} = \zeta(2) = \frac{\pi^2}{6}, \tag{A.8}$$

where ζ stands for the Riemann zeta function.

B

APPENDIX

Multipole-expansion Method

The performance of the multipole-expansion adaptation of the DCC scheme—the multipole-countercharge (MCC) correction—for a pyridazine cation is compared to that of the PCC and GCC schemes in Figure B-1. The size of the calculation cell ranges from 12 to 19 bohr. The parameters used in these calculations are those detailed in Sec. 3.3.2. Note the good performance of the MCC approach, which improves the energy accuracy by almost one order of magnitude in comparison with the PCC and GCC schemes for cell sizes above 17 bohr.

Figure B-1: Accuracy of the total energy of a pyridazine cation as a function of computational time using the PCC, GCC, and MCC schemes for cell sizes in the range 12-19 bohr. The labels D (dipole) and Q (quadrupole) indicate the order of the multipole expansion. For each scheme the corrective potential is updated every five SCF iterations.

APPENDIX C
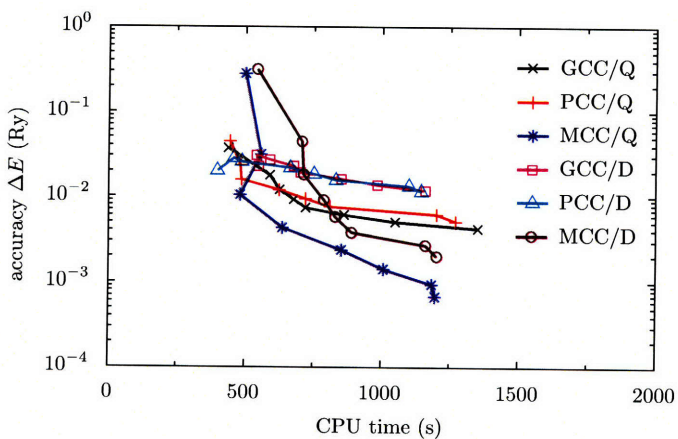
Details on the Pseudopotentials

The ultrasoft pseudopotentials were generated using Vanderbilts method [21] (for ruthenium), and the optimization scheme proposed by Rappe, Rabe, Kaxiras, and Joannopoulos [140] (for platinum, oxygen, and carbon). The parameters used for generating the pseudopotentials follow:

- Platinum

  The reference configuration for the platinum pseudopotential is [Xe] 4f14 5d9 6s1. The electronic states are obtained solving the scalar relativistic Kohn-Sham equations. The potential cutoff radius is $r_c = 2.4$ bohr. Pseudization is performed using two ultrasoft projectors for the s channel and one ultrasoft projector for the d channel. The all-electron wavefunctions are matched to their frozen-core counterparts at cutoff radii of 2.4 bohr and 1.8 bohr for the s and d states, respectively.

- Ruthenium

  The reference configuration for the ruthenium pseudopotential is [Kr] 4d7 5s1. The electronic states are obtained solving the scalar relativistic Kohn-Sham equations. The potential cutoff radius is $r_c = 2.4$ bohr. Pseudization is performed using two ultrasoft projectors for the s channel and two ultrasoft projectors for the d channel. The all-electron wavefunctions are matched to their frozen-core counterparts at cutoff radii of 2.4 bohr and 2.0 bohr for the s and d states, respectively.

- Oxygen

  The reference configuration for the oxygen pseudopotential is [He] 2s2 2p4. The electronic states are obtained solving the scalar relativistic Kohn-Sham equations. The

potential cutoff radius is $r_c = 1.6$ bohr. Pseudization is performed using two ultrasoft projectors for the s channel and two ultrasoft projectors for the p channel. The all-electron wavefunctions are matched to their frozen-core counterparts at a cutoff radius of 1.6 bohr.

- Carbon

  The reference configuration for the carbon pseudopotential is [He] 2s2 2p2. The electronic states are obtained solving the scalar relativistic Kohn-Sham equations. The potential cutoff radius is $r_c = 1.7$ bohr. Pseudization is performed using two ultrasoft projectors for the s channel and two ultrasoft projectors for the p channel. The all-electron wavefunctions are matched to their frozen-core counterparts at cutoff radii of 1.6 bohr and 1.7 bohr for the s and p states, respectively.

APPENDIX D

Ultrasoft Overlaps

The Vanderbilt ultrasoft formalism [21] consists of replacing the density operator $\hat{n}(\mathbf{r})$ with:

$$\hat{n}^{US}(\mathbf{r}) = \hat{n}(\mathbf{r}) + \sum_I \hat{n}_I(\mathbf{r}) \qquad (\text{D.1})$$

where $\hat{n}_I(\mathbf{r}; \mathbf{r}_1, \mathbf{r}_2) = \sum_{n,m} Q_{I,n,m}(\mathbf{r}) \beta^*_{I,n}(\mathbf{r}_1) \beta_{I,m}(\mathbf{r}_2)$ is the charge-augmentation contribution from the ionic core I. Correspondingly, the overlap operator $\hat{S}$ becomes:

$$\hat{S} = \hat{1} + \sum_I \hat{S}_I \qquad (\text{D.2})$$

where $\hat{S}_I(\mathbf{r}_1, \mathbf{r}_2) = \sum_{n,m} \int Q_{I,n,m}(\mathbf{r}) d\mathbf{r} \beta^*_{I,n}(\mathbf{r}_1) \beta_{I,m}(\mathbf{r}_2)$ is the ionic contribution to the overlap operator. The ultrasoft pseudopotential of the ionic core I is the sum of a local part $v_I^L(\mathbf{r})$ and a nonlocal part $\hat{v}_I^{NL}(\mathbf{r}_1, \mathbf{r}_2) = \sum_{n,m} D^0_{I,n,m} \beta^*_{I,n}(\mathbf{r}_1) \beta_{I,m}(\mathbf{r}_2)$.

This ultrasoft formalism considerably improves the convergence of density-functional algorithms with respect to the energy cutoffs applied to the plane-wave expansions of the wavefunctions and charge density. However, to calculate the overlap $\langle \chi | \hat{S} | \psi \rangle$ between the molecular orbital χ and the wavefunction ψ, it must be borne in mind that the overlap operators $\hat{S}_\chi$ and $\hat{S}_\psi$ corresponding to χ and ψ are distinct since the molecular orbital is calculated without the platinum slab. The procedure employed here consists in including fictitious platinum cores in the calculation of the molecular orbital. These fictitious cores are obtained by setting the local and nonlocal part of the platinum pseudopotential to zero, while keeping the contribution to the overlap operator unchanged. The resulting operator $\hat{S}_\chi^{fict}$ being identical to $\hat{S}_\psi$, the overlap coefficient can be calculated as $\langle \chi^{fict} | \hat{S}_\chi^{fict} | \psi \rangle = \langle \chi^{fict} | \hat{S}_\psi | \psi \rangle$ where χ^{fict}

is the molecular orbital calculated in the presence of the fictitious platinum cores. The primary advantage of this procedure is that it only requires changing the pseudopotentials.

APPENDIX E

Density-distribution Analysis

As an additional confirmation to the predominance of the 1π contribution in the C–O intramolecular force, we have calculated the density distribution and density-gradient distribution [121] projected on each CO molecular orbital χ. We define the projected density distribution as:

$$g_{1,\chi}(r_s) = \sum_i f_i |\langle \chi | \psi_i \rangle|^2 \int |\psi_i(\mathbf{r})|^2 \delta(r_s - r_s(\mathbf{r})) d\mathbf{r}, \tag{E.1}$$

where r_s is the Seitz radius. We propose a similar definition for the projected density-gradient distribution:

$$g_{3,\chi}(s) = \sum_i f_i |\langle \chi | \psi_i \rangle|^2 \int |\psi_i(\mathbf{r})|^2 \delta(s - s(\mathbf{r})) d\mathbf{r}, \tag{E.2}$$

where $s = |\nabla n|/2k_F n$ is the reduced density gradient. The derivatives of the distribution functions along the C–O stretching mode $\Delta^{(C-O)} g_{n,\chi} = d(C-O)\partial g_{n,\chi}/\partial d(C-O)$ (n=1,3) are plotted in Figure E-1.

Considering $\Delta^{(C-O)} g_{1,\chi}(r_s)$, we observe that increasing $d(C-O)$ tends to decrease the electronic charge in spatial regions of high electronic density. This trend is particularly marked for the 1π molecular orbitals, confirming their predominance in the intramolecular force. The predominant 1π contribution can also be seen in the $\Delta^{(C-O)} g_{3,\chi}(s)$ graph. It is important to note that the 1π orbitals result in a significant increase in charge-density homogeneity. According to the bond-expansion criterion derived by Zupan, Burke, Ernzerhof, and Perdew (Eq. 9 in Ref [121]), this observation confirms that the 1π orbitals are strongly bonding.

Figure E-1: Derivative of the density distribution function $\Delta^{(C-O)}g_{1,\chi}(r_s)$ and derivative of the density-gradient distribution function $\Delta^{(C-O)}g_{3,\chi}(s)$ along the C–O stretching mode for each molecular orbital χ.
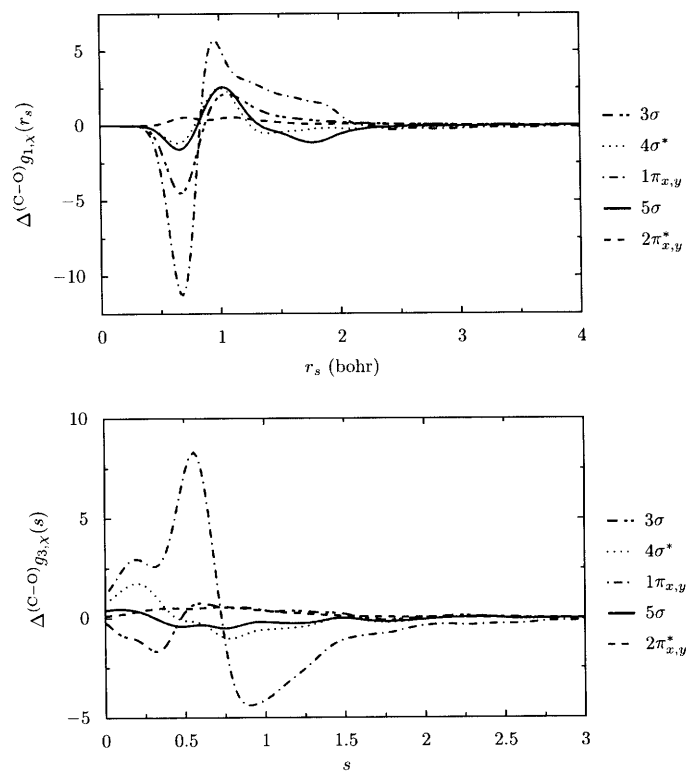
GGA + molecular U Force Density of States

The calculation of the FDOS within GGA + molecular U can be performed along the same general lines as the method presented in Chapter 5, the only modification being in the expression of the wavefunction contribution to the force $\mathbf{F}_{I,i\sigma}$. In the ultrasoft formalism and in the absence of molecular U contribution, the wavefunction contribution to the force can be written as [22,141]:

$$(\mathbf{F}_{I,i\sigma})_{GGA} = -f_{i\sigma}\langle\psi_{i\sigma}|\frac{\partial\hat{v}}{\partial\mathbf{R}_I} - \epsilon_{i\sigma}\frac{\partial\hat{S}}{\partial\mathbf{R}_I}|\psi_{i\sigma}\rangle. \tag{F.1}$$

Adding the molecular U term, the force contribution becomes:

$$
\begin{aligned}
(\mathbf{F}_{I,i\sigma})_{GGA+U} &= (\mathbf{F}_{I,i\sigma})_{GGA} - \frac{U_{2\pi^*}}{2}\sum_{\sigma}\text{Tr}\left\{(\mathbf{I} - 2\mathbf{f}_{2\pi^*,\sigma})\left.\frac{\partial\mathbf{f}_{2\pi^*,i\sigma})}{\partial\mathbf{R}_I}\right|_{\psi_{i\sigma}}\right\} \\
&\quad - \frac{U_{5\sigma}}{2}\sum_{\sigma}(1 - 2f_{5\sigma,\sigma})\left.\frac{\partial f_{5\sigma,i\sigma}}{\partial\mathbf{R}_I}\right|_{\psi_{i\sigma}}
\end{aligned} \tag{F.2}
$$

where $\mathbf{f}_{2\pi^*,i\sigma} = [f_{i\sigma}\langle\psi_{i\sigma}|\hat{S}|2\pi^*_\alpha\rangle\langle2\pi^*_\beta|\hat{S}|\psi_{i\sigma}\rangle]_{\alpha\beta}$ denotes the contribution from the wavefunction $\psi_{i\sigma}$ to the $2\pi^*$ occupation matrix $\mathbf{f}_{2\pi^*,\sigma}$ and $f_{5\sigma,i\sigma} = f_{i\sigma}\langle\psi_{i\sigma}|\hat{S}|5\sigma\rangle\langle5\sigma|\hat{S}|\psi_{i\sigma}\rangle$ is the contribution from $\psi_{i\sigma}$ to $f_{5\sigma,\sigma}$. Note that the derivatives must be calculated keeping $\psi_{i\sigma}$ fixed.

The main computational difficulty in determining the derivatives of the occupation coefficients is the evaluation of the response of the molecular orbitals χ to the atomic displacements $\partial\chi/\partial\mathbf{R}_I$. These responses can be obtained by performing a separate calculation for an isolated CO molecule using the same linear-response approach as that employed in the phonon

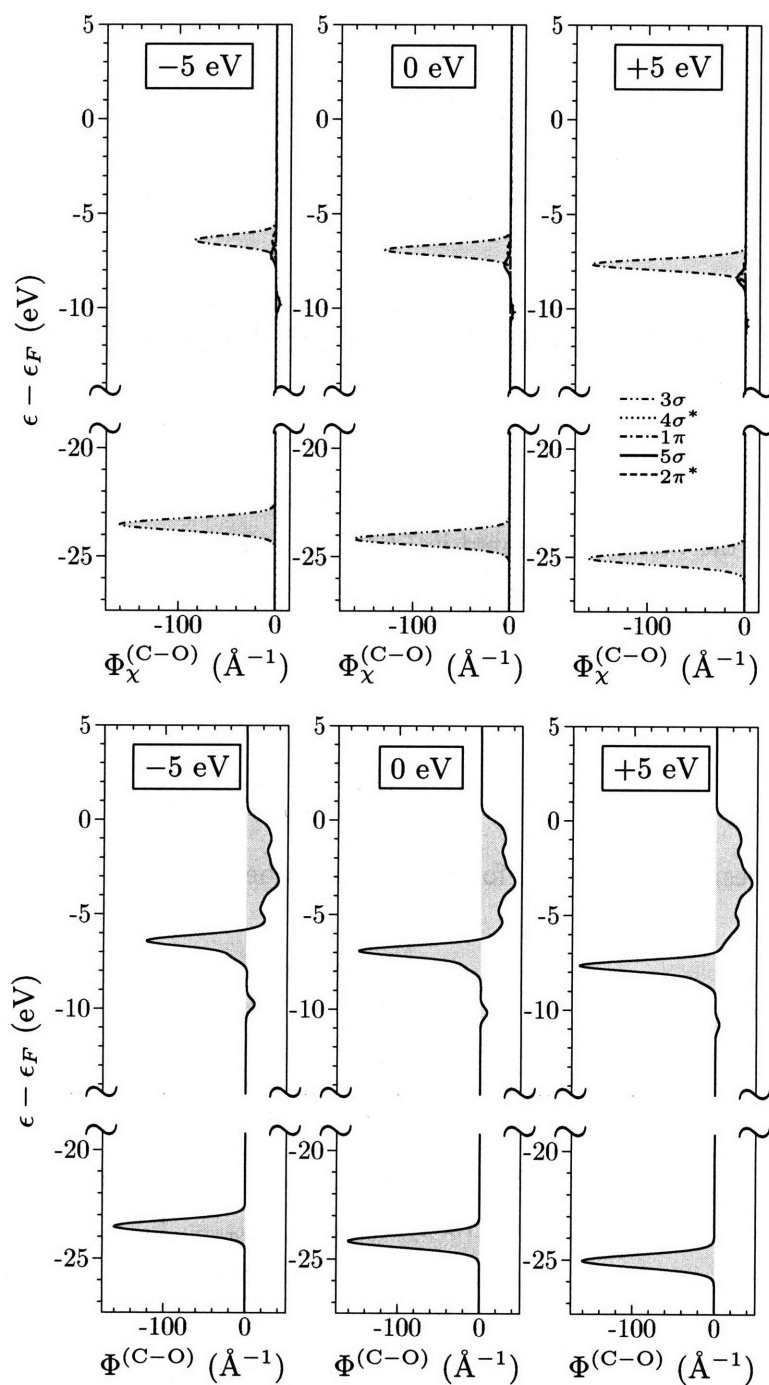Atop FDOS vs. $U_{2\pi*}$

Figure F-1: Force density of states projected on the CO molecular orbitals, and total force density of states as functions of $U_{2\pi*}$ controlling the hybridization of the LUMO orbitals for atop adsorption of CO on Pt(111).
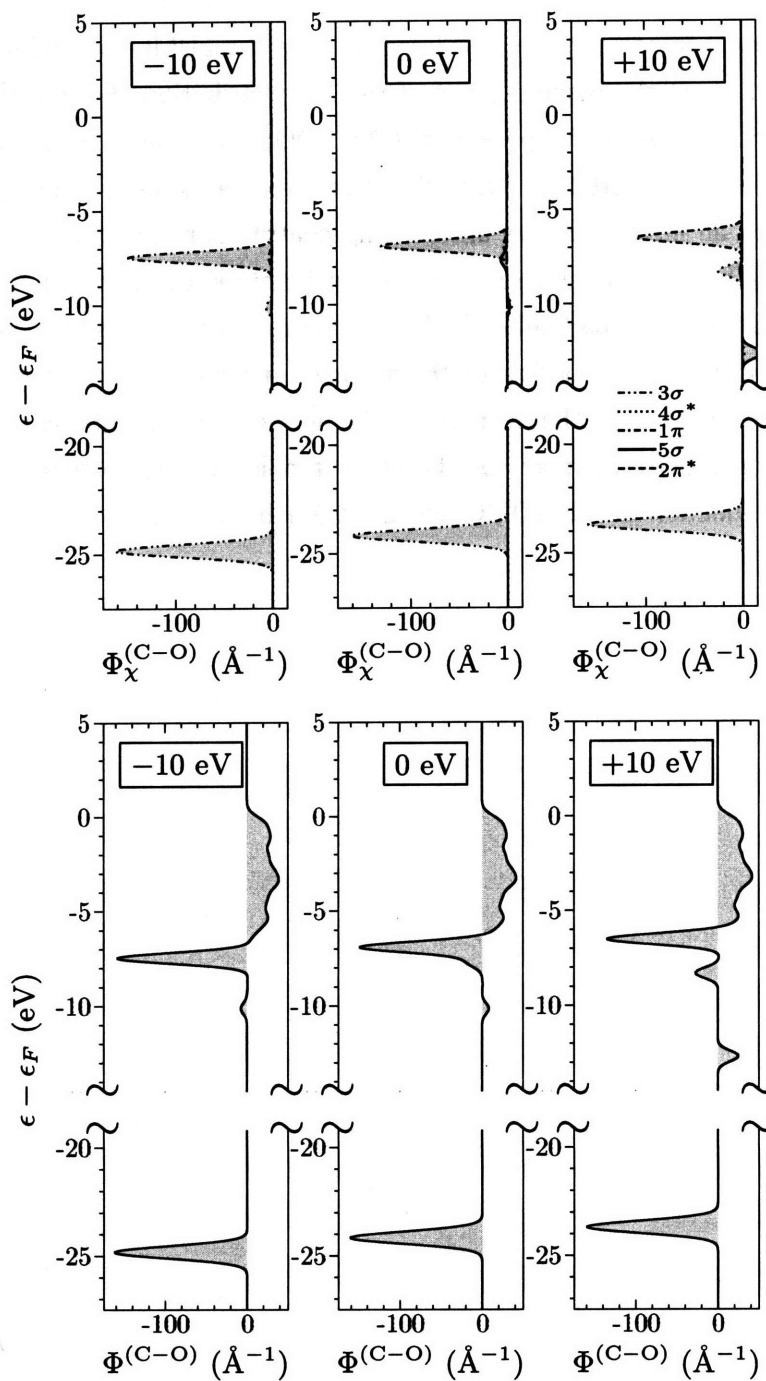
Atop FDOS vs. $U_{5\sigma}$

Figure F-2: Force density of states projected on the CO molecular orbitals, and total force density of states as functions of $U_{5\sigma}$ controlling the hybridization of the LUMO orbitals for atop adsorption of CO on Pt(111).

calculation [19]. The projected and total FDOS spectra as a function of the hybridization parameters for CO adsorbed at the atop site on Pt(111) are reported in Figures F-1 and F-2. The observed trends confirm that large shifts in the LUMO and HOMO single-electron energies do not affect the predominance of the 1π contribution. For positive values of $U_{2\pi^*}$ and $U_{5\sigma}$, the magnitude of the peak in the 1π FDOS increases due to the stronger molecular character of the 1π orbitals. Note that this increase in the 1π bonding contribution is accompanied by an increase in the antibonding contribution from the metal bands. Similar compensation effects in the electronic forces can be observed for negative values of the hybridization parameters. In particular, for $U_{2\pi^*}$ equal to -5 eV corresponding to an unphysical overestimation of the $2\pi^*$ hybridizationthe decrease in the bonding contribution from the 1π orbitals is partially offset by the decrease in the antibonding contribution from the d bands. This observation provides a more specific understanding of the invariance of the stretching frequency as a function of the HOMO and LUMO hybridizations.

Bibliography

[1] L. Galvani. *De Viribus Electritatis in Motu Musculari Commentarius.* Instituti Scientarum, Bologna, 1791.

[2] S. Arrhenius. *Recherches sur la Conductibilité Galvanique des Électrolytes.* PhD thesis, Uppsala University, 1884.

[3] J. O'M. Bockris and S. U. M. Khan. *Surface Electrochemistry.* Plenum Press, 1993.

[4] G. Q. Lu, J. O. White, and A. Wieckowski. *Surf. Sci.*, 564, 131–140, 2004.

[5] B. C. Wood. *Exploring kinetics and thermodynamics in fast-ion conductors and hydrogen-storage materials using ab-initio molecular dynamics.* PhD thesis, Massachusetts Institute of Technology, 2007.

[6] J. E. Tester, E. M. Drake, M. J. Driscoll, M. W. Golay, and W. A. Peters. *Sustainable Energy.* MIT Press, 2005.

[7] J. C. Amphlett, R. M. Baumert, R. F. Mann, B. A. Peppley, P. R. Roberge, and T. J. Harris. *J. Electrochem. Soc.*, 142, 9–15, 1995.

[8] P. Hohenberg and W. Kohn. *Phys. Rev.*, 136, B864, 1964.

[9] N. D. Mermin. *Phys. Rev.*, 137, A1441, 1965.

[10] W. Kohn and L. J. Sham. *Phys. Rev.*, 140, A1133, 1965.

[11] M. Weinert and J. W. Davenport. *Phys. Rev. B*, 45, 13709, 1992.

[12] N. Marzari. *Ab-initio Molecular Dynamics for Metallic Systems*. PhD thesis, University Of Cambridge, 1996.

[13] R. G. Parr and W. Yang. *Density-Functional Theory of Atoms and Molecules*. Oxford Science Publications, 1989.

[14] D. M. Ceperley and B. J. Alder. *Phys. Rev. Lett.*, 45, 566–569, 1980.

[15] J. P. Perdew. *Perdew Electronic Structure of solids '91*. Akademie Verlag, Berlin, 1991.

[16] J. P. Perdew, K. Burke, and M. Ernzerhof. *Phys. Rev. Lett.*, 77, 3865–3868, 1996.

[17] C. Lee, W. Yang, and R. G. Parr. *Phys. Rev. B*, 37, 785, 1988.

[18] A. D. Becke. *J. Chem. Phys.*, 98, 5648–5652, 1993.

[19] S. Baroni, S. de Gironcoli, A. Dal Corso, and P. Giannozzi. *Rev. Mod. Phys.*, 73, 515–562, 2001.

[20] S. de Gironcoli. *Phys. Rev. B*, 51, 6773, 1994.

[21] D. Vanderbilt. *Phys. Rev. B*, 41, 7892–7895, 1990.

[22] A. Dal Corso. *Phys. Rev. B*, 64, 235118–235134, 2001.

[23] N. Marzari, D. Vanderbilt, and M. C. Payne. *Phys. Rev. Lett.*, 79, 1337, 1997.

[24] J. P. Perdew and M. Levy. *Phys. Rev. Lett.*, 51, 1884–1887, 1983.

[25] V. I. Anisimov, J. Zaanen, and O. K. Andersen. *Phys. Rev. B*, 44, 943–954, 1991.

[26] V. I. Anisimov, I. V. Solovyev, M. A. Korotin, M. T. Czyżyk, and G. A. Sawatzky. *Phys. Rev. B*, 48, 16929–16934, 1993.

[27] A. I. Lichtenstein, J. Zaanen, and V. I. Anisimov. *Phys. Rev. B*, 52, R5467–R5470, 1995.

[28] V. I. Anisimov, F. Aryasetiawan, and A. I. Lichtenstein. *J. Phys. Condens. Matter*, 9, 767–808, 1997.

[29] M. Cococcioni and S. de Gironcoli. *Phys. Rev. B*, 71, 35105–35120, 2005.

[30] A. Dal Corso and S. de Gironcoli. *Phys. Rev. B*, 62, 273–277, 2000.

[31] G. Makov and M. C. Payne. *Phys. Rev. B*, 51, 4014–4022, 1994.

[32] J. P. Perdew and A. Zunger. *Phys. Rev. B*, 23, 5048–5079, 1981.

[33] V. A. Johnson. *Phys. Rev*, 60, 373–377, 1941.

[34] C. A. Coulson and I. Fischer. *Phil. Mag.*, 40, 386, 1949.

[35] M. Frigo and S. G. Johnson. *Proc. IEEE*, 93, 216231, 2005.

[36] J. W. Cooley and J. W. Tukey. *Math. Comput.*, 19, 297–301, 1965.

[37] M. T. Heideman, D. H. Johnson, and C. S. Burrus. *Arch. Hist. Exact Sci.*, 34, 265–277, 1985.

[38] M. Leslie and M. J. Gillian. *J. Phys. C: Solid State Phys.*, 18, 973–982, 1985.

[39] R. N. Barnett and U. Landman. *Phys. Rev. B*, 48, 2081–2097, 1993.

[40] D. Marx, J. Hutter, and M. Parrinello. *Chem Phys. Lett.*, 241, 457–462, 1995.

[41] D. Marx and J. Hutter. *Ab Initio Molecular Dynamics: Theory and Implementation*, pages 329–477. Forschungszentrum Jülich, 2nd edition, 2000.

[42] G. J. Martyna and M. E. Tuckerman. *J. Chem. Phys.*, 110, 2810–2821, 1999.

[43] M. R. Jarvis, I. D. White, R. W. Godby, and M. C. Payne. *Phys. Rev. B*, 56, 14972–14978, 1997.

[44] P. E. Blöchl. *J. Chem. Phys.*, 103, 7422, 1995.

[45] P. A. Schultz. *Phys. Rev. Lett.*, 84, 1942–1945, 1999.

[46] J. Neugebauer and M. Scheffler. *Phys. Rev. B*, 46, 16067–16080, 1992.

[47] A. Baldereschi, S. Baroni, and R. Resta. *Phys. Rev. Lett.*, 61, 734–737, 1988.

[48] L. Bengtsson. *Phys. Rev. B*, 59, 12301–12304, 1999.

[49] A. Natan, L. Kronik, and Y. Shapira. *Appl. Surf. Sci.*, 252, 7608–7613, 2000.

[50] B. Meyer and D. Vanderbilt. *Phys. Rev. B*, 63, 205426, 2001.

[51] A. Y. Lozovoi and A. Alavi. *Phys. Rev. B*, 68, 245416, 2003.

[52] P. R. Garabedian. *Partial Differential Equations.* Wiley, 1964.

[53] W. F. Ames. *Numerical Methods for Partial Differential Equations.* Computer Science and Scientific Computing. Academic Press, 3rd edition, 1992.

[54] J. M. Ziman. *Principles of the Theory of Solids.* Cambridge University Press, 2nd edition, 1972.

[55] B. Chicocki and B. U. Felderhof. *Physica A*, 158, 706–722, 1989.

[56] M. Holst and F. Saied. *J. Comput. Chem.*, 14, 105–113, 1993.

[57] M. Holst and F. Saied. *J. Comput. Chem.*, 16, 337–364, 1995.

[58] J.-L. Fattebert and F. Gygi. *Int. J. Quantum Chem.*, 93, 139, 2003.

[59] D. A. Scherlis, J.-L. Fattebert, F. Gygi, M. Cococcioni, and N. Marzari. *J. Chem. Phys.*, 124, 74103, 2006.

[60] W. L. Briggs, V. E. Henson, and S. F. McCormick. *A Multigrid Tutorial.* SIAM, 2nd edition, 2000.

[61] U. Trottenberg, C. W. Oosterlee, and A. Schüller. *Multigrid.* Academic Press, London, 2001.

[62] M. C. Payne, M. P. Teter, D. C. Allan, T. A. Arias, and J. D. Joannopoulos. *Rev. Mod. Phys.*, 64, 1045, 1992.

[63] Numerical recipes. http://www.nrbook.com/

[64] I. F. Greengard. *The Rapid Evaluation of Potential Fields in Particle Systems.* MIT Press, 1988.

[65] N. E. Singh-Miller and N. Marzari. to be submitted.

[66] C. A. Rozzi, D. Varsano, A. Marini, E. K. U. Gross, and A. Rubio. *Phys. Rev. B*, 73, 205119, 2006.

[67] S. Ismail-Beigi. *Phys. Rev. B*, 73, 233103, 2006.

[68] B. Kozinsky and N. Marzari. *Phys. Rev. Lett.*, 95, 166801, 2006.

[69] M. Peressi, S. Baroni, A. Baldereschi, and R. Resta. *Phys. Rev. B*, 41, 12106–12110, 1990.

[70] J. E. Jaffe and A. C. Hess. *J. Chem. Phys.*, 105, 10983, 1996.

[71] K. N. Kudin and G. E. Scuseria. *Phys. Rev. B*, 61, 16440–16453, 1999.

[72] K. N. Kudin and G. E. Scuseria. *J. Chem. Phys.*, 121, 2886–2890, 2004.

[73] N. D. Lang and W. Kohn. *Phys. Rev. B*, 7, 3541–3550, 1973.

[74] M. Otani and O. Sugino. *Phys. Rev. B*, 73, 115407, 2006.

[75] J. O'M. Bockris, A. K. N. Reddy, and M. Gamboa-Adelco. *Modern Electrochemistry*, volume Electrodics 2A. Kluwer Academic/Plenum Publishers, 2nd edition, 1998.

[76] W. Schmickler. *Chem. Rev.*, 96, 3177–3200, 1996.

[77] J. K. Nørskov, J. Rossmeisl, A. Logadottir, L. Lindqvist, J. R. Kitchin, and H. Jónsson T. Bligaard. *J. Phys. Chem. B*, 108, 17886, 2004.

[78] C. D. Taylor, S. A. Wasileski, J.-S. Filhol, and M. Neurock. *Phys. Rev. B*, 73, 165402, 2006.

[79] N. Sato. *Electrochemistry at Metal and Semiconductor Electrodes*. Elsevier, 1998.

[80] S. A. Wasileski, M. T. M. Koper, and M. J. Weaver. *J. Am. Chem. Soc.*, 124, 2797–2805, 2002.

[81] A. Y. Lozovoi and A. Alavi. *J. Electroanal. Chem.*, 607, 140–146, 2007.

[82] J. O'M. Bockris and A. K. N. Reddy. *Modern Electrochemistry*, volume Ionics 1. Plenum Publishers, 2nd edition, 1998.

[83] J. Larminie and A. Dicks. *Fuel Cell Systems Explained*. Wiley-VCH, 2nd edition, 2003.

[84] W. Vielstich, A. Lamm, and H. Gasteiger. *Handbook of Fuel Cells: Fundamentals, Technology, Applications*. Wiley-VCH, 2003.

[85] N. P. Brandon and D. Thompsett. *Fuel Cells Compendium*. Elsevier, 2005.

[86] G. Hoogers. *Fuel Cell Technology Handbook*. CRC Press, 2003.

[87] S. Cramm, K. A. Friedrich, K. P. Geyzers, U. Stimming, and R. Vogel. *Fresenius Journal Of Analytical Chemistry*, 358, 189–192, 1997.

[88] E. Herrero, J. M. Feliu, and A. Wieckowski. *Langmuir*, 15, 4944–4948, 1999.

[89] A. Crown, C. Johnston, and A. Wieckowski. *Surf. Sci.*, 506, L268–L274, 2002.

[90] Y. Y. Tong, H. S. Kim, P. K. Babu, P. Waszczuk, A. Wieckowski, and E. Oldfield. *J. Am. Chem. Soc.*, 124, 468–473, 2002.

[91] F. Maillard, G. Q. Lu, A. Wieckowski, and U. Stimming. *J. Phys. Chem. B*, 109, 16230–16243, 2005.

[92] P. Liu, A. Logadottir, and J. K. Nørskov. *Electrochim. Acta*, 48, 3731–3742, 2003.

[93] B. Hammer, Y. Morikawa, and J. K. Nørskov. *Phys. Rev. Lett.*, 76, 2141–2144, 1996.

[94] B. Hammer and J. K. Nørskov. *Nature*, 376, 238–240, 1995.

[95] J. K. Nørskov, T. Bligaard, A. Logadottir, S. Bahn, L. B. Hansen, M. Bollinger, H. Bengaard, B. Hammer, Z. Sljivancanin, M. Mavrikakis, Y. Xu, S. Dahl, and C. J. H. Jacobsen. *J. Catal.*, 209, 275–278, 2002.

[96] J. Greeley and M. Mavrikakis. *Nat. Mater.*, 3, 810–815, 2004.

[97] K. Reuter, D. Frenkel, and M. Scheffler. *Phys. Rev. Lett.*, 93, 116105–116108, 2004.

[98] B. Hammer, L. B. Hansen, and J. K. Nørskov. *Phys. Rev. B*, 59, 7413–7421, 1999.

[99] P. J. Feibelman, B. Hammer, J. K. Nørskov, F. Wagner, M. Scheffler, R. Stumpf, R. Watwe, and J. Dumesic. *J. Phys. Chem. B*, 105, 4018–4025, 2001.

[100] M. Gajdoš and J. Hafner. *Surf. Sci.*, 590, 117–126, 2005.

[101] L. Köhler and G. Kresse. *Phys. Rev. B*, 70, 165405–165013, 2004.

[102] G. Kresse, A. Gil, and P. Sautet. *Phys. Rev. B*, 68, 73401–73404, 2003.

[103] I. Grinberg, Y. Yourdshahyan, and A. M. Rappe. *J. Chem. Phys.*, 117, 2264–2270, 2002.

[104] S. E. Mason, I. Grinberg, and A. M. Rappe. *Phys. Rev. B*, 69, 161401–161404, 2004.

[105] H. Grönbeck. *Surf. Sci.*, 559, 214–222, 2004.

[106] K. Doll. *Surf. Sci.*, 573, 464–473, 2004.

[107] M. Neef and K. Doll. *Surf. Sci.*, 600, 1085–1092, 2006.

[108] X. Wu, M. C. Vargas, S. Nayak, V. Lotrich, and G. Scoles. *J. Chem. Phys.*, 115, 8748–8757, 2001.

[109] H. Orita, N. Itoh, and Y. Inada. *Chem. Phys. Lett.*, 384, 271–276, 2004.

[110] R. A. Olsen, P. H. T. Philipsen, and E. J. Baerends. *J. Chem. Phys.*, 119, 4522–4528, 2003.

[111] M. Birgersson, C.-O. Almbladh, M. Borg, and J. N. Andersen. *Phys. Rev. B*, 67, 454020–45413, 2003.

[112] J. Greeley, A. A. Gokhale, J. Kreuser, J. A. Dumesic, H. Topsøe, N. Y. Topsøe, and M. Mavrikakis. *J. Catal.*, 213, 63–72, 2003.

[113] M. Mavrikakis, J. Rempel, J. Greeley, L. B. Hansen, and J. K. Nørskov. *J. Chem. Phys.*, 117, 6737–6744, 2002.

[114] D. R. Lide, editor. *CRC Handbook of Chemistry and Physics*. Taylor and Francis, 88th edition, 2007.

[115] C. Lu, I. C. Lee, R. I. Masel, A. Wieckowski, and C. Rice. *Journal Of Physical Chemistry A*, 106, 3084–3091, 2002.

[116] D. F. Ogletree, M. A. Vanhove, and G. A. Somorjai. *Surf. Sci.*, 173, 351–365, 1986.

[117] H. Steininger, S. Lehwald, and H. Ibach. *Surf. Sci.*, 123, 264–282, 1982.

[118] J. A. Steckel, A. Eichler, and J. Hafner. *Phys. Rev. B*, 68, 85416–85424, 2003.

[119] G. Blyholder. *Journal Of Physical Chemistry*, 68, 2772–2777, 1964.

[120] A. Föhlisch, M. Nyberg, J. Hasselstrom, O. Karis, L. G. M. Pettersson, and A. Nilsson. *Phys. Rev. Lett.*, 85, 3309–3312, 2000.

[121] A. Zupan, K. Burke, M. Ernzerhof, and J. P. Perdew. *Journal OF Chemical Physics*, 106, 10184–10193, 1997.

[122] M. Gajdoš, A. Eichler, and J. Hafner. *J. Phys. Condens. Matter*, 16, 1141–1164, 2004.

[123] T. E. Shubina and M. T. M. Koper. *Electrochimica Acta*, 47, 3621–3628, 2002.

[124] B. C. Han and G. Ceder. *Phys. Rev. B*, 74, 205418, 2006.

[125] A. Gil, A. Clotet, J. M. Ricart, G. Kresse, M. García-Hernaández, N. Rosch, and P. Sautet. *Surf. Sci.*, 530, 71–86, 2003.

[126] A. B. Anderson and M. K. Awad. *J. Am. Chem. Soc.*, 107, 7854–7857, 1985.

[127] M. García-Hernaández, D. Curulla, A. Clotet, and F. Illas. *J. Chem. Phys.*, 113, 364–368, 2000.

[128] M. T. M. Koper, R. A. van Santen, S. A. Wasileski, and M. J. Weaver. *J. Chem. Phys.*, 113, 4392–4407, 2000.

[129] S. A. Wasileski, M. T. M. Koper, and M. J. Weaver. *J. Phys. Chem. B*, 105, 3518–3530, 2001.

[130] N. K. Ray and A. B. Anderson. *J. Phys. Chem.*, 86, 4851–4852, 1982.

[131] S. Holloway and J. K. Nørskov. *J. Electroanal. Chem.*, 161, 193–198, 1983.

[132] C. Korzeniewski, P. P. Schmidt S. Pons, and M. W. Severson. *J. Chem. Phys.*, 85, 4153–4160, 1986.

[133] P. S. Bagus, C. J. Nelin, W. Müller, M. R. Philpott, and H. Seki. *Phys. Rev. Lett.*, 58, 559–562, 1986.

[134] P. S. Bagus and G. Pacchioni. *Surf. Sci.*, 236, 233–240, 1990.

[135] M. Head-Gordon and J. C. Tully. *Chem. Phys.*, 175, 37–51, 1993.

[136] F. Illas, F. Mele, D. Curulla, A. Clotet, and J. M. Ricart. *Electrochim. Acta*, 44, 1213–1220, 1998.

[137] M. J. Weaver. *Surf. Sci.*, 437, 215–230, 1999.

[138] J. S. Luo, R. G. Tobin, and D. K. Lambert. *Chem. Phys. Lett.*, 204, 445–450, 1993.

[139] S. A. Wasileski, M. T. M. Koper, and M. J. Weaver. *J. Am. Chem. Soc.*, 124, 2796–2805, 2001.

[140] A. Rappe, K. M. Rabe, E. Kaxiras, and J. D. Joannopoulos. *Phys. Rev. B*, 41, 1227–1230, 1989.

[141] K. Laasonen, A. Pasquarello, R. Car, C. Lee, and D. Vanderbilt. *Phys. Rev. B*, 47, 10142–10153, 1993.